UNIVERSIDADE FEDERAL DE SÃO CARLOS
CENTRO DE CIÊNCIAS EXATAS E DE TECNOLOGIA
PROGRAMA DE PÓS-GRADUAÇÃO EM CIÊNCIA E ENGENHARIA DE MATERIAIS

COMPUTATIONAL MODELING OF RUBBER MULTIAXIAL PRESSING APPLIED TO CERAMIC MATERIALS

Caiuã Caldeira de Melo

São Carlos
April 2021

UNIVERSIDADE FEDERAL DE SÃO CARLOS
CENTRO DE CIÊNCIAS EXATAS E DE TECNOLOGIA
PROGRAMA DE PÓS-GRADUAÇÃO EM CIÊNCIA E ENGENHARIA DE MATERIAIS

COMPUTATIONAL MODELING OF RUBBER MULTIAXIAL PRESSING APPLIED TO CERAMIC MATERIALS

Caiuã Caldeira de Melo

A thesis submitted to Graduate Program in Materials Science and Engineering as a requirement for the degree of DOCTOR IN MATERIALS SCIENCE AND ENGINEERING.

Thesis advisor: Dr. Rodrigo Bresciani Canto
Funding agencies: CNPq - grant 140050/2017-5
CAPES - grant 88881.188615/2018-01

São Carlos
April 2021

Candidate's vitae

Master's degree in Material Science and Engineering by Graduate Program in Materials Science and Engineering – PPGCEM - UFSCar – (2016)

Bachelor's degree in Engineering Physics by Federal University of São Carlos – UFSCar – (2014)

UNIVERSIDADE FEDERAL DE SÃO CARLOS

Centro de Ciências Exatas e de Tecnologia
Programa de Pós-Graduação em Ciência e Engenharia de Materiais

Folha de Aprovação

Defesa de Tese de Doutorado do candidato Caiuã Caldeira de Melo, realizada em 07/04/2021.

Comissão Julgadora:

Prof. Dr. Rodrigo Bresciani Canto (UFSCar)

Prof. Dr. Marcello Rubens Barsi Andreeta (UFSCar)

Prof. Dr. Carlos Alberto Fortulan (USP)

Prof. Dr. François Hild (CNRS)

Prof. Dr. Nicolas Pierre Schmitt (UPEC)

O presente trabalho foi realizado com apoio da Coordenação de Aperfeiçoamento de Pessoal de Nível Superior - Brasil (CAPES) - Código de Financiamento 001.
O Relatório de Defesa assinado pelos membros da Comissão Julgadora encontra-se arquivado junto ao Programa de Pós-Graduação em Ciência e Engenharia de Materiais.

ACKNOWLEDGMENT

“... standing on the shoulders of Giants."

— Isaac Newton

I am grateful to my advisor Rodrigo Bresciani Canto for the precise instructions, the support and for indicating the path to follow during the entire elaboration of this work. I would like to thank the laboratory colleagues Araldo, Antonio, Bruno, Elisa, Fernanda, Filipe, Igor, Katylin, Lucas, Matheus Furlan, Matheus Garcia, Otávio, Rafael Vargas, Ricardo, Salvino and Vinicius for their assistance in conducting the work, which are fundamentals for the realization of this thesis. I thank the technicians of DEMa/UFSCar: Rafael Minhoto, Jhosefer, José Luis and Leomar for facilitating the execution of several tasks of this work.

I am grateful to Nicolas Schmitt, who made possible my internship in the Laboratoire de Mécanique et Technologie (LMT) at ENS Paris-Saclay. Thanks for the fruitful discussions about constitutive modeling and experimental mechanics, which have improved the outcomes of this work. I am also grateful to François Hild for all the knowledge passed during my stay in France. I should say also thanks to all my colleagues at LMT for the discussions and coffees at the famous LMT bar.

Finally, I would like to thank Roberta for being a loving, supportive and understanding partner in my most difficult moments and thank my family for having taught me that education is transformative, that not only makes us better, but may also improve the lives of people around us. This teaching is the driving force for me to continue studying and passing the knowledge I acquire.

I would like to thank to CNPq - Conselho Nacional de Desenvolvimento Científico e Tecnológico for the financial support to carry out this work with a scholarship, process 140050/2017-5.

To CAPES - Coordenação de Aperfeiçoamento de Pessoal de Nível Superior for the financial support by the PDSE grant 8881.188615/2018-01 used during my period at LMT, CAPES (Brazil).

This study was financed in part by the Coordenação de Aperfeiçoamento de Pessoal de Nível Superior - Brasil (CAPES) - Finance Code 001.

Nullius in verba.

— The Royal Society's motto

ABSTRACT

Uniaxial and isostatic powder pressing are well known processes. However, disadvantages such as the production of heterogeneous parts or low productivity, respectively, are intrinsic drawbacks. Rubber Multiaxial Pressing (RMP) is an alternative process to overcome these disadvantages. In RMP, the pressing tool consists of a flexible rubber mold, confined in a rigid die, where pressing takes place by the action of a piston. This loading is transferred to the powder in the inner cavity of the rubber mold, whose distribution depends on the geometry of the tool parts and the tribological conditions between them. One drawback of RMP lies in the tool design stage due to the challenge of accurately predicting the shape of the flexible mold in its deformed configuration. The complexity of the deformed geometry is due to inhomogeneous strains induced by the nonlinear mechanical behavior of rubber and powder, as well as by the tribological conditions. In this context, this study aims to investigate the process characteristics and use the finite element (FE) simulation to assist in tool design for RMP, thus enabling the manufacture of compacted parts with a geometry that meets the dimensional requirements and a mechanical strength that allows the part to retain its integrity during the next stages of processing. To perform reliable numerical analysis, a characterization of the mechanical behavior of the involved materials is required. Mechanical tests were performed to characterize the rubber used in the mold and the alumina powder. Once the constitutive models were identified, FE analyses of the RMP were performed. The case study explored by this research project was the pressing of an alumina ceramic femoral head for hip implant. Finally, experimental and computational results were compared in order to highlight the accuracy of the numerical analyses implemented.

Keywords: Rubber Multiaxial Pressing; Finite Element Analysis; Digital Image Correlation.

RESUMO

Modelagem computacional da prensagem multiaxial com elastômero aplicada a materiais cerâmicos

As prensagens uniaxial e isostática são processos bem conhecidos. No entanto, apresentam desvantagens como a produção de peças heterogêneas ou baixa produtividade, respectivamente. A Prensagem Multiaxial com Elastômero (RMP, na sigla em inglês) é uma alternativa para reduzir estas desvantagens. Na RMP o ferramental de prensagem é composto por um molde flexível, confinado em uma forma rígida, onde é submetido à ação de um pistão. Este carregamento é transferido ao pó presente na cavidade interna do molde elastomérico de forma multiaxial. Uma desvantagem da RMP está na etapa de projeto do ferramental, pois é difícil prever a forma do molde flexível em seu estado deformado. A geometria deformada é complexa devido às deformações não-homogêneas induzidas principalmente pelos comportamentos mecânicos não-lineares do elastômero e do pó, assim como pelas condições tribológicas. Neste contexto, este projeto estudou as características do processo e usou a simulação computacional para auxiliar no projeto do ferramental para a RMP, mostrando a viabilidade da fabricação de peças que atendem aos requisitos dimensionais e com resistência mecânica que as permitam permanecerem integras durante as fases seguintes do processamento. Para realizar uma análise numérica confiável, foi necessária uma extensa caracterização do comportamento mecânico dos materiais envolvidos. Foram realizados ensaios mecânicos para a caracterização do elastômero utilizado no molde flexível e do pó de alumina. Uma vez determinados os modelos constitutivos, foi realizada uma análise em elementos finitos da RMP. O estudo de caso utilizado por este projeto de pesquisa foi o processo de prensagem de uma esfera cerâmica de alumina para implante de quadril. Por fim, os resultados experimentais e computacionais foram comparados para destacar a precisão das análises numéricas implementadas.

Palavras-chaves: Prensagem Multiaxial com Elastômero; Análise em elementos finitos; Correlação de Imagens Digitais.

x

SUMMARY

FOLHA DE APROVAÇÃO i

ACKNOWLEDGMENT iii

ABSTRACT vii

RESUMO ix

SUMMARY xi

TABLE INDEX xiii

FIGURE INDEX xv

LIST OF ACRONYMS AND ABBREVIATIONS xxi

LIST OF SYMBOLS xxiii

1 INTRODUCTION 1

2 LITERATURE REVIEW 5
- 2.1 Powder pressing 5
- 2.2 Mechanical behavior of rubbers 8
- 2.3 Finite Element Modeling 11
- 2.4 Constitutive models for powder pressing 12
- 2.5 Hyperelastic models for rubbers 18
- 2.6 Rubber Multiaxial Pressing (RMP) 19
- 2.7 Pressing of a ceramic femoral head for hip replacement 24

3 MATERIALS AND METHODS 29
- 3.1 Ceramic powder 29
- 3.2 Rubber 30
- 3.3 Identification of constitutive model for powder compaction 31

3.3.1 Preliminary identification/validation procedure for powder compaction model . . . 31
3.3.2 Uniaxial compression test with bending consideration using digital image correlation . . . 37
3.3.3 Multi-test approach to identify a density-dependent constitutive model . . . 49
3.3.4 Diametral compression tests and evaluation of angle of friction for Drucker-Prager surface using dilatancy phenomenon 51
3.4 Identification of constitutive model for rubber . . . 54
3.5 Design, numerical and experimental simulation of RMP . . . 55

4 RESULTS . . . 59
4.1 Preliminary identification/validation procedure results for powder compaction model . . . 59
4.1.1 Experimental procedure . . . 60
4.1.2 Parameter calibration with pressure sensor data . . . 62
4.1.3 Calibration of the cap hardening law . . . 63
4.1.4 Comparison between experimental and numerical results . 63
4.2 Uniaxial compression test with bending consideration . . . 66
4.2.1 Digital image correlation and multi-point constraint . . . 66
4.2.2 Classical FEMU-F analysis . . . 68
4.2.3 Plane stress FEMU-F analysis . . . 72
4.2.4 3D Coupled FEMU-F analysis . . . 75
4.3 Multi-test approach for identification of density-dependent parameters . . . 77
4.4 Angle of friction . . . 81
4.5 Density-dependent elastic modulus and material cohesion . . . 82
4.6 Constitutive model for RenCast 4644-1 rubber . . . 83
4.7 Design, numerical and experimental simulation of RMP . . . 85

5 CONCLUSIONS . . . 91

6 REFERENCES . . . 95

TABLE INDEX

2.1 Elastic parameters and compressibility [27]. 9
2.2 Main parameters of DPC constitutive model and friction coefficient between alumina powder and die walls obtained from the literature 17
2.3 Poisson's ratio for rubbers used in the study of Shima et al. [16]. . . 21

3.1 Physical properties of RenCast® 4464-1 rubber [54] 31
3.2 Range of values used for the calibration of the model parameters . 36
3.3 DIC hardware parameters [63] 39
3.4 Summary of calibration analyses [63] 48
3.5 Information about specimens and uniaxial compression tests [63] 50
3.6 DIC hardware parameters [63] 51
3.7 Information about specimens and diametral compression tests . . . 51

4.1 Calibrated parameters 62
4.2 Calibrated parameters for classical FEMU-F analysis 73
4.3 Calibrated parameters for plane stress FEMU-F analyses 75
4.4 Calibrated parameters for 3D FEMU-F analysis 76
4.5 RMS values of the curve fitting 84
4.6 Calibrated parameters for the Ogden hyperelastic model (order 3) . 84

FIGURE INDEX

2.1 Steps of single-action uniaxial die compaction. 6
2.2 Steps of isostatic pressing (*wet bag*). 6
2.3 Steps of Rubber Multiaxial Pressing (RMP), highlighting a usual geometric defect ("elephant foot"). 7
2.4 Typical stress-strain curve of a rubber, adapted from Treloar [25]. . 9
2.5 Process of FE analysis, adapted from Bathe [36]. 12
2.6 Yield surface of Green-Shima-Oyane model (GSO) 14
2.7 Modified Cam-Clay model implemented in Abaqus® software [27]. 15
2.8 Yield surface of the DPC model implemented in Abaqus® [27]. . . 16
2.9 Deformation modes used in hyperelastic models calibration [27]. . 19
2.10 Rubber Multiaxial Pressing, adapted from Shima et al. [16]. 20
2.11 Green compacts of metallic powder processed through RMP, adapted from Sagawa et al. [3]. 21
2.12 FE Model for RMP by Shima et al. [16]. 22
2.13 Simulation of RMP by Shima et al. [16] (metallic powder 17-4PH PF-20 and rubber KE12): (a) shape of the green compact and its density distribution e (b) vectors of displacement field in the rubber mold at a pressure of 50 MPa. 23
2.14 Rubber mold optimization by Shima et al. [16]: (a) Initial estimate for the rubber mold cavity; (b) result of the simulation with the initial rubber mold and (c) optimized rubber mold. 25
2.15 Hip replacement: (a) components of prosthesis adapted from Capello et al. [53] and (b) X-Ray of the implant extracted from [50]. 26
2.16 Ceramic femoral head for hip replacement: (a) Dimensions after green machining, and (b) after sintering and finishing, units in mm [9]. 27
2.17 (a) Design of adequate rubber mold to the pressing of the ceramic head, and (b) axysimmetric FE model: mesh and boundary conditions [9]. 27

2.18 Numerical modelling of isostatic pressing for initial rubber mold (a) and optimized rubber mold (b) [9]. 28

3.1 Microscopy of the studied ceramic powder acquired in a Zeiss Stemi 2000-C microscope [43] 30

3.2 Steps of the experimental procedure: (a) Uniaxial and (b) isostatic pressing [56] 32

3.3 Cylindrical die (a) with a high height-to-diameter ratio to induce a density gradient along the height of the green compact powder, instrumented with two pressure sensors (b) [56] 33

3.4 Photographies of the (a) metal rigid die and (b,c) details of pistons-die walls assembly [56] 33

3.5 Uniaxial pressing test: Cross-head displacement (left) and force (right) vs. time [56] 34

3.6 FE simulation of experimental procedure steps: (a) Uniaxial pressing (axial loading/unloading, (b) ejection and (c) isostatic pressing [56] 35

3.7 Experimental setup. (a) Specimen between the testing machine platens ($20.3 \times 20.3 \times 50.8$ mm^3), and (b) upper schematic view of the camera disposition to image two adjacent lateral surfaces [63] 39

3.8 Force history showing the image acquisition instants (depicted with solid circles) [63] 40

3.9 One-element model to calibrate material parameters via FEMU-F using uniform stress assumption [63] 47

3.10 Reference images with mesh and boundary conditions applied in the plane stress analysis of faces $y-z$ (a) and $x-y$ (b). The ROI dimensions where the mesh is defined are ≈ 30 mm in height and ≈ 20.3 mm in width [63] 48

3.11 Extrapolated boundary conditions for the first four force peaks of (1 to 4): (a) top and (b) bottom surfaces of the 3D model. The red circles depict measured quantities [63] 49

3.12 (a) Image of the specimen for Test 2 and (b) corresponding loading history. 52
3.13 (a) Description of the tools used in Rubber Multiaxial Pressing and (b) detailed view of rubber mould. 56
3.14 Finite Element model for RMP 57

4.1 Load-displacement curve: raw data and with compliance correction 60
4.2 Normal stress on lower and upper pistons measured by pressure sensors, and normal stress computed from machine force and the cross-section area of the piston. 61
4.3 Profiles of the compacted part after isostatic pressing of 25 and 200 MPa 61
4.4 Comparison of normal stress measured by pressure sensors and predicted by the FE analysis for lower and upper pistons 63
4.5 Experimental and numerical profiles of the compacted part after isostatic pressing 64
4.6 Density field after: (a) closed-die pressing and ejection, (b) isostatic pressing at 25 MPa and (c) 200 MPa 65
4.7 Vertical displacement fields (positive downward, expressed in µm) using independent DIC analyses for faces $y-z$ and $x-y$ 67
4.8 Vertical displacement fields of faces $y-z$ and $x-y$ (positive downward, expressed in µm) when the constraints of equal vertical displacements is prescribed on the common edge 68
4.9 (a) Initial visual positioning of mesh boundaries (yellow) and after optimization (white). (b) Cost function e_s vs. vertical translation of mesh on $x-y$ face 69
4.10 Vertical displacement fields for faces $y-z$ and $x-y$ (positive downward, expressed in µm) when the constraints of equal vertical displacements is prescribed on the common edge and the meshes were repositioned 70
4.11 Computed load sensitivity for $x-y$ face 70

4.12 Hessian matrix in decimal logarithm for $x-y$ face, (b) Decimal logarithm of the eigenvalues of Hessian matrix, and (c) corresponding eigenvectors. 71

4.13 Classical (independent) analyses using DIC as a virtual strain gauge. Experimental and numerical stress-strain curves for (a) $y-z$ face, and (b) $x-y$ face 72

4.14 Load residuals for (a) $x-y$ and (b) $y-z$ faces 73

4.15 Plane stress analyses using measured boundary conditions. Experimental and computed forces for (a) $y-z$ and (b) $x-y$ faces . . 74

4.16 Force residuals for the plane stress analyses 74

4.17 (a) Experimental and computed forces, and (b) corresponding residuals for the 3D Coupled FEMU-F analysis 75

4.18 Eccentricity of the load distribution at loading peaks, expressed as distance from the center of the cross section 77

4.19 Axial strain distribution in the FE model for the last image (88) . . . 77

4.20 Average (square symbols) and standard deviation (solid blue line) of axial strain vs. image number 78

4.21 Curves of experimental and numerical forces from (a, b and c) uniaxial compression tests 1, 2 and 3 with specimens pressed at 50 MPa, (d , e and f) tests 4, 5 and 6 with specimens pressed at 100 MPa and (g , h and i) tests 7, 8 and 9 with specimens pressed at 200 MPa. 79

4.22 Parameters of Drucker-Prager surface evaluated from multi-test approach 80

4.23 (a) Axial, (b) transversal and (c) volumetric strain for the Brazilian test 1. 82

4.24 Linear regression of the pressure and equivalent Mises stress data identified by the dilatancy approach. 82

4.25 Material cohesion as a function of compaction pressure for the studied ceramic powder. 83

4.26 Calibration with the tests on the rubber material: (a) Nominal strain-stress curves for uniaxial compression tests and (b) nominal stress as a function of volumetric ratio for the volumetric compression tests. 84
4.27 Optimized rubber mold geometry for RMP of a ceramic femoral head. 86
4.28 Profile of the undeformed cavity of the rubber mold and profiles of the desired compact (target) and the outcome of the finite elements analysis. 86
4.29 Rubber parts manufactured for RMP: (a) Auxiliary 3D-printed part, (b) bottom view of the rubber mold, and (c) top view of the rubber mold and cap. 87
4.30 Ceramic femoral head produced via RMP. 87
4.31 Measured profiles of the femoral head pressed by RMP: (a) Top view image, (b) Side view 1, (c) Side view 2, (d) Top view profile and (e) Side view profiles. 88
4.32 Comparison between experimental and numerical profiles. 89
4.33 Comparison between the density fields obtained by the FE simulations with the (a) preliminary and (b) density-dependent constitutive models. 90

xx

LIST OF ACRONYMS AND ABBREVIATIONS

DIC -Digital Image Correlation

DPC -Drucker-Prager/Cap model

FE -Finite Element

FEMU -Finite Element Model Updating

GSO -Green-Shima-Oyane model

FEM -Finite Element Method

MCC -Modified Cam-Clay model

RMP -Rubber Multiaxial Pressing

LIST OF SYMBOLS

a - Parameter related to the yield surface size in the MCC model or nodal displacement

b - Parameter of the Voce's law

$\mathbf{B}$ - left Cauchy-Green stretch tensor

C_{ij} - Material parameters in the polynomial form of W proposed by Rivlin

d - Material Cohesion

D_{ij} - Material parameters in the polynomial form of W proposed by Rivlin

D - Material parameter related to compressibility in the Arruda-Boyce model

dV - Permanent volumetric change

$d\varepsilon$ - Strain increment

$d\varepsilon_v^p$ - Volumetric plastic strain increment

$d\bar{\varepsilon^p}$ - Devatoric plastic strain increment desviadora

$d\sigma$ - Stress increment

f - Reference image

F - Yield function

F_c - Cap surface in the Drucker-Prager Cap model or computed forces of FEMU

F_m - Measured forces of FEMU

F_t - Transition surface in the Drucker-Prager Cap model

F_s - Shear failure surface in the Drucker-Prager Cap model

g - Deformed image

H - Hessian matrix

G_0 - Initial shear modulus

I_1 - First invariant of Cauchy-Green stretch tensor

I_2 - Second invariant of Cauchy-Green stretch tensor

I_3 - Third invariant of Cauchy-Green stretch tensor

J - Square root of I_3

K_0 - Initial bulk modulus

M - Constant in the Modified Cam-Clay model

p - Pressure

$\mathbf{p}$ - Set of parameter

p_a - Evolution parameter of the Cap yield surface in the Drucker-Prager Cap model

p_b - Pressure in the Drucker-Prager Cap model

p_0 - Initial pressure

q - Mises stress

q_0 - initial Mises stress

R - Shape parameter in the Drucker-Prager Cap model

V - Volume

$\mathbf{u}$ - Pixel displacement

V_0 - Initial volume

W - Deformation energy potential

α - Constant that ensures a smooth transition between Drucker-Prager Cap surfaces

α_i - Parameter of Ogden model

β - Parameter of the Modified Cam-Clay model or internal friction angle of the Drucker-Prager Cap model

ε_v^p - Volumetric plastic strain

$\bar{\varepsilon^p}$ - Deviatoric plastic strain

$\bar{\eta^p}$ - Cost-function variable

λ - Lagrange multiplier

$\lambda_1, \lambda_2, \lambda_3$ - Principal stretches

λ_L - Material parameter related to shear behavior in the Arruda-Boyce model

ν - Poisson ratio

σ - Stress tensor

σ_∞ - Parameter of the Voce's law

$\sigma_\mathbf{y}$ - Yield stress

μ - Friction between powder and die walls and material parameter related to shear behavior of the Arruda-Boyce model

μ_i - Material parameters of the Ogden model

ϕ_i - Shape function

1 INTRODUCTION

> “It doesn’t matter how beautiful your theory is,
> it doesn’t matter how smart you are. If it
> doesn’t agree with experiment, it’s wrong."
> — Richard P. Feynman

Uniaxial and isostatic pressing are widely used in industry to produce parts from powder materials [1, 2]. In both processes, a green part is produced and then sintered to obtain the final part, whose properties strongly depend on these processes. Uniaxial pressing is the most widely used, mainly due to its high productivity and consists of filling a rigid die with powder and compacting it by the action of a piston, producing green compacts with well defined geometry. However, components with homogeneous distribution of densities and mechanical properties are hard to obtain. Less compacted regions tend to exhibit lower mechanical properties, which cause distortion and defects during firing. Isostatic pressing produces more homogeneous compacts in terms of density (and consequently, mechanical properties) distribution, but its productivity is considerably lower in comparison to uniaxial pressing [3].

Rubber Multiaxial Pressing (RMP), also known as Rubber Isostatic Pressing (RIP) [4], was developed as an alternative to more conventional processes (uniaxial and isostatic pressing). In RMP, the powder material is confined in a flexible rubber mold. This assembly is inserted into the cavity of a rigid die and the powder material is compacted multiaxially by the surfaces of the rubber mold cavity that is loaded and deformed by the axial advance of the piston. RMP brings together the advantages of both aforementioned processes, *i.e.,* leading to a more homogeneous property distribution as in isostatic pressing but with similar productivity of uniaxial pressing. Yet, the prediction of the final compact geometry is a challenge, since it depends on the nonlinear behavior of rubber and the powder, the geometry of the tooling parts and the tribological conditions between the interfaces of the used materials. For instance, in RMP, the “elephant foot” is a

common geometric defect. This flaw is a consequence of friction between rigid and flexible parts, which results in mismatch of deformations. Defect mitigation is sought through lubrication and changes of geometry in costly trial-error steps. Through computer simulations, it is possible to reduce the development time of a product manufactured by this process by predicting some quality control variables such as the dimensions of the compacted part and its mechanical properties.

Finite element (FE) analyses have been used by several authors [5–15] to predict the shape, density distribution and to prevent crack formation in green compacts obtained in classical processes, *i.e.,* uniaxial and isostatic pressing. Although this computational tool is very useful for product development or optimization, it should be emphasized that the accuracy of the results is strongly dependent on the parameters of the models. In the case of pressing simulation, the FE model generally depends on the mechanical behavior of the powder and tooling materials, the part geometries and the tribological conditions between parts. The mathematical expression of the mechanical behavior of materials is called the constitutive model. A constitutive model with plasticity has permanent or plastic strains [1]. These models, usually composed of elastic and plastic parts, use a yield surface to delimit the elastic regime of the material, that is, to define in which mechanical loads the material will not present permanent deformations. The flow rule and the hardening law define how permanent strains will occur in relation to their magnitude and direction.

In this context, computer modeling is a powerful tool for studying and improving RMP process variables, for example, by optimizing the tooling geometry to obtain green compacts with more homogeneous density distributions and dimensions that minimize the need for subsequent machining operations. In this study, an example of RMP application dealt with the pressing of a ceramic sphere for an alumina (Al_2O_3) hip implant. This piece is usually produced by cold isostatic pressing. The pressing of this component was firstly studied by Canto [9] who focused on reducing material excess for green machining.

[1] in the macromechanical approach used in this work, the ceramic powder, composed of grains and voids, constitutes a continuous medium. Permanent strains in the continuous medium are called plastic strains.

Although RMP (or RIP) has been reported for over three decades [3, 4, 16, 17], the process is not widely addressed in the literature. For example, none of the studies found in the Web of Science database in a search for “Rubber Isostatic Pressing” used ceramic materials. Some of these articles cite the possibility of applying the process to ceramic powders, but without studying specifically ceramic materials. The lack of interest in the application of this technique in the industrial and academic environment may be associated with the difficult development of pressing tools (rigid die and rubber mold), non-linearity effects of the materials involved (powder and rubber), large deformations, and the effect of friction, which together result in nontrivial problem. Further, computer modeling is a powerful tool that can be used to enable its application and considerably improve RMP processes. For instance, FE analyses make tool design easier by optimizing tool geometry to achieve green compacts with more homogeneous density distribution and reduced processing times, *e.g.,* reducing green machining time. The purpose of this thesis is to improve and facilitate the application of RMP through the use of FE modeling. Conventional and original methodologies will be applied for the identification of constitutive models and coefficients of friction between the different surfaces (compacted part, flexible mold and rigid die). The validation of the proposed methodology will also be performed by applying it to an industrial case study of a ceramic sphere for hip replacement. The manufacturing of this component is commonly performed by isostatic pressing and it is believed to be a candidate case to have its processing benefited from advantages of RMP.

2 LITERATURE REVIEW

> I could be bounded in a nutshell, and count myself a king of infinite space.
>
> — William Shakespeare, Hamlet

This study is comprised of three main subjects: ceramic powder pressing, elastomeric materials and computational modeling. Understanding the phenomenology of ceramic powder pressing and the mechanical behavior of elastomers, as well as the experimental identification of constitutive model parameters associated with these materials, are essential for the computational modeling of RMP and its application in an industrial case study.

2.1 Powder pressing

Pressing is a process widely used in the ceramics industry to produce parts such as valves, refractory bricks, cutting tools and spark plugs [12, 18–20]. In essence, pressing is the densification of a material, initially a powder with high void fraction, by the action of mechanical loading. There are two conventional processes related to this procedure: uniaxial and isostatic pressing. In uniaxial pressing, the powder is compacted into a rigid die by the action of a piston acting only with movement in the axial direction. Uniaxial pressing may be performed in two different ways: single-action pressing where only one piston is movable and double-action pressing where both top and bottom pistons may be displaced. The compacted part assumes the final geometry of the die cavity. In general, this method produces parts with heterogeneous density distributions due to friction between the contacting surfaces. However, process productivity is high, thereby decreasing process cost. The steps involved in uniaxial pressing are illustrated in Figure 2.1.

Isostatic pressing consists of filling a flexible mold with the powder material

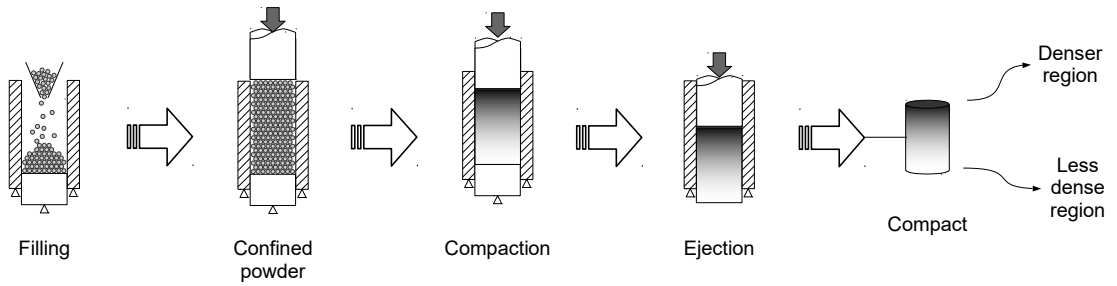

Figure 2.1 Steps of single-action uniaxial die compaction.

and mechanical loading comes from the hydrostatic pressure of a pressurized fluid, which acts evenly distributed on the external surfaces of the flexible mold. The final part has a more homogeneous density distribution compared to uniaxial pressing. However, isostatic pressing is more time consuming and costly. Figure 2.2 shows the steps of isostatic pressing.

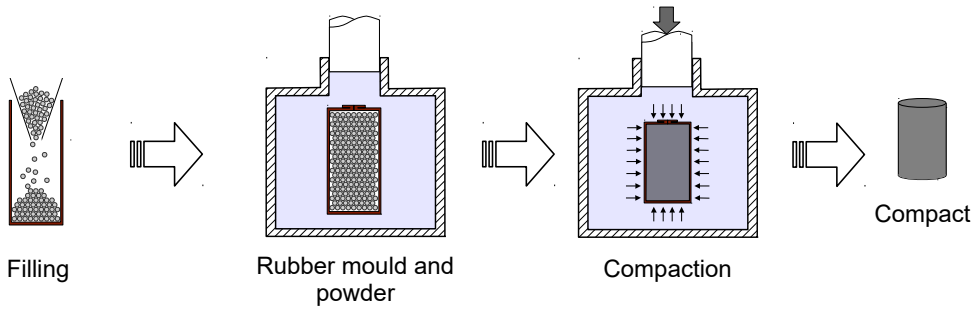

Figure 2.2 Steps of isostatic pressing (*wet bag*).

As a third way of carrying out pressing, the Rubber Multiaxial Pressing (RMP) was developed to bring together the advantages of both uniaxial and isostatic pressings. This process consists of applying a compressive loading, obtained by the action of an axially moving piston, in a flexible rubber mold confined in a rigid die (Figure 2.3). This loading is transferred to the powder present in the inner cavity of the rubber mold in a multiaxial way due to the quasi-incompressibility of the rubber. The loading distribution depends mainly on the geometry of the parts of the entire tooling, the tribological conditions between the contact surfaces and the mechanical behavior of the materials (powder and rubbers). In Figure 2.3, the geometric defect known as “elephant foot” is outlined. This defect is a consequence

of the tribological conditions of the surfaces between the parts, which jeopardizes the prediction of the final compact shape without the aid of computational tools such as FE analysis.

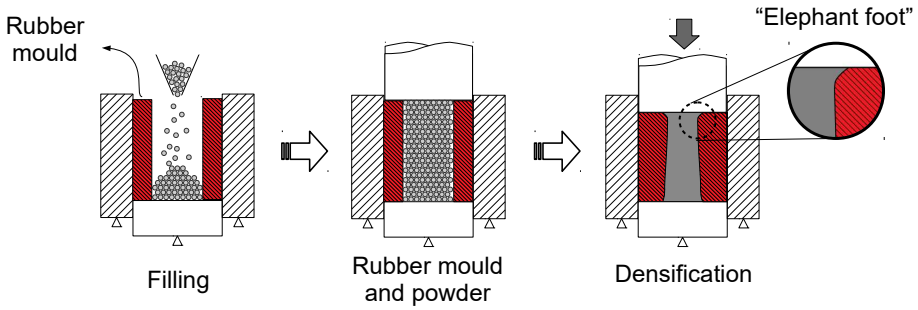

Figure 2.3 Steps of Rubber Multiaxial Pressing (RMP), highlighting a usual geometric defect ("elephant foot").

To better understand and mitigate the flaws of pressing, several numerical approaches were developed to model the densification behavior of the powder in the process. In micromechanical approaches, two distinct procedures may be used: the discrete element method (DEM) [21] and the finite element method (FEM) applied to multiple particles [22]. When DEM is used, the powder is considered as rigid particles and their motion is analyzed using Newton's second law. To model pressing more accurately, FEM has been used to simulate each powder grain and its interactions, the so-called multiple-particles finite element method [23]. In a green compact, the number of grains can be estimated to be in the order of thousands or millions, so the computational cost of these first two (micromechanical) approaches is very high, making them unfeasible in most industrial cases.

More commonly used, the macromechanical approach considers the powder grains and the voids (inside and between them) as a continuous and isotropic medium. This assumption holds true if the dimensions of the compacted part are much larger than the grain dimensions. The continuous medium approach has been satisfactory in solving industrial problems in recent decades [9, 12, 18, 19, 24]. The constitutive models from this approach are called phenomenological. These pressing models are plasticity models characterized by a yield criterion, a hardening law and a flow rule [5]. Plastic strain is associated with material den-

sification. The deformation of each grain (in the case of metallic and polymeric powders) and the packing between them are macroscopically seen as a permanent (or plastic) strain. To further densify the material, *i.e.,* to increase the plastic strain, it is necessary to increase the compressive loading in the compact. The relationship between plastic deformation and compressive loading, usually measured by the mean stress (also called pressure), is expressed by the hardening law. The yield criterion delimits the stress states in which the material will have reversible (or elastic) deformations of the stress states in which the continuous medium has undergone plastic strain. The flow rule allows a relationship to be established between the stress and the amount of plastic strain suffered by the material. Such constitutive laws will be further discussed in Section 2.4 (page 16).

2.2 Mechanical behavior of rubbers

The most notable physical characteristic of rubbers is their great flexibility even under relatively small stresses [25]. A typical stress-strain curve in a simple natural rubber tensile test is presented in Figure 2.4. In this type of mechanical test, the engineering strain of rubber may reach 1000 %, which makes classical treatments of deformations inaccurate.

The stress-strain curve is noticeably nonlinear. Thus, Hooke's law is not directly applicable, it is only possible to assign a modulus of elasticity to the material for conditions of small deformation where there is a linear approximation of the stress-strain curve[1]. In this case, typical values of modulus of elasticity are of the order of 1 MPa [16, 25, 26]. These properties of large stretches and low stiffness contrast with the properties of other materials such as metals and ceramics. For example, steel has its Young's modulus around 2×10^5 MPa and its maximum strain in the elastic regime is between 0.1 and 1 %. Therefore, there is a huge difference between other engineering materials and rubbers, suggesting a different treatment.

[1] Hooke's law is applicable only for small deformations in rubbers, which is not the case in this study.

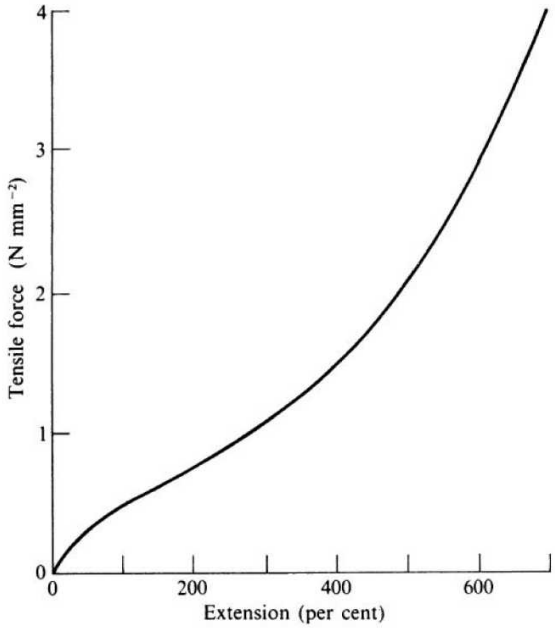

Figure 2.4 Typical stress-strain curve of a rubber, adapted from Treloar [25].

Another well-know property of rubbers is their quasi-incompressibility, in other words, high initial bulk modulus (K_0) relative to initial shear modulus (G_0) [27]. In cases where the material is highly confined (*e.g.,* o-rings used for sealing), rubber deforms very little even at high mechanical loads. In this context, rubbers are often considered incompressible. This consideration is supported by their initial bulk modulus K_0 being about three orders of magnitude higher than the initial shear modulus G_0 (which is equivalent to a Poisson's ratio $\nu \approx 0.5$ - see Table 2.3) [28]. However, some applications such as RMP are strongly influenced by rubber compressibility, and its precise characterization is essential.

Table 2.1 Elastic parameters and compressibility [27].

K_0/G_0	ν
10	0.452
50	0.490
100	0.495
1000	0.4995
10000	0.49995

In addition to the characteristics already mentioned, rubbers may exhibit other

complex aspects such as time-dependent behavior, hysteresis, and Mullins effect [29]. These phenomena will not be dealt herein. A great effort has been expended by several authors to propose realistic constitutive equations for rubbers [30–34]. The constitutive models are based on the general theory of hyperelasticity [25], and aim to establish relationships between stress and strain from a strain energy potential. An efficient hyperelastic model should prioritize four aspects [29]:

1. The typical stress-strain curve must be reproduced by the model;
2. The model must be stable for several strain states;
3. The number of parameters should be as small as possible to reduce the amount of experiments required for model calibration;
4. The mathematical formulation must be simple and suitable for numerical implementation.

The constitutive behavior of hyperelastic materials is derived from the strain energy potential function, W, based on the three Cauchy-Green stretch tensor invariants I_1, I_2 e I_3. W is the energy stored in the material per unit of reference volume (volume of initial configuration) as a function of strain at one point of the material:

$$W = f(I_1, I_2, I_3) \tag{2.1}$$

and

$$\begin{aligned} I_1 &= tr(\mathbf{B}) = {\lambda_1}^2 + {\lambda_2}^2 + {\lambda_3}^2 \\ I_2 &= \tfrac{1}{2}\left[tr(\mathbf{B})^2 - tr(\mathbf{B})^2\right] = {\lambda_1}^2{\lambda_2}^2 + {\lambda_1}^2{\lambda_3}^2 + {\lambda_2}^2{\lambda_3}^2 \\ I_3 &= det(\mathbf{B})) = {\lambda_1}^2{\lambda_2}^2{\lambda_3}^2 \end{aligned} \tag{2.2}$$

where **B** is the left Cauchy-Green stretch tensor, and λ_1, λ_2 and λ_3 the principal stretches. The Cauchy stress tensor $\boldsymbol{\sigma}$ is evaluated by the differentiation of W with respect to **B**. For an isotropic material, $\boldsymbol{\sigma}$ is written as [35]:

$$\boldsymbol{\sigma} = \frac{1}{J}\mathbf{B}\cdot\frac{\partial W}{\partial \mathbf{B}}\ ,\ J = \sqrt{I_3} \tag{2.3}$$

For a more accurate description of the behavior of the a rubber, the material should be tested under similar conditions to its application and the experimental stress-strain curves should be reproduced by the constitutive equations of the hyperelastic model. Uniaxial mechanical tests are easier to conduct but are not sufficient to achieve proper model calibration. Therefore, some other experiments such as planar, biaxial, and volumetric tests may be performed in conjunction with uniaxial tests (tensile and compression). More details on hyperelastic models are given in the Section 2.5 (page 18).

2.3 Finite Element Modeling

An FE analysis starts from a physical problem, expressed in a mathematical model to be solved. The FE model is used to solve complex engineering problems, but it is important to note that the solution of FE analyses can never give more information than the mathematical model itself [36]. In Figure 2.5, a FE analysis procedure is presented. For example, the physical problem may involve a structural component under mechanical loading. The idealization of this physical problem requires assumptions that lead to the formulation of differential equations, which can be solved by the FEM. Since the FE solution stews from a numerical analysis, it is necessary to verify its accuracy by varying the analysis parameters such as the mesh density or the type of element.

FE modeling of RMP is complex and challenging, involving large deformations, contact models, and complex constitutive models to represent the powder and flexible rubber mold. For these analyses, Abaqus implicit FE commercial software was used. The constitutive models were calibrated from mechanical tests. In the analyses, it is possible to estimate, among others, the final geometry of the compact and its density distribution, and these variables will be used to better understand the process and design a suitable numerical tool for improving pressing.

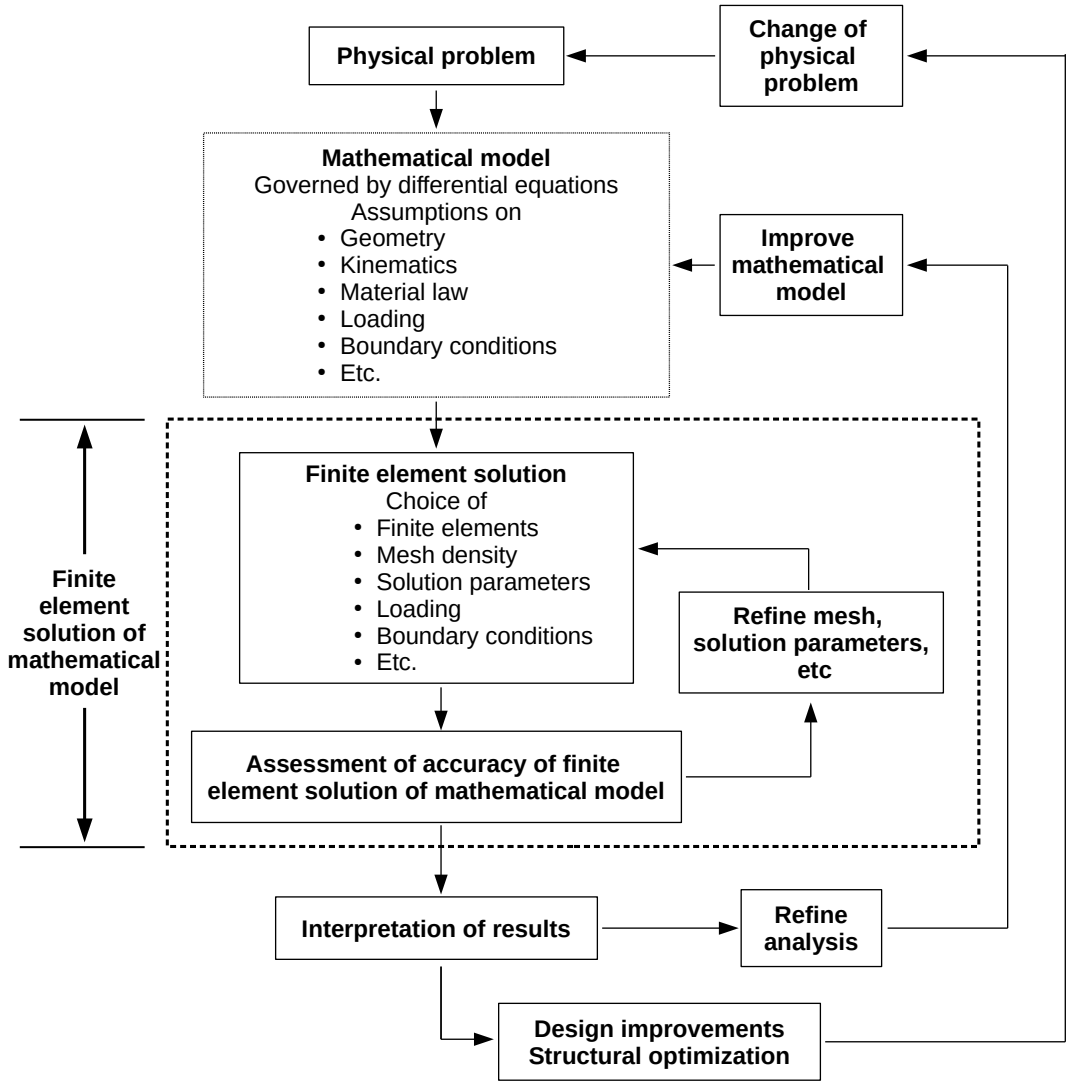

Figure 2.5 Process of FE analysis, adapted from Bathe [36].

2.4 Constitutive models for powder pressing

The phenomenological models used in FE representation of powder pressing are generally elastoplastic models described by ellipses in the Mises equivalent stress q vs. pressure p plane [37–39]. Both invariants are defined by

$$p = -\frac{1}{3}\,tr\,(\boldsymbol{\sigma}) \qquad \text{and} \qquad q = \sqrt{\frac{3}{2}(\mathbf{S} : \mathbf{S})} \tag{2.4}$$

where $\boldsymbol{\sigma}$ is the Cauchy stress tensor and $\mathbf{S}$ is its deviatoric part.

In uniaxial elastoplasticity, the yield stress delimits the elastic and plastic regimes.

In multiaxial loads, a surface, namely the yield surface, in the space of principal stresses delimits these two regimes. For stress states that are within the yield surface, the material response is elastic. Plastic strains occur only when the stress state is on this surface. Another way to represent the yield surface F is to write it as a function of p, q and state variables.

$$F = F(p, q, \text{state}) = 0 \tag{2.5}$$

Therefore F is a function of two scalars (p and q) and the state of plastic strain in the material. It is also convenient to analyze the material response in terms of increments of plastic strain. Again, the volumetric and deviatoric parts are separated, where $d\varepsilon_v^p$ is the increment of volumetric plastic strain and $d\bar{\varepsilon}^p$ is the increment of plastic deviatoric strain. An increment of volumetric plastic strain may be related to permanent volumetric change dV and the sample current volume V

$$d\varepsilon_v^p = \frac{dV}{V} \tag{2.6}$$

Equation(2.6) can also be written as function of density ρ or void ratio e. Thus, in the case of constitutive models for powder pressing, the state of plastic deformation in the yield function is represented by ρ or e

$$F = F(q, p, \rho \text{ or } e) \tag{2.7}$$

Green-Shima-Oyane model

The first contributions to a constitutive model of powder pressing were made by Green [40] and by Shima and Oyane [41]. In the so-called Green-Shima-Oyane (GSO) model, the yield surface is an ellipse centered at the origin, described in the p vs. q plane (Figure 2.6), whose size and proportion are functions of compact density (Equation 2.7). As density increases, the yield surface F expands and larger stresses are required to deform the compact plastically. It is convenient to express F in the normalized form

$$F = \sqrt{\left(\frac{p}{p_0(\rho)}\right)^2 + \left(\frac{q}{q_0(\rho)}\right)^2} - 1 = 0 \tag{2.8}$$

where $p_0(\rho)$ and $q_0(\rho)$ are functions of density. These variables are simply the two axes of the elliptic yield surface, as illustrated in Figure 2.6. The response is elastic for any loading history within the ellipse and plastic deformation only occurs if the stress state is on the yield surface.

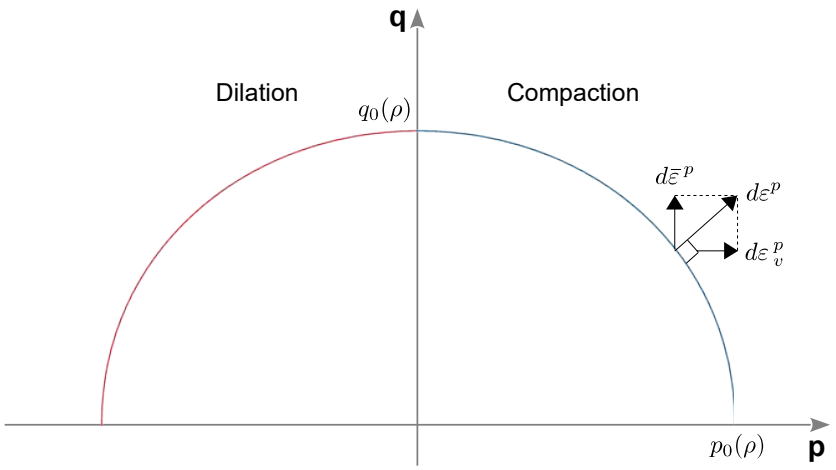

Figure 2.6 Yield surface of Green-Shima-Oyane model (GSO)

In a compact deforming plastically, there may be increments of volumetric plastic strain $d\varepsilon_v^p$ and of deviatoric plastic strain $d\bar{\varepsilon}^p$. Pressure p represents the tendency of material volume change and ε_v^p is the measure of permanent volume change. On the other hand, Mises stress q represents the tendency to distortion of the material and $\bar{\varepsilon}^p$ is its measure. Figure 2.6 shows the vector representing the plastic increment with the volumetric and deviatoric components. Drucker [42] described a stability postulate for the deformation of a material, in which the work performed by additional stresses of an arbitrary point in the stress space for any loading path must be non-negative ($d\sigma : d\varepsilon \geq 0$). The author demonstrated that for this condition to be satisfied the increment of plastic strain must be perpendicular to the yield surface. Note that for any p vs. q plane loading path where p is positive (compression), the GSO model will result in a negative volumetric plastic strain

increment ($d\varepsilon_v^p \leq 0$, compaction). Montilha et al. [43] performed a uniaxial compression test ($p > 0$) of a green alumina compact and verified that at some point of loading the material expanded, *i.e.,* there was a positive increment of volumetric strain. This phenomenon is called dilatancy. Therefore, the GSO model is not able to represent dilatancy in the compressive-side of p vs. q plane, as observed for an alumina compact.

Modified Cam-clay model

The modified Cam-Clay (MCC) [44] is a plasticity model that also presents an elliptical yield surface [45]. In its simplest form, MCC is described by a translation of the yield surface defined in the GSO model (Figure 2.7). The flow surface of the MCC model is defined as

$$F = \frac{1}{\beta^2}\left(\frac{p}{a} - 1\right)^2 + \left(\frac{q}{Ma}\right)^2 - 1 = 0 \tag{2.9}$$

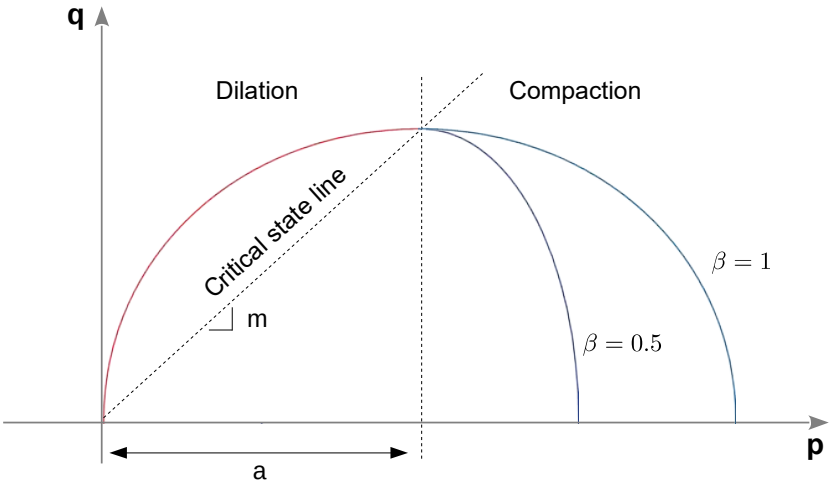

Figure 2.7 Modified Cam-Clay model implemented in Abaqus® software [27].

In Equation 2.9, the parameter a is related to the size of the yield surface, and M is related to the shape of the yield surface. If the parameter β is less than one, the yield surface consists of two distinct elliptical curves. If the β parameter is equal to the unit (β = 1), the yield surface is described by the same

ellipse. To simply represent the model by an elliptical curve, β = 1. Thus, in this particular case, the yield surface only depends on two unknown parameters M and a, therefore, two distinct loading paths are sufficient to characterize the model parameters. The critical state line divides the yield surface into two distinct responses: softening (dilation) on its left side and hardening (compaction) on its right side.

Drucker-Prager/Cap model

The Drucker-Prager/Cap (DPC) [27, 46] model has its yield function defined by three surfaces in the p vs. q plane: the so-called Drucker-Prager surface, the Cap surface and a transition surface, as shown in Figure 2.8.

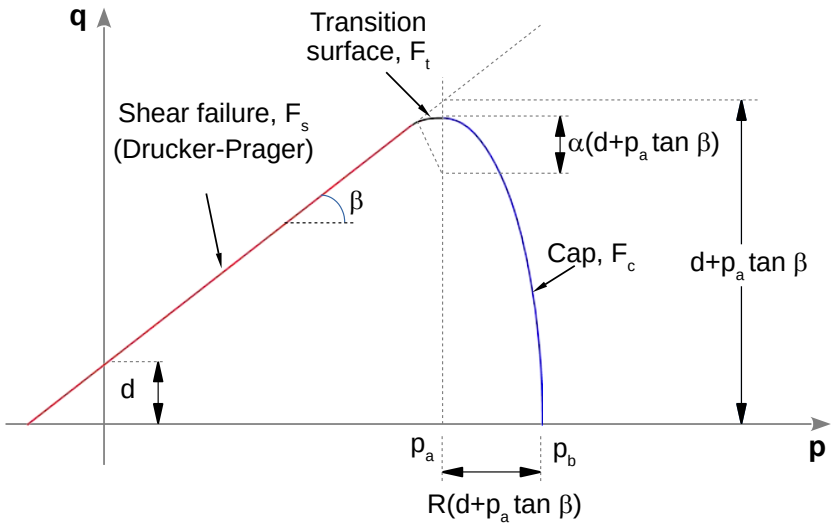

Figure 2.8 Yield surface of the DPC model implemented in Abaqus® [27].

The Drucker-Prager surface, F_s, is defined by

$$F_s = q - p\tan(\beta) - d = 0 \tag{2.10}$$

where d is the cohesion, and β is the internal friction angle of the material. Thus, when shear-driven plasticity occurs, the plastic flow mechanism is governed by friction and sliding between particles, resulting in particle decompaction and material expansion. The Drucker-Prager model is said to be non-associative, where

the flow rule is distinct from the yield surface. Non-associative flow rules best represent the dilatancy phenomenon in granular materials [47].

The Cap surface, F_c, introduces the material sensitivity to hydrostatic stress states (mechanical densification) and is defined by

$$F_c = \sqrt{(p - p_a)^2 + \left[\frac{Rq}{1 + \alpha - \frac{\alpha}{\cos(\beta)}}\right]^2} - R\left[d + p_a \tan(\beta)\right] = 0 \tag{2.11}$$

where R is the material parameter that controls the shape of the Cap, p_a an evolution parameter, and α a constant that ensures a smooth transition between Drucker-Prager and Cap surfaces. The parameter α has no physical meaning, and thus it is recommended to use small values (zero whenever possible).

When compaction occurs, plastic flow is dominated by densification and packing of the particles. Thus, the Cap surface, F_c, and its hardening law describe this mechanism. The transition surface, F_t, connects F_s and F_c, ensuring smoothness of the flow function necessary to avoid numerical errors and instabilities. The hardening curve specified for this model interprets flow so that the hydrostatic stress (p_b) is defined as a function of volumetric plastic deformation (ε_v^p).

The DPC parameters depend on the physical characteristics of the studied powder system [8]. Table 2.2 shows values of d, β and R for various alumina powder systems and some values of the coefficient of friction between alumina powder and the matrix walls (μ), highlighting a significant difference between the data.

Table 2.2 Main parameters of DPC constitutive model and friction coefficient between alumina powder and die walls obtained from the literature

Reference	Material	d [MPa]	β [°]	R	μ
Aydin et al. (1996) [5]	99.99 % α-Al_2O_3	5.5	16.5	0.558	0.3
Aydin et al. (1997) [48]	99.99 % α-Al_2O_3	5.5*	16.5*	0.558*	0.2
Zipse, H. (1997) [6]	Al_2O_3 with 10% of ZrO_2	0.1	65	0.5	0.23
Zeuch et al. (2001) [8]	94% Al_2O_3	2.3	26.7	1.77	-
Zeuch et al. (2001) [8]	99.5% Al_2O_3	4.2	28.5	1.405	-
Canto et al. (2003) [10]	α-Al_2O_3	3.0	16.5*	0.558*	0.2
Shin H. and Kim J-B (2015) [14]	Al_2O_3	4	44	0.25 - 0.5	-
Le Corre et al. (2017) [15]	Mesoporous alumina	30	43	0.638	-
Le Corre et al. (2017) [15]	Macroporous alumina	17	13	0.638	-

* Same parameters reported by Aydin et al. (1996) [5].

2.5 Hyperelastic models for rubbers

Several forms of energy density potential describe hyperelastic materials. These forms are based on the main stretch invariants or the main stretches themselves. Some treatments consider the material as incompressible ($J = 1$, Equation 2.1) to simplify the calibration and numerical implementation in FE softwares. In RMP, rubber compressibility directly affects the final dimensions of the compacted part, so this simplification should not be used. Some models capable of describing the mechanical behavior of elastomers are described hereafter. As proposed by Rivlin [31], a polynomial form for W is expressed as

$$W = \sum_{i,j=0}^{N} C_{ij}(\bar{I}_1 - 3)^i(\bar{I}_2 - 3)^j + \sum_{i=1}^{N} \frac{1}{D_i}(J-1)^{2i} \tag{2.12}$$

where C_{ij} and D_{ij} are material parameters. When the series is truncated in the first term, one obtains the so-called Neo-Hookean model

$$W = C_{10}(\bar{I}_1 - 3) + \frac{1}{D_1}(J-1)^2 \tag{2.13}$$

Considering only the first two terms of Equation 2.12, W first obtained by Mooney [30] is written as

$$W = C_{10}(\bar{I}_1 - 3) + C_{01}(\bar{I}_2 - 3) + \frac{1}{D_1}(J-1)^2. \tag{2.14}$$

Using an approach simply based on the main stretches, Ogden [32] proposed a specific form for the energy density potential

$$W = \sum_{i=1}^{N} \frac{2\mu_i}{\alpha_i^2}(\bar{\lambda}_1^{\alpha_i} + \bar{\lambda}_2^{\alpha_i} + \bar{\lambda}_3^{\alpha_i} - 3) + \sum_{i=1}^{N} \frac{1}{D_i}(J-1)^{2i} \tag{2.15}$$

where μ_i and α_i are real constant values, including non-integers.

In general, homogeneous deformation modes are sufficient to characterize the constants of the hyperelastic model. The most traditional tests used for this purpose are uniaxial and planar tension, uniaxial and planar compression, and volumetric compression [27] (Figure 2.9).

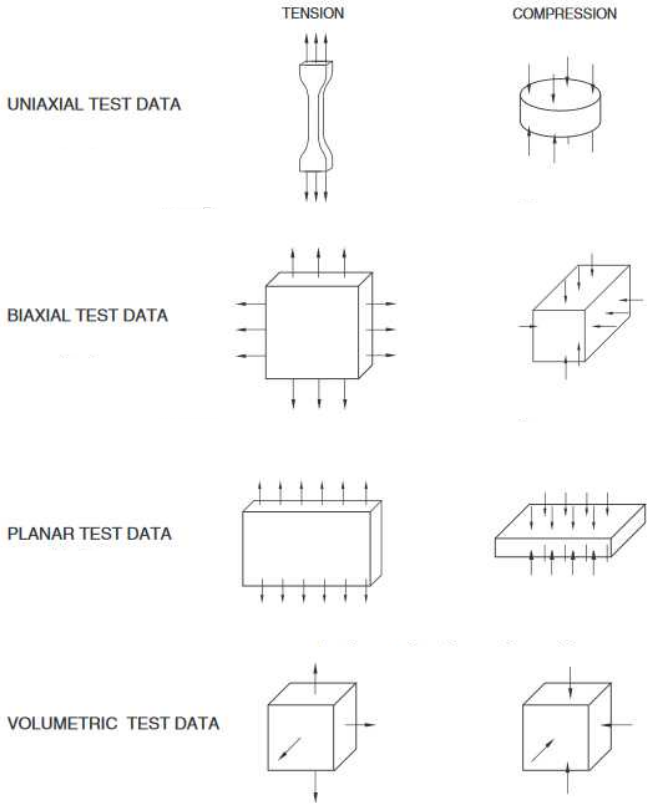

Figure 2.9 Deformation modes used in hyperelastic models calibration [27].

2.6 Rubber Multiaxial Pressing (RMP)

RMP pressing tool consists of three main parts: metallic pistons, flexible rubber mold and metallic rigid die. The powder is inserted into a cavity in the rubber mold as shown in Figure 2.10. In conventional uniaxial pressing, the powder is only pressed along the piston actuation axis. In RMP, pressing occurs in all directions by the action of the flexible rubber mold. This action is a consequence of quasi-incompressibility of rubber used in the flexible mold (under confined mechanical loading, the rubber changes its form with almost no change in volume). The volume of the cavity formed by the rigid parts (pistons and die walls) decreases with the motion of the piston. As the volume of the rubber mold does not decrease considerably, the volume of the powder cavity is reduced accordingly, thus the powder is densified.

The RMP process has several advantages as a pressing procedure [3]. The

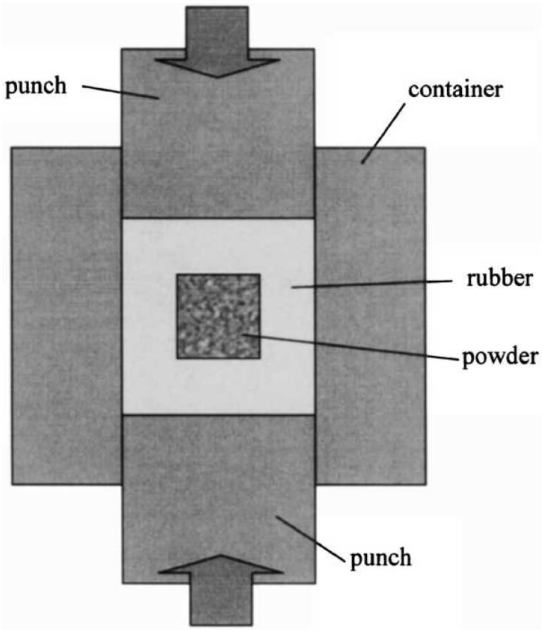

Figure 2.10 Rubber Multiaxial Pressing, adapted from Shima et al. [16].

procedure allows for the production of a wide variety of shapes such as helical gears, threads and long tubes (Figure 2.11). RMP is generally faster than isostatic pressing and yields compacts with homogeneous and adjustable density, which is not easily achieved by uniaxial pressing. Several types of powders can be used: ceramic, polymeric and metallic. Since in RMP there is no direct contact between the powder and the die walls, this process has advantages for pressing abrasive powders [3], *e.g.,* reducing tool wear. The rubber mold is easily made from a liquid resin which when mixed with its catalyst and poured into a cavity, cures and takes the form of the tooling. This route is also used in isostatic pressing molds [9].

Shima et al. [16] developed an elastoplastic analysis to study the fundamental characteristics of RMP, aiming to obtain near-net shape compacts. The Shima-Oyane model described in Section 2.4 was used to model powder compaction. Rubber was represented by a simplistic elastic model that considers the shear and bulk moduli dependent on volumetric strain. The model geometry and FE mesh are shown in Figure 2.12.

FE analyses were compared with experimental results with the same geom-

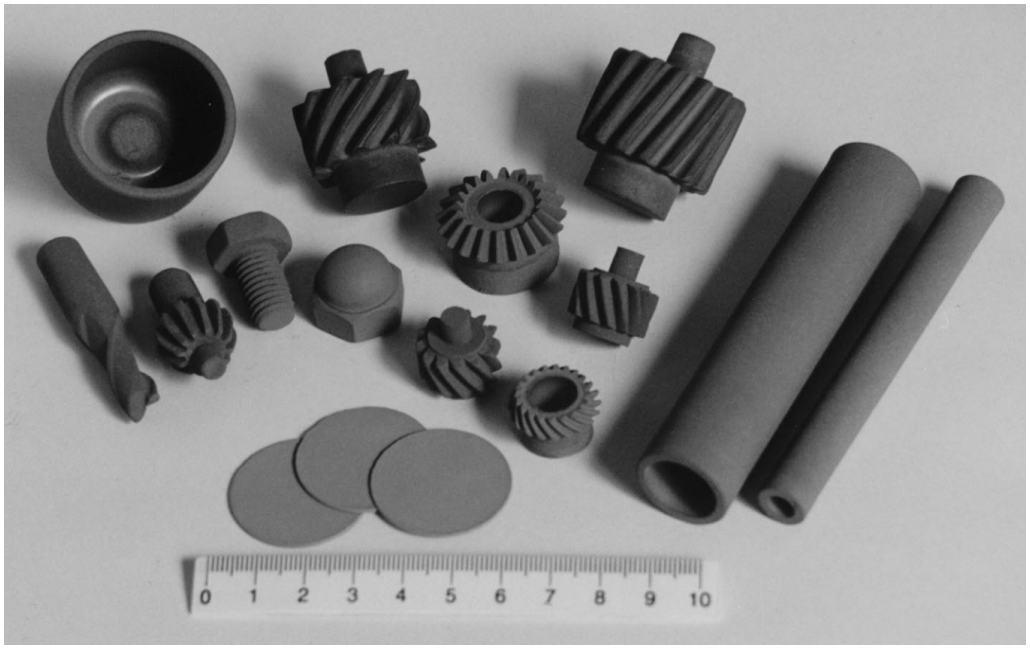

Figure 2.11 Green compacts of metallic powder processed through RMP, adapted from Sagawa et al. [3].

etry (Figure 2.10). The experiments were carried out with three different types of stainless steel powders (17-4PH PF-20, 17-4PH PF-20J e SUS440C PF) and using three different types of rubbers (KE12, KE112 and KE24) for flexible molds. The three elastomeric materials differed in hardness and compressibility, which is measured by the Poisson's ratio (Table 2.3). In particular, the Poisson's ratio has a large influence on the final geometry of the compact by determining the volumetric changes of the flexible mold. The thickness of the rubber mold is also a factor influencing the final shape of the green compact, the greater the thickness of the flexible mold, the greater the tendency of the compact to maintain the shape of the initial cavity, but the loads required for pressing the powder are higher.

Table 2.3 Poisson's ratio for rubbers used in the study of Shima et al. [16].

Rubber	KE12	KE112	KE24
Poisson's ratio	0.4997	0.4995	0.4988

In Figure 2.13, a result of RMP simulation using 17-4PH PF-20 powder and KE12 elastomer for the flexible mold is presented. The relative density distribution

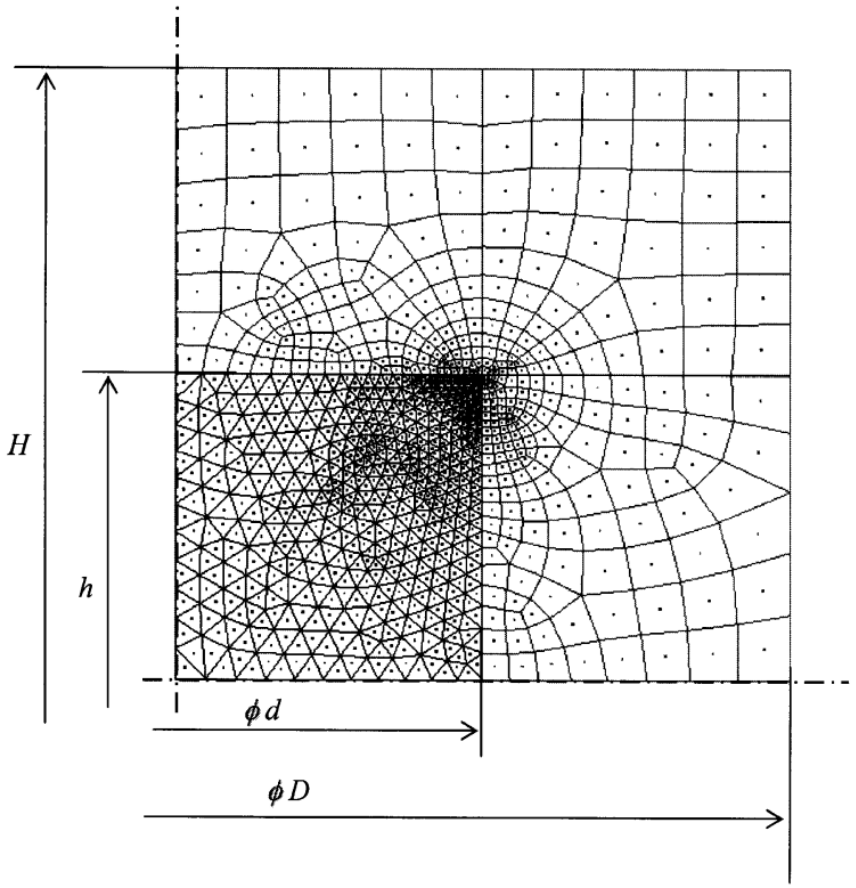

Figure 2.12 FE Model for RMP by Shima et al. [16].

and part geometry are shown in Figure 2.13(a). One may note that the upper and lower regions of the compact have larger diameters than the other portions. The density range is small in the compact except in corners. Shima et al. [16] stated that the fracture that usually occurs near the corner of the sample during unloading is associated with high density gradient. To observe the nodal displacements in the rubber during RMP, the rubber mold displacement vectors are shown in Figure 2.13(b) at a pressure of 50 MPa.

Shima et al. [16] proposed an optimization algorithm for the initial shape of the flexible mold cavity, aiming at a desired geometry for the green compact. In the algorithm, a desired shape with a certain relative density ρ_d was assumed. The initial relative density was called ρ_i, and the thickness of the flexible mold was considered twice as large as the main cavity dimension. The algorithm is divided into the following steps:

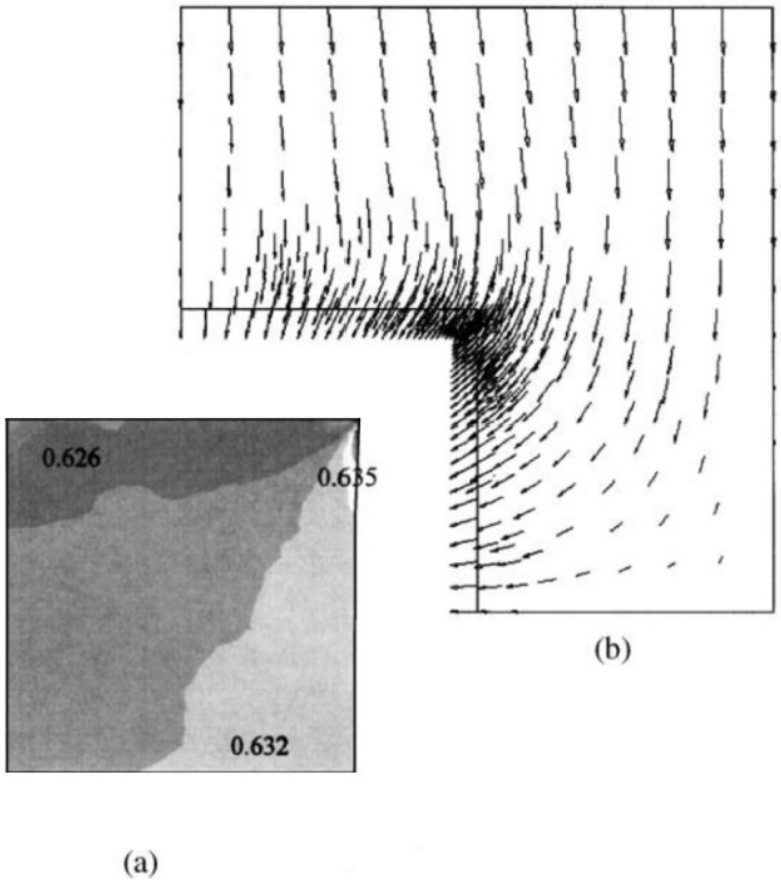

Figure 2.13 Simulation of RMP by Shima et al. [16] (metallic powder 17-4PH PF-20 and rubber KE12): (a) shape of the green compact and its density distribution e (b) vectors of displacement field in the rubber mold at a pressure of 50 MPa.

1. A hypothesis of isostatic pressing would result in an initial cavity with dimensions $\sqrt[3]{\rho_d/\rho_i}$ times larger than desired. This is a first estimation for the cavity dimensions. The nodes of the powder/mold interface are given a special name as shown in Figure 2.14(a);

2. Run an FE analysis of pressing with the estimated dimensions of the rubber mold cavity;

3. Calculate the difference between each deformed z coordinate of nodes $i, i+1, i+2...$ in the simulation (Figure 2.14(b)) and the z coordinate of the desired dimensions. Similarly, the difference between each deformed r coordinate of nodes $j, j+1, j+2...$ in the simulation is calculated and the R coordinates of the compact with optimal dimensions, and finally repeat the same procedure

with node k of the cavity vertices. These differences are called transposition magnitudes;

4. The starting positions of nodes $i, i+1, i+2...$ are corrected by repositioning them in the z direction according to the associated transposition magnitude. The same is true for nodes $j, j+1, j+2...$ in the r direction and node k at the geometry vertex (Figure 2.14(c));

5. Run the FE model again with the updated cavity geometry;

6. Iterate the procedure from 3 to 5 until the current and desired compact geometry reach acceptable match.

In this routine, a comparison is made between the shape of the rubber mold cavity in the compression stage with the desired shape for the green compact, with each iteration bringing these shapes closer together, resulting in ideal dimensions for the rubber mold cavity.

Yang et al. [17] studied the mechanical behavior of elastomers when pressing an aluminum alloy powder in cold isostatic pressing and RMP. The effect of thickness, rigidity of the elastomeric mold and friction between the surfaces of the tooling were studied. The authors used two different elastomers (silicone and Viton™) with two different thicknesses (5 and 10 mm). The Ogden hyperelastic model was used to analyze the deformation of elastomers. The GSO and Lee-Kim [49] models were used to represent the pressing of the powder. The results of the FE analyses were compared with experimental measurements and indicated an influence of the thickness of the rubber mold wall and of tribological conditions in the distribution of powder densities in RMP. In addition, the shape of the compact predicted with the Lee-Kim model was closer to that obtained experimentally in relation to the shape predicted with the GSO model.

2.7 Pressing of a ceramic femoral head for hip replacement

Already described as the surgery of the century [50], hip replacement is the substitution of the hip joint by a prosthesis. The modern prosthetic joint consists

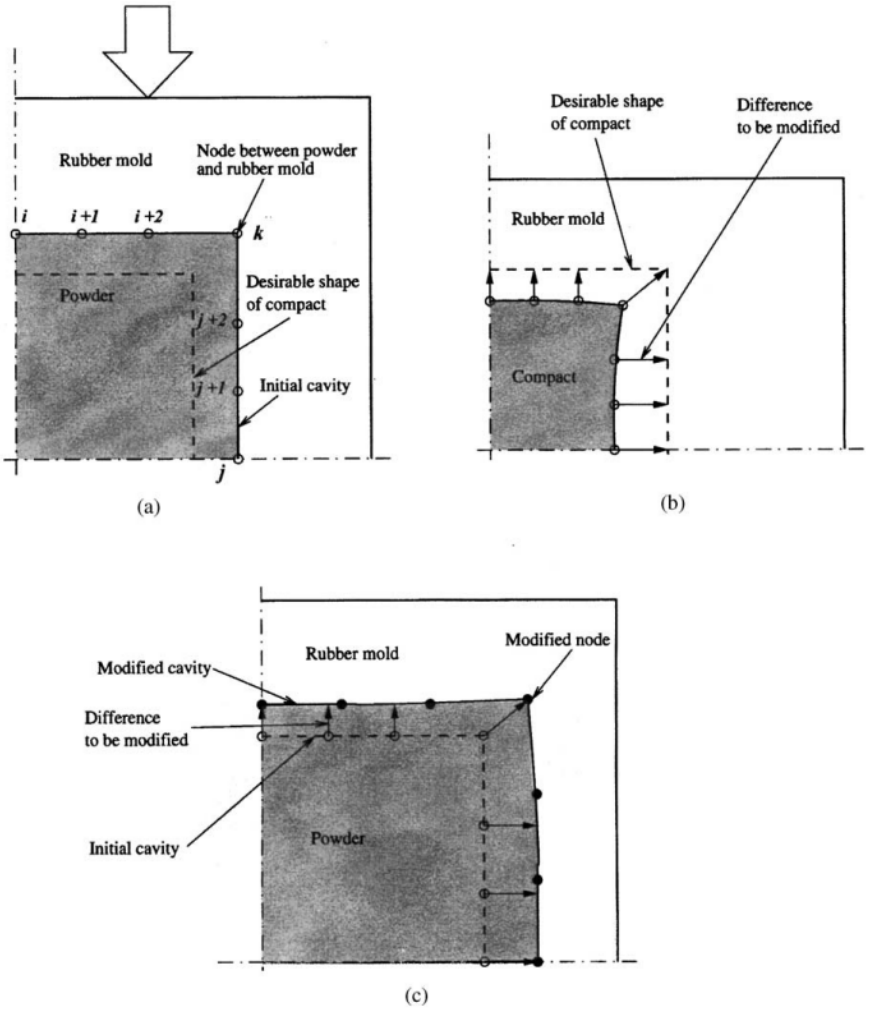

Figure 2.14 Rubber mold optimization by Shima et al. [16]: (a) Initial estimate for the rubber mold cavity; (b) result of the simulation with the initial rubber mold and (c) optimized rubber mold.

of four parts: an acetabular cup, a liner, a ceramic femoral head and a stem. These components are shown separately in Figure 2.15(a) and implanted in Figure 2.15(b). Ceramic-on-Ceramic bearing were introduced by Pierre Boutin in 1970 for applications in hip replacement [51]. Due to its biocompatibility, the CoC bearing has been an alternative to Metal-on-Polyethylene and Metal-on-Metal joints. The advantages of CoC bearing are mainly related to wear properties and low risk of intoxication [52].

Usually compacted by isostatic pressing and made of alumina powder, ceramic femoral heads are manufactured into the following steps [9]:

1. Isostatic pressing (wet bag);

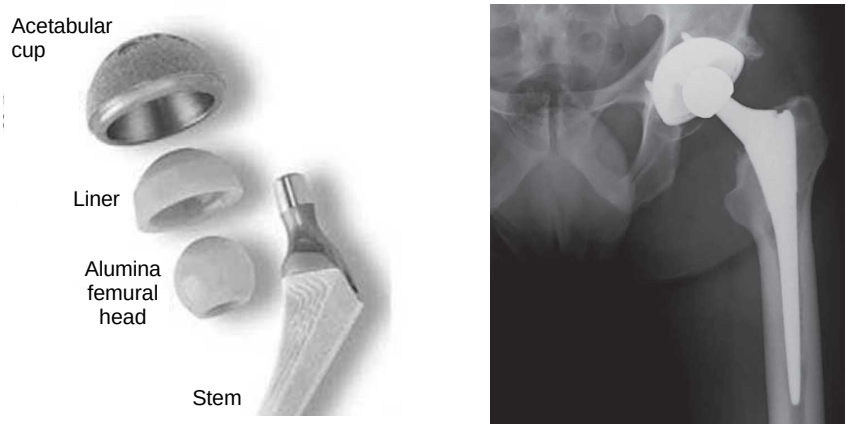

(a) (b)

Figure 2.15 Hip replacement: (a) components of prosthesis adapted from Capello et al. [53] and (b) X-Ray of the implant extracted from [50].

2. Machining of the green compact;

3. Firing;

4. Finishing.

Canto [9] has developed a methodology for manufacturing optimized isostatic pressing molds. The objective of the study was to produce a mold that would result in a compact with geometry close to the final shape intended for the part (near-net shape), reducing the material to be removed and green machining step. In Figures 2.16, the shapes of the ceramic femoral head are presented, respectively, after machining in green and after sintering and finishing.

The study in question used FE analyses to predict the final shape of the compact and obtain an adequate rubber mold design. The elastomeric material was modeled by the Mooney-Rivlin hyperelastic model. The metallic parts were considered as rigid analytical surfaces. The Drucker-Prager/Cap plasticity model was used to describe powder compaction. In Figure 2.17(a), the geometry of the appropriate mold design obtained by the study is described.

The mesh, boundary conditions and rigid analytical surfaces are shown in Figure 2.17(b). A uniform pressure of 100 MPa was applied to the outer surface of rubber. The contacts between powder/core, core/rubber and rubber/powder

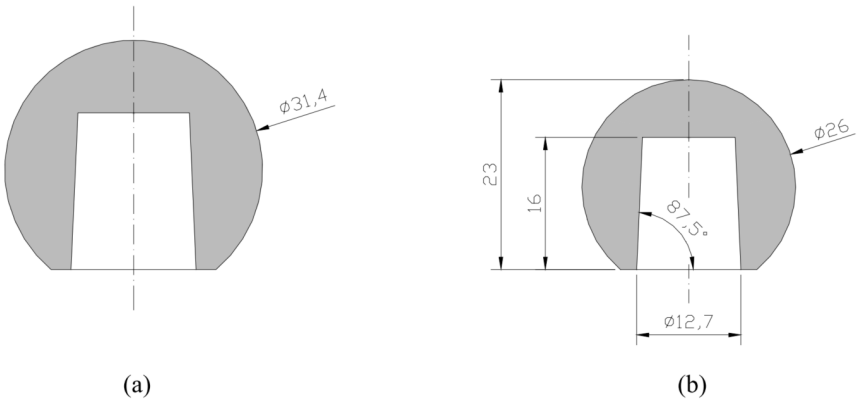

Figure 2.16 Ceramic femoral head for hip replacement: (a) Dimensions after green machining, and (b) after sintering and finishing, units in mm [9].

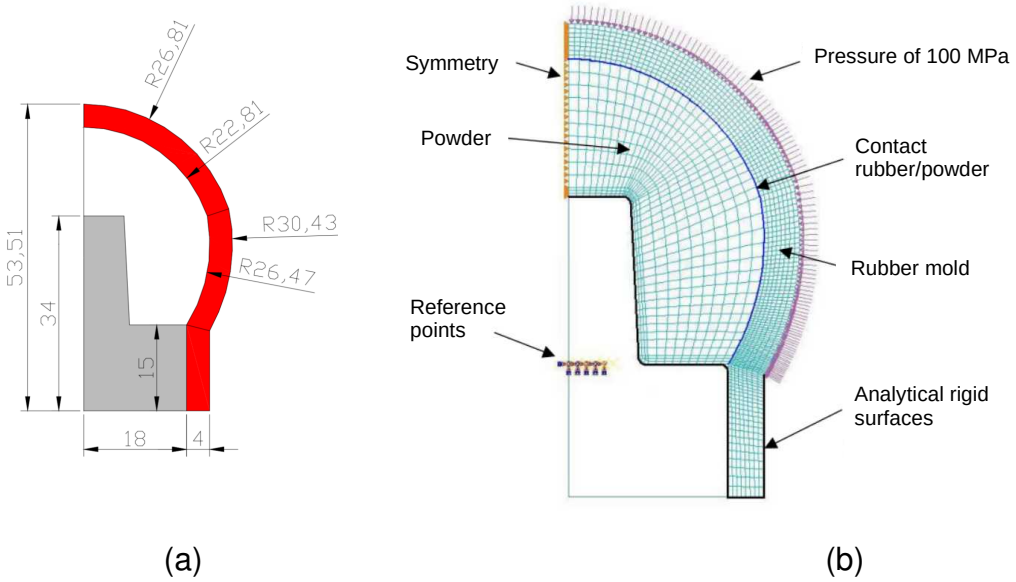

Figure 2.17 (a) Design of adequate rubber mold to the pressing of the ceramic head, and (b) axysimmetric FE model: mesh and boundary conditions [9].

were defined using, respectively, friction coefficients 0.05, 0.2 and 0.2.

The results of FE analysis were compared to those measured experimentally in the pressed part and to the intended geometry, both for the conventional mold, Figure 2.18(a), and for the optmized mold, Figure 2.18(b). The dimension estimated by the numerical analysis accurately depicts the shape of the isostatically pressed part. Only the region near the base of the compact has a more pronounced discrepancy between experimental and numerical results. This difference was attributed to numerical issues related to the contact model.

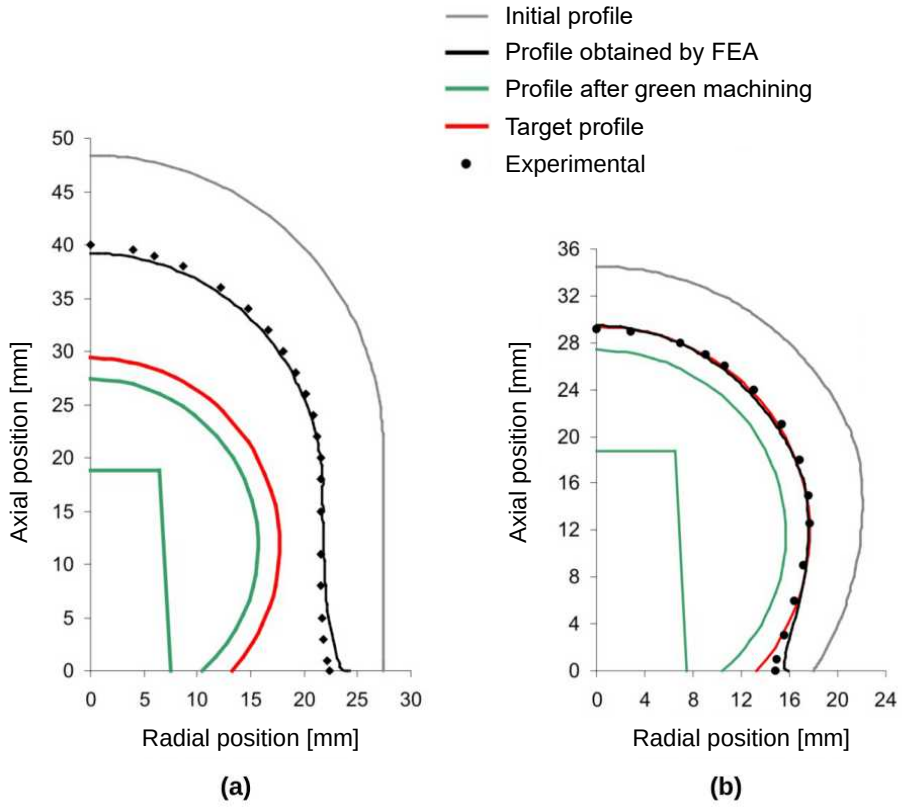

Figure 2.18 Numerical modelling of isostatic pressing for initial rubber mold (a) and optimized rubber mold (b) [9].

3 MATERIALS AND METHODS

> "When a theorist finds a new result nobody believes it, except him!
> When an experimentalist finds a whole new result the world believes in it, except him!"
> — Jean Lemaitre and Jean-Louis Chaboche, Mechanics of solid materials

In this chapter, firstly, the studied materials are described, *i.e.,* ceramic powder and rubber (Section 3.1 and 3.2). Furthermore, the methods employed in this work will be detailed as well. Section 3.3.1 describes an experimental procedure that may be used to validate the constitutive models for powder pressing. The experimental data was utilized to test a predefined set of DPC parameters obtained from the literature. Additionally, the data was employed to develop a preliminary model for the studied alumina powder. To further investigate the material properties of the compacted ceramic powder, a uniaxial compression test was performed in a cuboid specimen using the Digital Image Correlation (DIC), and made it possible to consider bending effects (Section 3.3.2). This procedure was then generalized to a multi-experiment analysis to mitigate the bias of using single test data (Section 3.3.3). To obtain some parameters of the DPC model, Brazilian tests were performed and analyzed with the results of the uniaxial compression tests (Section 3.3.4). Section 3.4 details the identification of the constitutive model for rubber and Section 3.5 describes how the identified material models were used to design and improve RMP for ceramic femoral head applications.

3.1 Ceramic powder

An atomized alumina powder is used in the present work. The average granule size is 75 μm. The measurement of loss on fire was 2.7 wt.% at 500 $^{\circ}$C for two

hours. The apparent density of the powder is 1.28 g/cm^3 and was obtained by direct measurements of the mass and volume of an amount of the powder in a graduated cylinder. The fully-dense density, obtained from Montilha et al. [43] was 3.74 g/cm^3, measured using a helium pycnometer. A microscopy of the powder is shown in Figure 3.1. The material was supplied by Ceraltec Cerâmica Técnica Ltda, from Brazil.

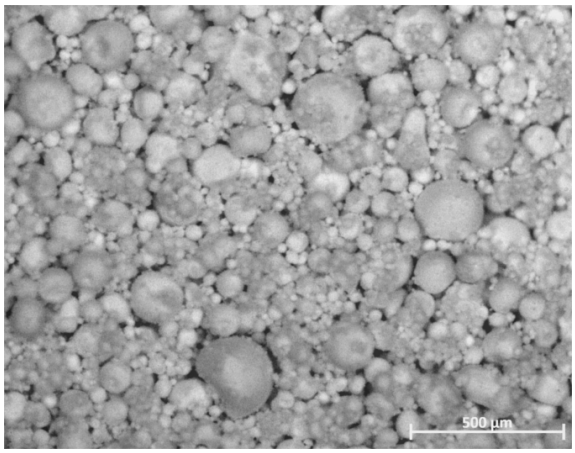

Figure 3.1 Microscopy of the studied ceramic powder acquired in a Zeiss Stemi 2000-C microscope [43]

3.2 Rubber

RenCast® 4464-1 is a two-component silicone rubber system, curable by polyaddition. This material has some interesting properties such as good fluidity to fill the counter-mold and make complex geometries, good mechanical strength in relation to other silicones, and high hardness [54]. These characteristics make rubber material an excellent candidate for the application of RMP. RenCast® 4464-1 is a polydimethylsiloxane rubber. This rubber has a linear chain of alternating silicon and oxygen (siloxanes), with a methyl radical attached to silicon atoms. Its good mechanical properties arises from the stability of its chemical bonds. The material shows low shrinkage during curing (less than 0.1% in its dimensions). Commercially, polydimethylsiloxane rubbers are known as RTV (Room Temperature Vulcanization), referring to the curing potential at room temperature. Table 3.1 summarizes the physical properties of RenCast® 4464-1 after curing.

Table 3.1 Physical properties of RenCast® 4464-1 rubber [54]

Property	Standard	Value
Hardeness, shore A	DIN 53505	41
Tear strength [N/mm]	ASTM D624B	158
Maximum stretching [%]	DIN 53504 S1	350
Tensile strength [MPa]	DIN 53504 S1	5.5
Coefficient of thermal expansion (0 up to 150°C) [$^{\circ}C^{-1}$]	ASTM D3386	2.5×10^{-4}
Linear contraction [%]	Standard mold	<0.1

3.3 Identification of constitutive model for powder compaction

A series of mechanical tests with alumina powder were performed in order to obtain the parameters of the constitutive model for powder compaction. Uniaxial compression tests, Brazilian tests, volumetric tests and closed-die (oedometric) tests were carried out and are further detailed in the following sections. In collaboration with Nicolas Schmitt during the internship at LMT, constitutive models for powder pressing and their identification were studied and some results presented in the next sections are the outcome of this investigation.

3.3.1 Preliminary identification/validation procedure for powder compaction model

The experimental procedure consists of two steps: closed-die uniaxial pressing, Figure 3.2(a), followed by isostatic pressing, Figure 3.2(b). In the first step, loose powder is introduced into the die cavity (I). The powder is then compacted in single-acting pressing (II), resulting in a cylindrical specimen with non-homogeneous density distribution (III) as a consequence of the friction between unlubricated die walls and powder [55]. The ejection is made removing the lower piston and moving down the upper piston (IV). In the second step, the compacted part (V) is isostatically pressed (VI and VII). In isostatic pressing, less compacted regions have a larger volumetric strain, thereby resulting in a shape that highlights the previous density gradient. The study presented hereafter was published [56] during the present work.

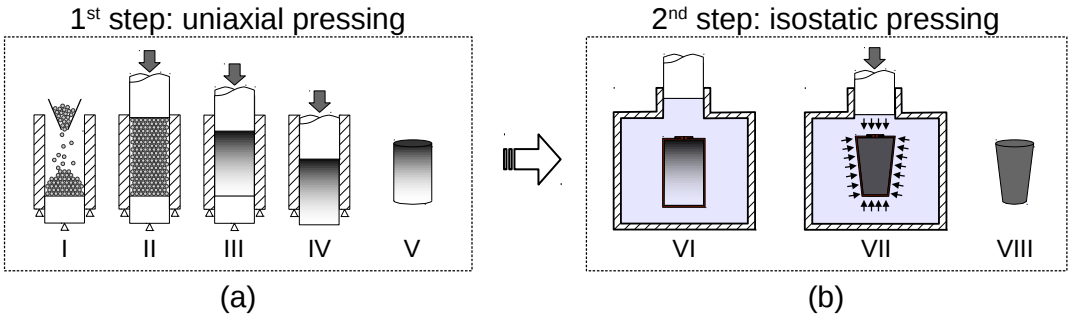

Figure 3.2 Steps of the experimental procedure: (a) Uniaxial and (b) isostatic pressing [56]

Uniaxial pressing

A rigid die with a cylindrical internal cavity and upper and lower pistons instrumented with pressure sensors was designed and fabricated as shown in Figure 3.3(a): the die is 300 mm high and has 50 mm of internal diameter, the pressure sensors, Figure 3.3(b), were designed according to Ref. [57]. In Figure 3.4, images highlighting apparatus details are shown.

The uniaxial pressing step (Figure 3.2a) was performed using an INSTRON universal testing machine, model 5500R, with a 250 kN capacity. The die cavity was filled with 500 g of alumina powder, resulting in an initial height of powder in the die cavity of ≈200 mm. The test proceeded with a loading followed by an unloading program was performed. A maximum load of 150 kN (equivalent to approximately 76 MPa in the inner cross-section area of the die) was reached during loading and the cross-head speed was 1 mm/min^{1}, as shown in Figure 3.5. After axial unloading, the green compact was ejected.

A polytetrafluoroethylene (PTFE) gasket was used to prevent the powder from entering the gap formed between the matrix and the upper piston. This gasket was formed *in situ*, using PTFE powder, resulting in a 5.5 mm high disc. This procedure ensures perfect coupling of the gasket with the die. The polymer was chosen because of its very low friction coefficient when in contact with steel. The entire system compliance (including the PTFE gasket) was measured with a previous mechanical test without alumina powder, and subtracted from the presented results. The aim of this first experimental step was to obtain a non-homogeneous

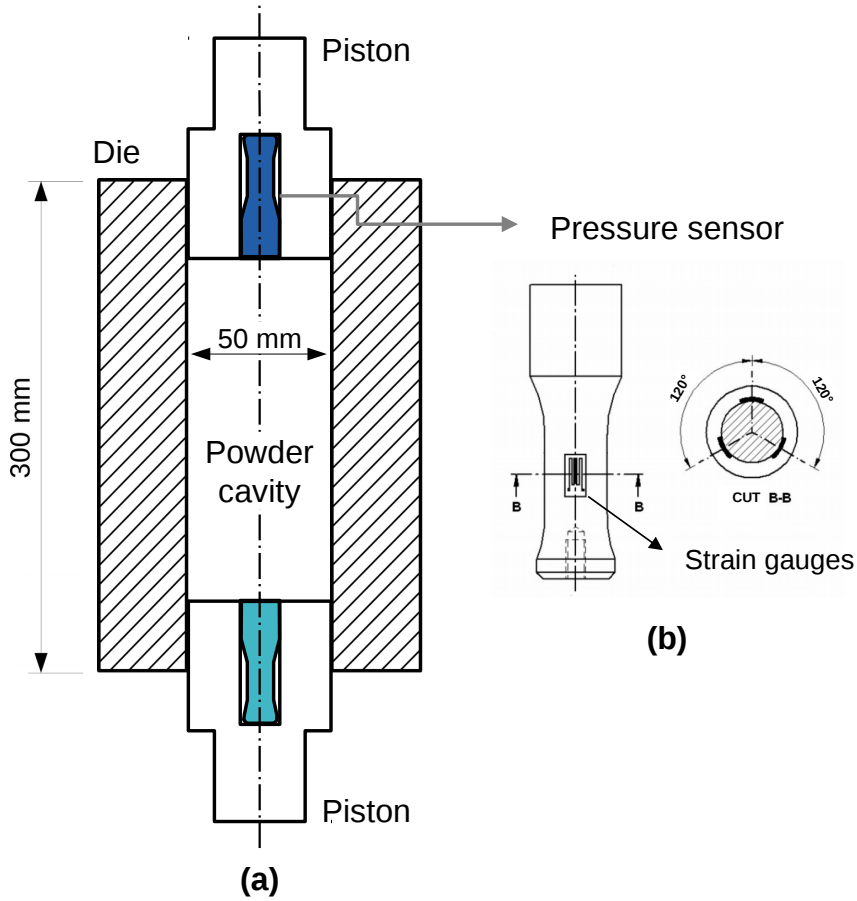

Figure 3.3 Cylindrical die (a) with a high height-to-diameter ratio to induce a density gradient along the height of the green compact powder, instrumented with two pressure sensors (b) [56]

Figure 3.4 Photographies of the (a) metal rigid die and (b,c) details of pistons-die walls assembly [56]

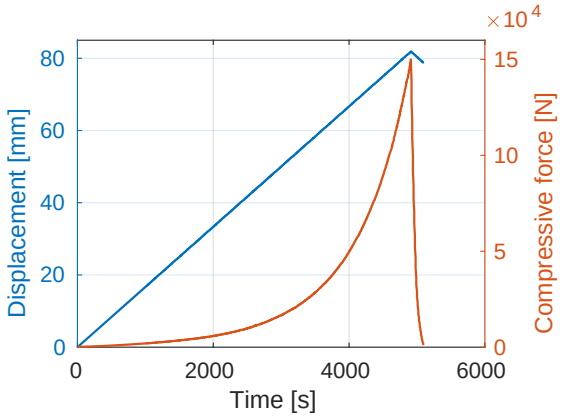

Figure 3.5 Uniaxial pressing test: Cross-head displacement (left) and force (right) vs. time [56]

green compact in terms of relative density, and to measure the difference of applied pressure between the top and the bottom surfaces of the compact during uniaxial pressing.

Isostatic pressing

This step was performed in an isostatic press AIP CP360, applying increasing pressures in two sequential stages: 25 and 200 MPa. At the end of each stage, a caliper (ABSOLUTE Digimatic, Mitutoyo Ltd, accuracy of 0.02 mm) was used to determine the non-regular cylindrical shape dimensions of the alumina compact, Figure 3.2(b) - VIII, by measuring the diameter of different heights.

Finite element model

The experimental configuration is axisymmetric and the finite element model was developed using this simplification for the sake of computational cost. The model is composed of four geometric parts: upper and lower pistons, die wall and ceramic powder. Simulation followed the same steps as the experimental procedure: uniaxial pressing (axial loading/unloading), ejection and isostatic pressing. For this analysis, the DPC model described in Section 2.4 was used.

The boundary conditions for the parts in each step are detailed in Figure 3.6. The lower piston had no displacement in y-direction (vertical) during the analyses. In the uniaxial pressing step (Figure 3.6a), the rigid part representing the die walls

was fixed. A force of 150 kN was prescribed in a reference point coupled to the analytical rigid surface, describing the upper piston. During axial unloading this force is gradually removed. The ejection was represented by the rigid die wall moving up, while the upper piston was set in the current position (Figure 3.6b). In the last step, a pressure of 25 MPa was applied on the external surfaces of the powder and removed, then the powder was re-pressed at 200 MPa and unloaded again. The coordinates X and Y of the nodes on the external surface of the powder part were extracted for comparison with the experimental profile of the green part after the two isostatic pressing stages (25 MPa and 200 MPa).

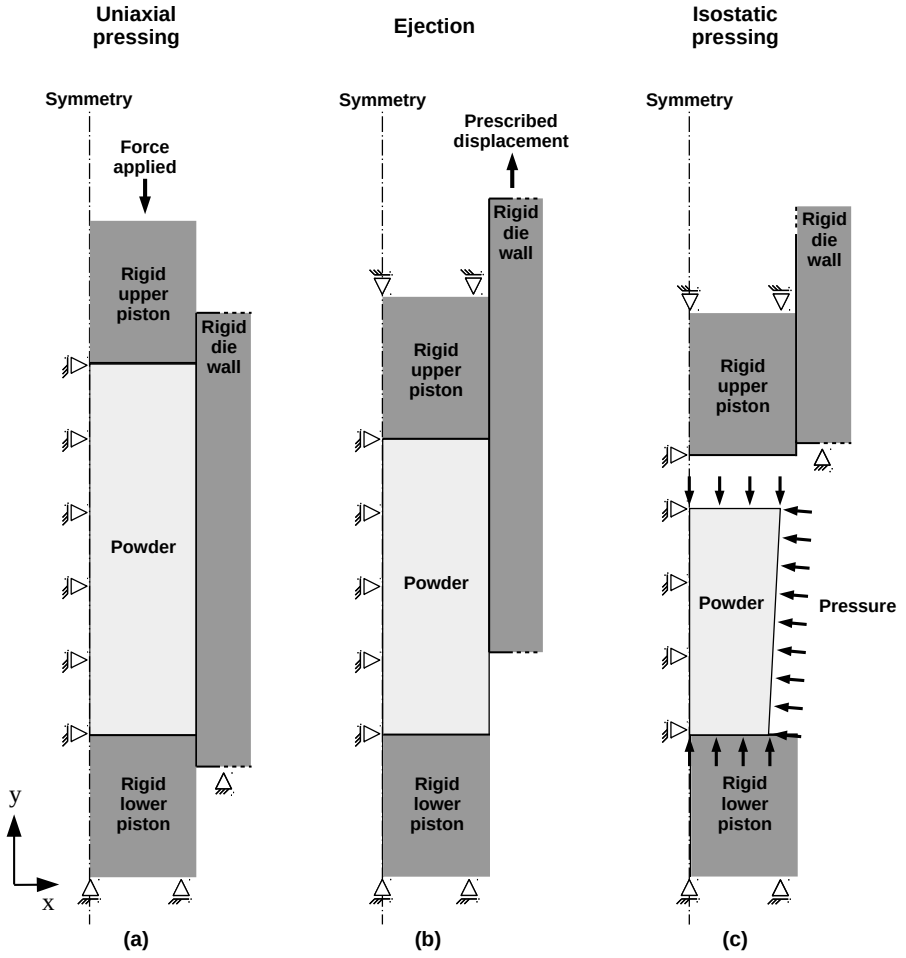

Figure 3.6 FE simulation of experimental procedure steps:
(a) Uniaxial pressing (axial loading/unloading, (b) ejection and (c) isostatic pressing [56]

The interactions between the powder and die parts were described via hard contact and Coulomb friction model. The coefficient of friction between the mold-

ing equipment and the powder was identified by inverse analysis, using brute-force optimization scheme to find the best match for this parameter (more detailed in Section 3.3.1). The die walls and pistons were modeled as analytical rigid surfaces. The DPC model was chosen to represent the powder and their parameters were identified by inverse analysis using pressure sensor data, as described in Section 3.3.1. Elasticity of the studied powder system was modeled as linear with a Young's modulus of 2.7 GPa and Poisson ratio of 0.13 [43]. The element type used in the powder was a 4-node bilinear quadrilateral (CAX4) and the total number of elements was 528. Geometric nonlinearity was considered to simulate the large strains of the powder during pressing.

Calibration with pressure sensor data

As the DPC parameters for the alumina powder system studied were not available, an inverse analysis based on the values of DPC parameters, shown in Table 2.2, was performed and the set of parameters that best suits the experimental and numerical data were determined. An automatized algorithm in Python programming language was developed to run simulations (In total, 1296 cases were run) with combinations of parameters set in a range of values shown in Table 3.2.

Table 3.2 Range of values used for the calibration of the model parameters

Parameters	Min.	Max.
Coefficient of friction, μ	0.2	0.3
Material cohesion, d [MPa]	0.05	7
Material angle of friction, β	15°	65°
Cap shape parameter, R	0.558	1.77

To determine the best match of experimental and numerical data, the minimum normal stress as a function of piston displacement of upper and lower pressure sensor was analyzed. In other words, the best match was found, minimizing the error defined by

$$E = \frac{|\sigma_{max}^{abq} - \sigma_{max}^{exp}|}{\sigma_{max}^{exp}} \tag{3.1}$$

where E is the error, and σ_{max}^{exp} and σ_{max}^{abq} the maximum absolute normal stress from pressure sensors measurement and numerical results, respectively.

Calibration of the cap hardening law using isostatic pressing tests

The hardening law was estimated by means of isostatic pressing tests and volumetric measurements performed with a caliper (ABSOLUTE Digimatic, Mitutoyo Ltd, accuracy of 0.02 mm) and precision weighing scales that resulted in a volumetric plastic strain vs. compaction pressure curve that was used as input for the simulations.

3.3.2 Uniaxial compression test with bending consideration using digital image correlation

Uniaxial compression is a well-known experimental procedure used to characterize the mechanical properties of metals, polymers, and ceramics, by establishing the relationship between the uniaxial stress state prescribed by the loading condition and the induced triaxial strain state [58]. For an ideal uniaxial compression test, a uniform stress state is expected to arise within the specimen. However, some artifacts may jeopardize this usually assumed stress homogeneity [59, 60]. Features of the test such as the lack of parallelism of the platens, and eccentric forces on the specimen, usually result in non-uniform stress states. Further, geometrical imperfections of the sample geometry may lead to similar issues. The difficulty of designing specimen and fixture parts to reach the desired stress states may lead to spurious data and erroneous identification of material parameters [61]. As reported in the ASTM C1424-10 standard: “actual studies of the effect of bending on the compressive strength distributions of advanced ceramics do not exist” [62]. Thus, the study presented hereafter aims to fill this gap. This study was fully developed during the internship at LMT in collaboration with François Hild and it was published in Ref. [63] during this thesis.

A uniaxial compression test was performed on a compacted alumina sample. Using Digital Image Correlation (DIC), the displacement fields of two perpendicular surfaces of the cuboid specimen were measured with two different

cameras. The DIC results showed bending effects in the displacement fields. To calibrate a constitutive model for the studied material, Finite Element Model Updating (FEMU) was applied, where DIC provided Dirichlet boundary conditions. The FEMU approach aimed to minimize a cost function based on the experimental and numerical reaction forces. Three different FEMU analyzes were implemented. The first approach, which corresponds to standard FEMU, uses the average axial strain assessed from DIC results and the forces to calibrate the constitutive model. The second one uses the displacements of the boundaries of the regions of interest for each camera separately (plane-stress hypotheses) to obtain the sought parameters. Last, a FEMU analysis with 3D considerations was carried out, using the multi-point constraint method to link the displacement fields of both analyzed surfaces. As a consequence of bending, the first two approaches give rise to two sets of different parameters for the constitutive model, showing that the more appropriate approach is the last one that considers the 3D nature of bending.

Material, experimental procedure and modeling of the test

The studied alumina powder was used to make the cuboid specimen. This process was divided into three steps, namely (i) isostatic pressing of alumina powder at a minimum pressure to handle the sample, (ii) manual sanding, and (iii) final isostatic pressing. In the first step, the specimen was preformed in an isostatic AIP CP360 press. The chosen pressure for this step was 10 MPa, which was enough to press green compacts that are not too brittle to handle, and prevent major distortions in the geometry of the specimen. In the second step, the remaining geometric distortions were corrected by sanding the specimen. Last, the specimen was recompacted at 100 MPa. The final geometry had cross-sectional dimensions of 20.3×20.3 mm^2, and height of 50.8 mm. Figure 3.7(a) shows the tested specimen between the platens of the testing machine. A random speckle pattern was sprayed onto the observed surfaces to increase the number of gray levels and contrast in the image and make DIC measurements possible.

The images were simultaneously acquired with two cameras monitoring two

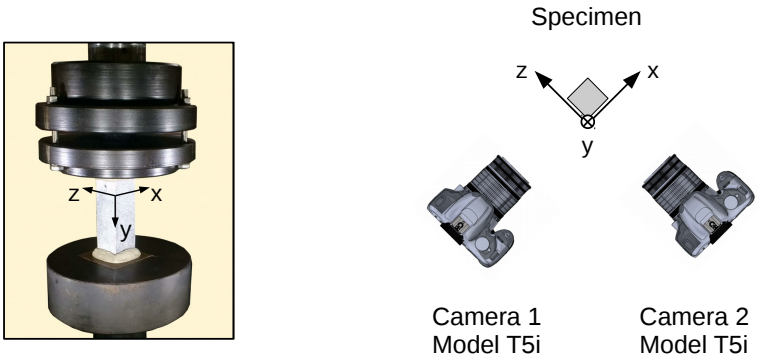

(a) (b)

Figure 3.7 Experimental setup. (a) Specimen between the testing machine platens ($20.3 \times 20.3 \times 50.8$ mm^3), and (b) upper schematic view of the camera disposition to image two adjacent lateral surfaces [63]

adjacent lateral surfaces (Figure 3.7(b)). The hardware parameters of the optical setup are gathered in Table 3.3.

Table 3.3 DIC hardware parameters [63]

Cameras	Canon T5 Rebel
Definition (raw)	3456×5184 pixels (Bayer pixels)
Color filter	Bayer
Gray Levels amplitude	8 bits
Lens	Canon 100-mm macro
Aperture	$f/5.6$
Field of view	40×60 mm^2
Image scale	11.6 | 10.9 µm/pixel (camera 1 | 2)
Stand-off distance	27 cm | 25 cm (camera 1 | 2)
Image acquisition rate	$0.05 - 0.17$ fps
Exposure time	1/60 s
Patterning technique	sprayed black paint
Pattern feature size♯	4 pixels (B/W)

♯evaluated as full width at half maximum of autocorrelation function

The test was performed in a series of loading-unloading cycles on a servohydraulic MTS Bionix testing system equipped with a 15 kN capacity load cell. To reduce the problems related to the lack of parallelism between the loaded surfaces, an epoxy resin was applied on the upper and lower parts of the specimen (see Figure 3.7a), this procedure does not affect the displacement measurement since it was computed by DIC technique and not by the cross-head displacement

registered by the test machine. The testing procedure, shown in Figure 3.8, consisted of four loading-unloading cycles, followed by a final loading until the force started to decrease. A cross-head speed of 0.1 mm/min was selected, and a preload of 30 N was applied. The number of acquired pictures was equal to 88 for both perpendicular faces.

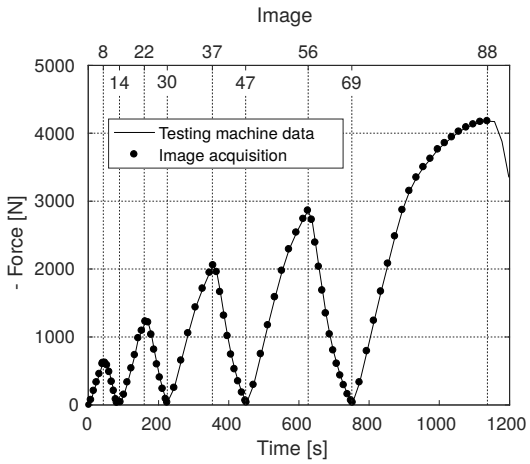

Figure 3.8 Force history showing the image acquisition instants (depicted with solid circles) [63]

The elastoplastic Drucker-Prager model with nonlinear hardening was chosen to represent the mechanical behavior of green compacted alumina since this powder (*i.e.,* unsintered ceramic) has a ductile mechanical behavior when considered as a continuous medium [43].

The hardening response was modeled with Voce's law [64]

$$\sigma_{ax} = \sigma_\infty - (\sigma_\infty - \sigma_y)\exp(-b\,\epsilon^p_{ax}) \tag{3.2}$$

where σ_{ax} is the axial stress, σ_∞ the compressive strength, σ_y the yield stress, b a hardening coefficient, and ϵ^p_{ax} the axial plastic strain. The elastic response of the material was considered linear and isotropic. One may note that the parameters d and σ_y are linearly dependent. For the analysis in this work, the identification (described in Section 3.3.2) was not sensitive to the Poisson's ratio ν and the friction angle β. Both values were taken from the literature [43, 56], respectively as $\nu = 0.13$ and $\beta = 55°$.

Digital Image Correlation and multi-point constraint

Global digital image correlation aims to find the displacement field $\mathbf{u}$ that minimizes globally the difference of the gray levels between a reference image f and a deformed image g corrected by the measured displacement. The corresponding (gray level) conservation law is written with the following cost function

$$\eta^2 = \sum_i^{N_i} [f(\mathbf{x}_i) - g(\mathbf{x}_i + \mathbf{u}_i)]^2 \tag{3.3}$$

where N_i is the number of pixels in the region of interest (ROI). To ensure a good conditioning of the minimization, the displacement of the *i-th* pixel $\mathbf{u}_i$ is represented by a set of degrees of freedom via finite element (FE) shape functions

$$\mathbf{u}_i = \mathbf{u}(\mathbf{x}_i) = \sum_j^{N_j} \phi_j(\mathbf{x}_i)\, a_j \tag{3.4}$$

where a_j are the nodal displacements, and $\phi_j(\mathbf{x}_i)$ the corresponding shape function.

To solve the minimization problem, an iterative scheme is proposed where the degrees of freedom $\{\mathbf{a}\}$ are decomposed as a current guess $\{\mathbf{a}\}^{(n)}$, and incremental updates $\{\delta\mathbf{a}\}$,

$$\{\mathbf{a}\}^{(n+1)} = \{\mathbf{a}\}^{(n)} + \{\delta\mathbf{a}\} \tag{3.5}$$

Linearizing the summand of the DIC cost function (3.3), the solution is found by solving the following linear system

$$[\mathbf{M}]\{\delta\mathbf{a}\} = \{\mathbf{b}\} \tag{3.6}$$

where

$$M_{jk} = \sum_{i=1}^{N_i} (\nabla f(\mathbf{x}_i) \cdot \phi_j(\mathbf{x}_i))\, (\phi_k(\mathbf{x}_i) \cdot \nabla f(\mathbf{x}_i)) \tag{3.7}$$

and

$$b_j = \sum_{i=1}^{N_i} (\nabla f(\mathbf{x}_i) \cdot \phi_j(\mathbf{x}_i))\, (f(\mathbf{x}_i) - \tilde{g}(\mathbf{x}_i)] \tag{3.8}$$

where $\tilde{g}(\mathbf{x}_i) = g(\mathbf{x} + \mathbf{u}^{(n)}(\mathbf{x}))$.

Constraint conditions, commonly applied in the FE method [65], are used to introduce additional relationships among degrees of freedom or couple separate regions together. To couple the common regions observed by both cameras, *i.e.,* one vertical line, the multi-point constraint (MPC) with the linear transformation method [66] was used herein. Alternative constraint procedures such as Lagrange multipliers and penalty methods could also be used. The Lagrange multiplier approach increases the number of equations of the linear system, while the selected method requires less effort than the others to assemble the global equations. On the other hand, the penalty method conserves the number of system variables but may lead to an ill-conditioned set of equations [67].

From Equation (3.6), the following linear system is written to determine the degrees of freedom from the separate image acquisitions independently

$$\begin{bmatrix} [\mathbf{M}^{c1}] & \mathbf{0} \\ \mathbf{0} & [\mathbf{M}^{c2}] \end{bmatrix} \begin{Bmatrix} \{\delta\mathbf{a}^{c1}\} \\ \{\delta\mathbf{a}^{c2}\} \end{Bmatrix} = \begin{Bmatrix} \{\mathbf{b}^{c1}\} \\ \{\mathbf{b}^{c2}\} \end{Bmatrix} \tag{3.9}$$

where $c1$ and $c2$ designate the two cameras. It is worth noting that the units of the nodal displacements $\{\mathbf{a}^{c1}\}$ and $\{\mathbf{a}^{c2}\}$ are pixels, which can have different physical dimensions for each camera, depending on the lens and the magnification. To have a better global perspective of the system variables, the pixel quantities are converted into usual units of length

$$\{\delta\overline{\mathbf{a}}^{c}\} = \{\delta\mathbf{a}^{c}\}\,\pi^{c} \quad \text{and} \quad \left\{\overline{\mathbf{b}}^{c}\right\} = \{\mathbf{b}^{c}\}\,\pi^{c} \tag{3.10}$$

where π^{c} is the physical size of one pixel for a photographed face by camera c. Converting the displacements and also the right-hand terms $\{b^{c}\}$, the linear system (3.9) is rewritten as

$$\begin{bmatrix} [\mathbf{M}^{c1}] & \mathbf{0} \\ \mathbf{0} & [\mathbf{M}^{c2}] \end{bmatrix} \begin{Bmatrix} \{\delta\overline{\mathbf{a}}^{c1}\} \\ \{\delta\overline{\mathbf{a}}^{c2}\} \end{Bmatrix} = \begin{Bmatrix} \left\{\overline{\mathbf{b}}^{c1}\right\} \\ \left\{\overline{\mathbf{b}}^{c2}\right\} \end{Bmatrix} \tag{3.11}$$

If there are two regions that can be coupled using the MPC method, a relationship between various degrees of freedom may be expressed as $\overline{a}_i^{c1} = \overline{a}_j^{c2}$. One can

write a linear transformation $[\mathbf{T}]$ linking all degrees of freedom ($\{\overline{\mathbf{a}}^{c1}\}$ and $\{\overline{\mathbf{a}}^{c2}\}$) to a unique vector with effective degrees of freedom $\{\overline{\mathbf{a}}^{g}\}$

$$\begin{Bmatrix} \{\delta\overline{\mathbf{a}}^{c1}\} \\ \{\delta\overline{\mathbf{a}}^{c2}\} \end{Bmatrix} = [\mathbf{T}]\ \{\delta\overline{\mathbf{a}}^{g}\} \tag{3.12}$$

The linear system concerning all *effective* degrees of freedom reads

$$[\mathbf{M}^{g}]\,\{\delta\overline{\mathbf{a}}^{g}\} = \{\overline{b}^{g}\} \tag{3.13}$$

with

$$[\mathbf{M}^{g}] = [\mathbf{T}]^{\top}\begin{bmatrix} [\mathbf{M}^{c1}] & \mathbf{0} \\ \mathbf{0} & [\mathbf{M}^{c2}] \end{bmatrix}[\mathbf{T}] \quad \text{and} \quad \{\overline{\mathbf{b}}^{g}\} = [\mathbf{T}]^{\top}\begin{Bmatrix} \{\overline{\mathbf{b}}^{c1}\} \\ \{\overline{\mathbf{b}}^{c2}\} \end{Bmatrix} \tag{3.14}$$

Another approach to couple two different regions is Lagrange's method with undetermined multipliers. This method can be use to evaluate the maximum or minimum of a function of two or more dependent variables, necessarily satisfying a prescribed relation. The DIC equations (3.6) and (3.9) have a clear analogy with FE structural analysis, where $[\mathbf{M}]$ would represent the stiffness, $[\delta\mathbf{a}]$ the degrees of freedom and b the forces. In this regard, one may calculate the balance of energy Π for this system, adding some unknowns λ multiplied by the prescribed relationship among degrees of freedom $[\mathbf{C}]$, which is the last term in Equation (3.15). It is worth noting that this term does not change the expression as it is equal to zero.

$$\Pi = \frac{1}{2}\begin{Bmatrix} \{\delta\overline{\mathbf{a}}^{c1}\} \\ \{\delta\overline{\mathbf{a}}^{c2}\} \end{Bmatrix}^{\top}\begin{bmatrix} [\mathbf{M}^{c1}] & \mathbf{0} \\ \mathbf{0} & [\mathbf{M}^{c2}] \end{bmatrix}\begin{Bmatrix} \{\delta\overline{\mathbf{a}}^{c1}\} \\ \{\delta\overline{\mathbf{a}}^{c2}\} \end{Bmatrix} - \begin{Bmatrix} \{\delta\overline{\mathbf{a}}^{c1}\} \\ \{\delta\overline{\mathbf{a}}^{c2}\} \end{Bmatrix}^{\top}\begin{Bmatrix} \{\overline{\mathbf{b}}^{c1}\} \\ \{\overline{\mathbf{b}}^{c2}\} \end{Bmatrix} + \{\lambda\}^{\top}[\mathbf{C}]\begin{Bmatrix} \{\delta\overline{\mathbf{a}}^{c1}\} \\ \{\delta\overline{\mathbf{a}}^{c2}\} \end{Bmatrix} \tag{3.15}$$

As the next step, one may differentiate Π with respect to the degrees of freedom and the Lagrange multipliers

$$\begin{bmatrix} [\mathbf{M}^{c1}] & \mathbf{0} & \\ \mathbf{0} & [\mathbf{M}^{c2}] & [\mathbf{C}]^{\top} \\ [\mathbf{C}] & & \mathbf{0} \end{bmatrix} \begin{Bmatrix} \{\delta\overline{\mathbf{a}}^{c1}\} \\ \{\delta\overline{\mathbf{a}}^{c2}\} \\ \{\lambda\} \end{Bmatrix} = \begin{Bmatrix} \{\overline{\mathbf{b}}^{c1}\} \\ \{\overline{\mathbf{b}}^{c2}\} \\ \mathbf{0} \end{Bmatrix} \tag{3.16}$$

The set of equations is solved for the degrees of freedom and Lagrange multipliers. $\{\lambda\}$ in structural analysis may be interpreted as forces of constraint. In this perspective, one may interpret $\{\lambda\}$ as the pseudo-force to couple two nodes together in the DIC analyses. This method increases the number of unknowns in comparison with the initial system, which suggests that it may better handle problems with lower multipoint constraints, in other words, $[\mathbf{C}]$ with smaller dimensions. An advantage is that in a non-linear problem, where the constraints are changing during the analysis, the part of the system containing $[\mathbf{M}^{c1}]$ and $[\mathbf{M}^{c2}]$ does not need to be refactored. This property can be valuable in representing contact or crack propagation problems in DIC analyses. This type of approach was used to account for perfect hinges in pantographic metamaterials [68].

The penalty method can be also used to enforce constraints. From the constraint relationship, one may define

$$\{\mathbf{t}\} = [\mathbf{C}] \begin{Bmatrix} \{\delta\overline{\mathbf{a}}^{c1}\} \\ \{\delta\overline{\mathbf{a}}^{c2}\} \end{Bmatrix} = \mathbf{0} \tag{3.17}$$

For this method, the term $(1/2)\{\mathbf{t}\}^{\top}[\boldsymbol{\alpha}]\{\mathbf{t}\}$ is added the balance of energy Π, where $[\boldsymbol{\alpha}]$ is a diagonal matrix of penalty values.

$$\Pi = \frac{1}{2} \begin{Bmatrix} \{\delta\overline{\mathbf{a}}^{c1}\} \\ \{\delta\overline{\mathbf{a}}^{c2}\} \end{Bmatrix}^{\top} \begin{bmatrix} [\mathbf{M}^{c1}] & \mathbf{0} \\ \mathbf{0} & [\mathbf{M}^{c2}] \end{bmatrix} \begin{Bmatrix} \{\delta\overline{\mathbf{a}}^{c1}\} \\ \{\delta\overline{\mathbf{a}}^{c2}\} \end{Bmatrix} - \begin{Bmatrix} \{\delta\overline{\mathbf{a}}^{c1}\} \\ \{\delta\overline{\mathbf{a}}^{c2}\} \end{Bmatrix}^{\top} \begin{Bmatrix} \{\overline{\mathbf{b}}^{c1}\} \\ \{\overline{\mathbf{b}}^{c2}\} \end{Bmatrix} + \frac{1}{2}\{\mathbf{t}\}^{\top}[\boldsymbol{\alpha}]\{\mathbf{t}\} \tag{3.18}$$

Minimizing Equation (3.17) by differentiating it with respect to the degrees of freedom, one obtains

$$\left(\begin{bmatrix} [\mathbf{M}^{c1}] & \mathbf{0} \\ \mathbf{0} & [\mathbf{M}^{c2}] \end{bmatrix} + [\mathbf{C}^{\top}][\boldsymbol{\alpha}][\mathbf{C}] \right) \begin{Bmatrix} \{\delta\overline{\mathbf{a}}^{c1}\} \\ \{\delta\overline{\mathbf{a}}^{c2}\} \end{Bmatrix} = \begin{Bmatrix} \{\overline{\mathbf{b}}^{c1}\} \\ \{\overline{\mathbf{b}}^{c2}\} \end{Bmatrix} \tag{3.19}$$

in which $[\mathbf{C}^{\intercal}][\boldsymbol{\alpha}][\mathbf{C}]$ is called the penalty matrix. If $[\boldsymbol{\alpha}]$ is null, constraints are ignored. As $[\boldsymbol{\alpha}]$ grows, the vector of degrees of freedom changes in such a way that constraints are better satisfied. The analyst is responsible for selecting appropriate values of the components in $[\boldsymbol{\alpha}]$. If all $[\boldsymbol{\alpha}]$ penalty numbers are the same, then $[\boldsymbol{\alpha}] = \alpha[\mathbf{I}]$, where $[\mathbf{I}]$ is the identity matrix, and Equation (3.19) simplifies slightly.

Vertical misplacement of the mesh boundaries on the two perpendicular analyzed faces of the specimen may lead to artifacts after coupling the displacements of nodes belonging to common edges, thereby resulting in inaccurate displacement fields (see Figure 4.8). To solve this problem, the optimization of the position of the mesh boundaries was conducted. The cost function (3.20) is based on the minimization of the global mismatch strain of the elements that contain a constrained node, as a shift in the position of the mesh boundaries causes spurious shear strains in these elements

$$e_s = \sum_{j}^{N_{im}} \sum_{i}^{N_e} \frac{\left[\epsilon_{12}^{(i,j)}\right]^2}{{\gamma_s}^2} \tag{3.20}$$

where ϵ_{12} denotes the (nodal) shear strain, γ_s the shear strain uncertainty estimated from ten images acquired before the test when the specimen was preloaded, N_{im} the number of images, and N_e the number of elements that contain constrained nodes.

Identification framework

In this study, Finite Element Model Updating (FEMU) is chosen as an identification method. FEMU is an approach to calibrate material parameters involved in mechanical tests by the development of an FE model of the mechanical test, and its comparison with experimental data [69–71]. The algorithm uses the results of DIC in FE models to minimize the distance between measured and predicted quantities. It is chosen to use the experimental geometry and the measured displacement fields as prescribed Dirichlet boundary conditions on the edges of the FE model. The cost function for the so-called FEMU-F route is based on the

differences between measured and computed reaction forces

$$\chi^2(\{\mathbf{p}\}) = \frac{1}{{\gamma_F}^2 n_t} \sum_t (F_m(t) - F_c(t, \{\mathbf{p}\}))^2 \tag{3.21}$$

where γ_F is the load uncertainty (on F_m), n_t the number of time increments, and F_c the computed reaction forces, which depend on material parameters gathered in the column vector $\{\mathbf{p}\}$. The identification methodology consists in a nonlinear least-squares minimization of this cost function.

Considering an initial guess for the set of parameters $\{\mathbf{p}_n\}$ at iteration n, the minimization is performed by calculating the correction $\{\delta\mathbf{p}\}$ from the linearized computed forces F_c

$$F_c(t, \{\mathbf{p}_n\} + \{\delta\mathbf{p}\}) \approx F_c(t, \{\mathbf{p}_n\}) + \frac{\partial F_c}{\partial \{\mathbf{p}\}}(t, \{\mathbf{p}_n\}) \; \{\delta\mathbf{p}\} \tag{3.22}$$

about the current estimate $\{\mathbf{p}_n\}$ of the sought parameters. The cost function then becomes

$$\chi^2(\{\delta\mathbf{p}\}) = \frac{1}{{\gamma_F}^2 n_t} \sum_t \left(F_m(t) - F_c(t, \{\mathbf{p}_n\}) - \frac{\partial F_c}{\partial \{\mathbf{p}\}}(t, \{\mathbf{p}_n\}) \; \{\delta\mathbf{p}\} \right)^2 \tag{3.23}$$

and its minimization with respect to $\{\delta\mathbf{p}\}$ leads to a linear system

$$[\mathbf{H}]\{\delta\mathbf{p}\} = \{\mathbf{h}\} \tag{3.24}$$

where $[\mathbf{H}]$ is the Hessian

$$[\mathbf{H}] = \sum_t \left(\frac{\partial F_c}{\partial \{\mathbf{p}\}}(t, \{\mathbf{p}_n\}) \right)^\mathsf{T} \frac{\partial F_c}{\partial \{\mathbf{p}\}}(t, \{\mathbf{p}_n\}) \tag{3.25}$$

$\{\mathbf{h}\}$ the right-hand member

$$\{\mathbf{h}\} = \sum_t \left(\frac{\partial F_c}{\partial \{\mathbf{p}\}}(t, \{\mathbf{p}_n\}) \right)^\mathsf{T} (F_m(t) - F_c(t, \{\mathbf{p}_n\}) \tag{3.26}$$

and $\frac{\partial F_c}{\partial \{\mathbf{p}\}}(t, \{\mathbf{p}_n\})$ the so-called sensitivity vector [72].

Three different FEMU approaches were used in this study (Table 3.4). First,

a classical analysis was conducted using a virtual DIC strain gauge (*i.e.,* averaging the axial strain results over the DIC mesh). An FE model with one element was used to fit the constitutive law with the experimental stress-strain curve. Prescribed displacements were applied, as depicted in Figure 3.9, to reach the same average strains as measured by DIC.

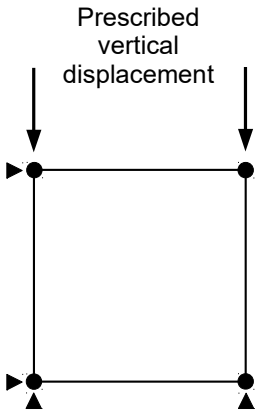

Figure 3.9 One-element model to calibrate material parameters via FEMU-F using uniform stress assumption [63]

Assuming uniform stress states, the reaction force is calculated and compared to the experimental load. With this approach, a FEMU scheme can be used to calibrate the material parameters. Moreover, a plane stress and a three-dimensional analysis were run to compare the FEMU results using the data from each face independently, and using data from both (coupled) faces in a 3D modeling, respectively.

For the plane stress analysis, the DIC meshes (with three-noded triangular elements) were used in the FE analyses. The vertical displacements obtained for each node in the upper and lower boundaries of the mesh (yellow circles in Figure 3.10(a-b)) were prescribed as Dirichlet boundary conditions. For each analyzed face, the horizontal displacement in the upper-left vertex was prescribed as zero to remove the rigid body translation along that direction.

In the 3D analysis, a hexahedron-element mesh was adopted. The vertical displacements were applied all over the cross-section of the upper and lower boundaries of the ROIs. For this purpose, the displacement fields obtained from

Table 3.4 Summary of calibration analyses [63]

Type of analysis	Coupled	Mesh boundary correction	Input for identification	FE model
Classical (plane stress)	×	✓	Average strain (DIC gauge)	1 four-noded element (CPS4) for each side
2D Plane Stress	×	✓	Prescribed DIC displacements on boundaries	170 three-noded elements (CPS3) for each side
3D Coupled	✓	✓	Prescribed DIC displacement on boundaries + extrapolations	490 eight-noded brick elements (C3D8)

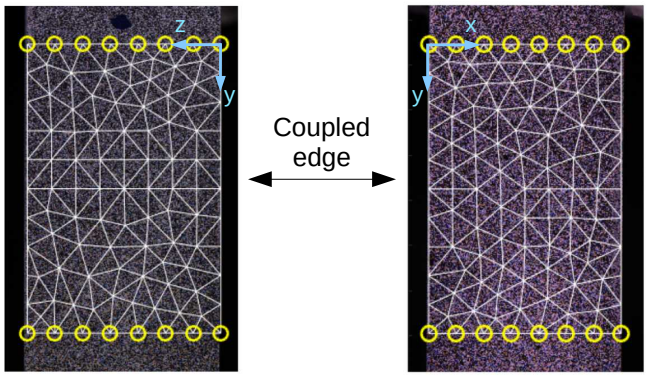

(a) (b)

Figure 3.10 Reference images with mesh and boundary conditions applied in the plane stress analysis of faces $y - z$ (a) and $x - y$ (b). The ROI dimensions where the mesh is defined are ≈ 30 mm in height and ≈ 20.3 mm in width [63]

DIC runs with MPC (Section 3.3.2) were used to fit, for the sake of simplicity, a plane. These results were then extrapolated for the vertical displacements inside the considered cross-sections of the specimen. Figure 3.11 shows these extrapolations for the first four force peaks (Figure 3.8), following the coordinate system defined in Figure 3.7 (*i.e.,* the vertical axis y is positive downward). The coefficients of the fitted planes were used as non-uniform distributions of displacement in the FE model using Abaqus® [73]. This approach allows the bending effect in the specimen to be represented as a measured displacements may induce nonuniform strain distributions.

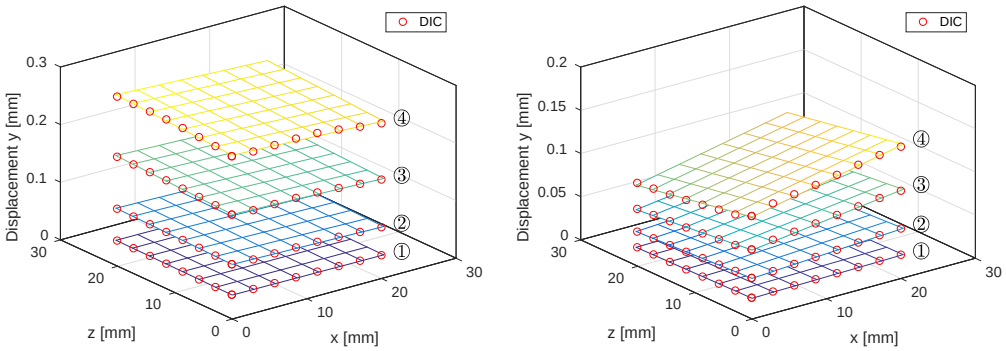

Figure 3.11 Extrapolated boundary conditions for the first four force peaks of (1 to 4): (a) top and (b) bottom surfaces of the 3D model. The red circles depict measured quantities [63]

3.3.3 Multi-test approach to identify a density-dependent constitutive model

A multi-test approach for the identification of a constitutive model is motivated by assumption that the model parameters must be valid for a number of tests and not biased by single test data. The following approach is based on the work of Neggers et al. [74] and also uses the framework described in Section 3.3.2. Equation (3.27) aggregates the cost functions of similar tests, Equation (3.21), in one single expression

$$\chi^2(\{\mathbf{p}\}) = \sum_{T}^{N_T} \chi_T^2(\{\mathbf{p}\}) = \sum_{T}^{N_T} \frac{1}{\gamma_F^2 \, n_t^{(T)}} \sum_{t} (F_m^{(T)}(t) - F_c^{(T)}(t, \{\mathbf{p}\}))^2 \tag{3.27}$$

where N_T is the number of tests. The approach to the numerical solution is the same as defined in Equation (3.24). Matrix $[\mathbf{M}]$ has now a contribution for each test

$$[\mathbf{H}] = \sum_{T}^{N_T} [\mathbf{H^{(T)}}] \tag{3.28}$$

and the right hand member

$$\{\mathbf{h}\} = \sum_{T}^{N_T} \{\mathbf{h^{(T)}}\} \tag{3.29}$$

Nine uniaxial compression tests were performed on cuboid specimens, manufactured with a procedure similar to that described in Section 3.3.2. The speci-

mens were isostatically pressed at 50, 100 and 200 MPa, which generated samples with different densities. The original Drucker-Prager model was also used to represent the material behavior and its parameters were identified for the analyzed specimen densities. The tests were performed with loading-unloading cycles on an electromechanical MTS testing system using a 30 kN capacity load cell. The testing procedure consisted of four loading-unloading cycles, followed by final loading until the force started to decrease. A cross-head speed of 0.1 mm/min was used and a preload of 30 N was applied. Table 3.5 summarizes some information about the tests. Images were acquired simultaneously on adjacent faces by two cameras, similarly to the experimental setup described in Section 3.3.2.

Table 3.5 Information about specimens and uniaxial compression tests [63]

Test	Dimensions [mm]			Compaction pressure [MPa]	Density [g cm^{-3}]	Number of images
	Thickness	Width	Height			
1	45.64	16.87	16.85	50	2.26	143
2	45.07	17.11	17.10	50	2.23	143
3	44.95	17.08	17.07	50	2.24	141
4	44.53	16.73	16.78	100	2.34	134
5	44.30	16.82	16.81	100	2.35	136
6	44.78	16.65	16.63	100	2.36	135
7	43.86	16.36	16.33	200	2.49	150
8	43.77	16.47	16.49	200	2.47	152
9	43.64	16.37	16.37	200	2.51	150

The hardware parameters of the optical setup are gathered in Table 3.6.

Table 3.6 DIC hardware parameters [63]

Cameras	Canon 5DS
Definition (raw)	8688×5792 pixels (Bayer pixels)
Color filter	Bayer
Gray Levels amplitude	8 bits
Lens	Canon 180-mm macro
Aperture	$f/18$
Field of view	30×45 mm^2
Image scale	8.4 µm/pixel
8 Stand-off distance	225 mm
Image acquisition rate	$0.03 - 0.29$ fps
Exposure time	1/13 s
Patterning technique	sprayed black paint
Pattern feature size♯	6 pixels (B/W)

♯evaluated as full width at half maximum of autocorrelation function

3.3.4 Diametral compression tests and evaluation of angle of friction for Drucker-Prager surface using dilatancy phenomenon

The angle of friction parameter β and material cohesion d are usually determined by analyzing the green compact strength in uniaxial compression test and diametral compression test, also called Brazilian test. Since the original Drucker-Prager model is represented by a linear function in p vs. q plane, two experiments are needed to determine its yield surface. For the Drucker-Prager parameter evaluation, three diametral compression tests were performed with specimens pressed at 100 MPa, using a similar manufacturing procedure as the specimens for uniaxial compression tests. The experimental set-up was similar to that described in Section 3.3.3. Table 3.7 summarizes the physical properties of the specimen and some information about the tests.

Table 3.7 Information about specimens and diametral compression tests

Test	Dimensions [mm]		Compaction pressure [MPa]	Density [g cm^{-3}]	Number of images
	Diameter	Thickness			
1	62.63	19.36	100	2.34	160
2	62.68	19.45	100	2.33	111
3	62.86	19.00	100	2.36	156

Images were acquired simultaneously of opposite faces by two cameras, using

a hardware and setup similar to that described in Table 3.6 (Section 3.3.3). The testing procedure, shown in Figure 3.12(a), consisted of three loading-unloading cycles, followed by a final loading until fracture of the specimen. A cross-head speed of 0.01 mm/min and a preload of 30 N were applied. Figure 3.12(b) shows an example of image from the specimen of Test 2, highlighting the mesh used in DIC analyses.

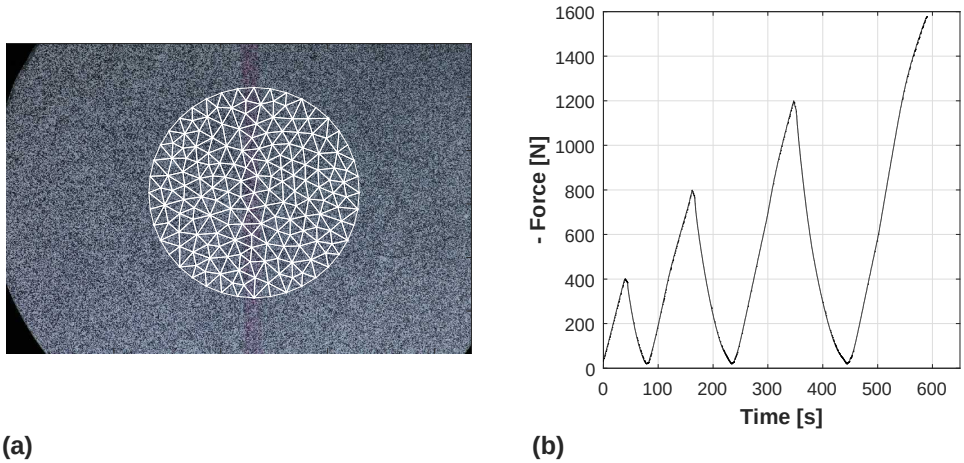

Figure 3.12 (a) Image of the specimen for Test 2 and (b) corresponding loading history.

The results of the diametral and uniaxial compression tests were analyzed using the approach described in Montilha et al. [43], using dilatancy to drive the identification of β. Dilatancy is defined as the change in the tendency of reduction in volumetric strain on a compressive stress state. In other words, the dilatancy point is here defined as the minimum value of volumetric strain during the test. To observe dilatancy, the evolution of the volumetric strain was measured using the DIC technique. This technique makes possible the evaluation of the in-plane strain tensor

$$[\varepsilon] = \begin{bmatrix} \varepsilon_{11} & \varepsilon_{12} \\ \varepsilon_{21} & \varepsilon_{22} \end{bmatrix} \tag{3.30}$$

where ε_{ij} are the components of the strain tensor.

For uniaxial compression, the transverse strain may be assumed as identical in the in-plane and out-of-plane directions ($\varepsilon_{33} = \varepsilon_{22}$). In that case, the volumetric

strain during the test was calculated as

$$\varepsilon_{vol}^{uc} = \varepsilon_{11} + 2\,\varepsilon_{22} \tag{3.31}$$

where direction 1 is the direction of the load applied to the specimen (axial) and direction 2 is perpendicular to direction 1 (transversal).

For diametral compression tests, the in-plane stress ε_{33} was neglected (strong assumption) and the volumetric strain calculated as

$$\varepsilon_{vol}^{dc} = \varepsilon_{11} + \varepsilon_{22} \tag{3.32}$$

The volumetric strain was measured during the mechanical test to identify the critical stress state, where an abrupt change in the mechanical behavior of the material is observed, that is, the specimen began to expand when subjected to a compressive stress state.

The values of minimum volumetric strain that represent dilatancy are associated with a stress state in the specimen from which the Mises stress (q) and pressure (p) are calculated. Equation (3.33) defines these variables for uniaxial compression.

$$p^{uc} = -\frac{\sigma_{11}}{3} \quad \text{and} \quad q^{uc} = -\,\sigma_{11} \tag{3.33}$$

and for diametral compression

$$p^{dc} = -\frac{2\,\sigma_{22}}{3} \quad \text{and} \quad q^{dc} = -\sqrt{13}\,\sigma_{22} \tag{3.34}$$

With this data, one may calculate the angle of friction using the Equation 3.35.

$$tan\beta = \frac{q^{uc} - q^{dc}}{p^{uc} - p^{dc}} \tag{3.35}$$

It is possible to find in the literature other methods to obtain β with the use of fracture stresses in Equation 3.35. The difference between both approaches will

be further discussed later.

3.4 Identification of constitutive model for rubber

Specimen manufacturing and experimental procedure

Specimens manufacture consisted of weighing the RenCast® 4644-1 components accurately and mixing the resin and the hardener together for at least 5 minutes, reaching a homogeneous mixture. The mixture was placed in a clean and dry mold and a vacuum system was used to reduce the occurrence of trapped air bubbles. Specimens were tested in three deformation modes: uniaxial compression, uniaxial tension and volumetric compression. The geometry of the specimen in the uniaxial tensile test followed the ASTM D412 standard. For uniaxial and volumetric compression, cylindrical specimens with a diameter of 20 mm and a respective height of 37.65 mm and 37.15 were used.

The uniaxial tensile test was performed in an MTS-Bionix Universal Servo-hydraulic Testing Machine with a 5 kN load cell and the cross-head speed was 10 mm/min, same speed was used in the other mechanical tests. The uniaxial compression and volumetric tests were conducted in an Instron 5500R testing machine equipped with a 250 kN load cell. In volumetric compression test, a closed die was used to confine the rubber specimen.

Identification framework

With data from the mechanical tests, the parameters of the hyperelastic models described in Section 2.5 can be obtained using an Abaqus® built-in calibration tool [73]. The FE software determines the material constants through two optimization algorithms depending on the hyperelastic model, which are the linear least-square procedure and the Levenberg-Marquard algorithm [75, 76]. In both algorithms, the error in stress is minimized through the relative error measure e for the three nominal stress and nominal strain data sets (uniaxial tensile, compression and volumetric test)

$$e = \sum_{i=1}^{n} \left[1 - \frac{T_i^F(\mathbf{p})}{T_i^E(\mathbf{p})} \right]^2 \tag{3.36}$$

where n is the number of data pairs, $\mathbf{p}$ the set of material parameters, $T_i^F(\mathbf{p})$ and $T_i^E(\mathbf{p})$ are respectively the numerical and experimental nominal axial stresses. For the full polynomial models, the linear least-squares method is used. A linear system is constructed from

$$\frac{\partial e}{\partial p_i} = 0 \tag{3.37}$$

and the materials parameters are obtained by its solution.

Some models as Ogden, Arruda-Boyce and Van der Waals have nonlinear energy potentials in relation to some of their coefficients [73]. Thus, a nonlinear least-squares-fit procedure is needed. In this case, Abaqus® software applies the Marquard-Levenberg algorithm to the formulation [77]. The material parameters are evaluated iteratively

$$p_i^{(r+1)} = p_i^{(r)} - \sum_{j=1}^{m} \sum_{k=1}^{n} \left[P_{ik}^{(r)} P_{jk}^{(r)} + \gamma \delta_{ij} \right]^{-1} P_{jk}^{(r)} E_k^{(r)} \tag{3.38}$$

where r is the iteration, m the number of coefficients of the model,

$$E_k = \frac{T_k^E - T_k^F}{T_k^E}$$

is the vector of relative errors, and

$$P_{ik} = \frac{\delta E_k}{\delta p_i} = -\frac{\delta T_k^F}{T_k^E \delta p_i}$$

the derivative of the vector of relative errors with respect to the coefficients $\mathbf{p}$.

3.5 Design, numerical and experimental simulation of RMP

Up to now, the discussed methodologies focused on finding trustworthy constitutive models for the powder and rubber. Once these steps are performed, RMP can then be modelled and its design improved. The tools for manufacturing the ceramic femoral head via RMP are composed of several parts, as depicted in

Figure 3.13. The rigid die is divided into two pistons and a die wall, all these parts are made of SAE 4340 steel. The flexible parts are the rubber mould and the rubber cap. The sealing rings are used to prevent rubber material from entering between the piston and die walls. A rigid mandrel, also made of SAE 4340 steel, is used to shape the internal part of the ceramic femoral head.

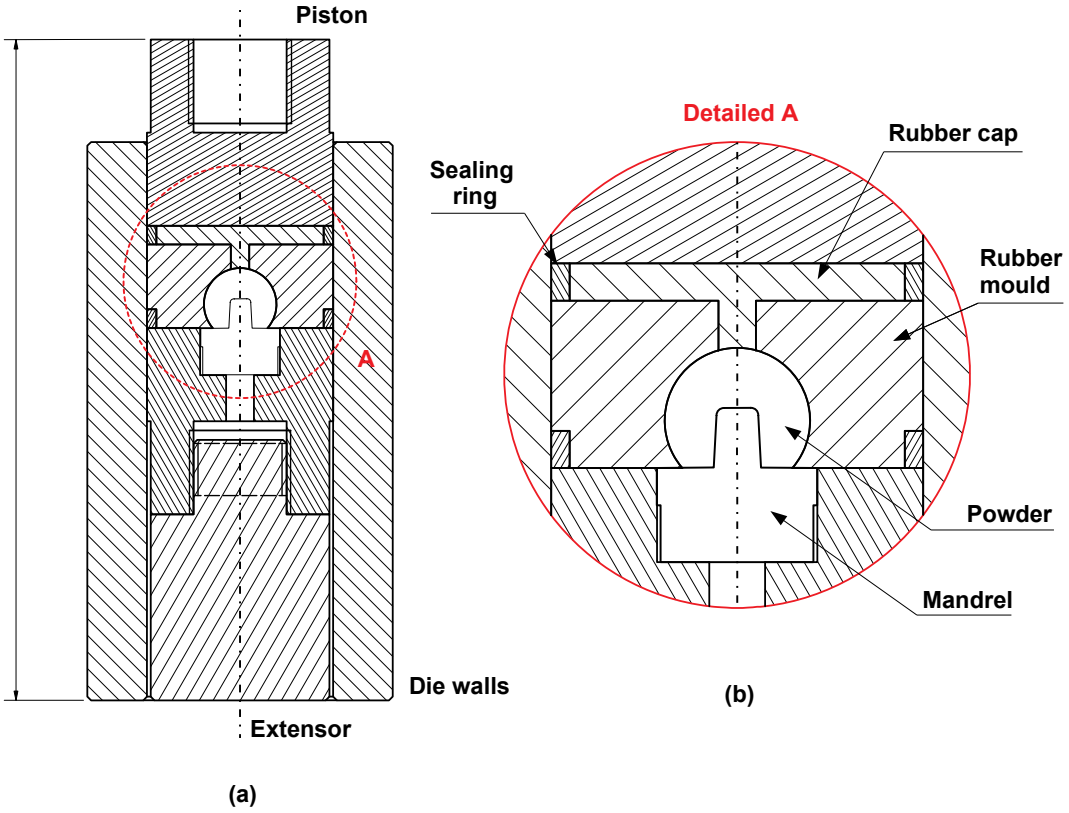

Figure 3.13 (a) Description of the tools used in Rubber Multiaxial Pressing and (b) detailed view of rubber mould.

As Figure 3.13 shows only a first concept of the RMP tools, FE analyses were carried out to improve the design of these parts. The FE analyses were used to predict the final shape of the green ceramic sphere, to obtain an adequate rubber mold design and to identify regions with poorer mechanical properties from the analysis of the density field. The rubber material was described by the Ogden hyperelastic model (Section 2.5). The DPC model was used to account for the mechanical behavior of the alumina powder during pressing. Geometry, mesh,

boundary conditions and rigid analytical surfaces of the FE model are shown in Figure 3.14. A force of 600 kN($\approx$ 75 MPa of axial stress on the piston) was applied at the reference point on the rigid analytical surface representing the piston.

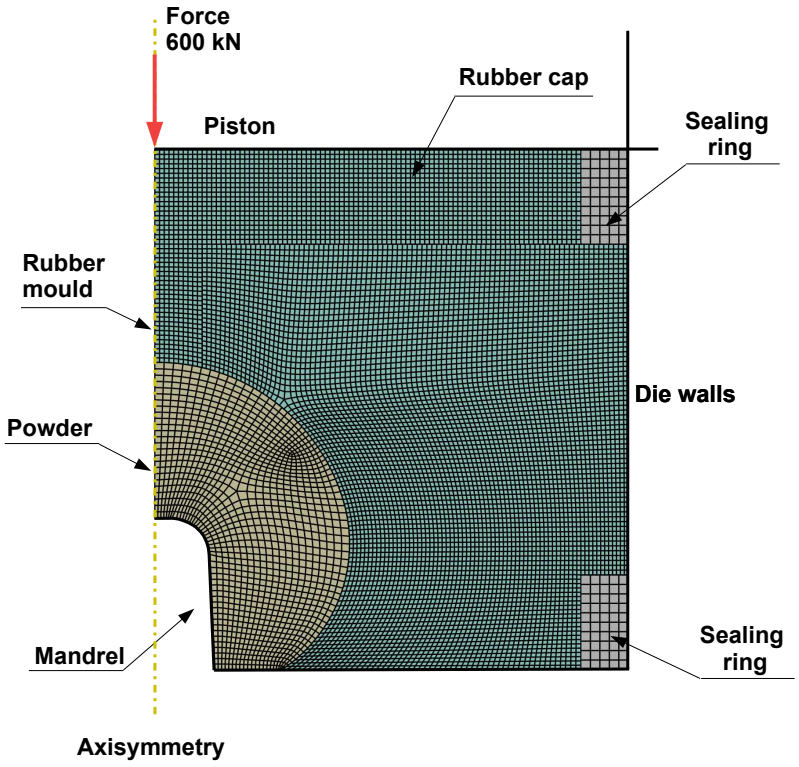

Figure 3.14 Finite Element model for RMP

RMP pressing of the ceramic femoral head was performed experimentally in a uniaxial press, with a maximum recommended capacity of 600 kN. The rubber molds were made using 3D-printed auxiliary parts and following the steps described in Section 3.4. The geometry of the compacted part was compared with the shape obtained in FE analyses, using an in-house developed profile projector.

4 RESULTS

> “I have been impressed with the urgency of doing. Knowing is not enough, we must apply. Being willing is not enough, we must do."
>
> — Leonardo da Vinci

The results of the preliminary identification/validation procedure for the DPC model are described in Section 4.1. To improve DPC model precision, uniaxial and diametral compression tests were performed and their results are described in Sections 4.2, 4.3 and 4.4. The calibrated constitutive model for RenCast® 4644-1 rubber is described in Section 4.6. With the constitutive models for rubber and ceramic powder pressing, a design of RMP for a ceramic femoral head was created using FE analyses and implemented experimentally. Thus, the whole methodology was evaluated by comparing the experimental and simulated results of the femoral head shape (Section 4.7).

4.1 Preliminary identification/validation procedure results for powder compaction model

This section describes the results of an experimental procedure to validate numerical models used to simulate powder pressing. It consists mainly of two steps: closed die uniaxial pressing followed by isostatic pressing. Uniaxial pressing causes a non-homogeneous density distribution in the pressing direction as a consequence of friction between die walls and powder. In isostatic pressing, less compacted regions have a larger volumetric strain, resulting in a non-trivial shape of the re-compacted part, which stems indirectly from the previous density distribution. Experimental data for both steps are compared to the results from finite element models. The Drucker-Prager/Cap constitutive model was used to describe compaction of alumina powder. Several simulations covering a range of parameters obtained from the literature were performed to calibrate the model

through an inverse analysis.

4.1.1 Experimental procedure

The first step of the procedure is confined uniaxial pressing. Figure 4.1 shows the load-displacement curves obtained from the testing machine and with a correction for the machine compliance. The machine compliance was characterized by performing an experiment with no powder in the die cavity. At minimum force (-150 kN), the compliance correction of the piston displacement was 2.1 mm (2.6 % of the total displacement). This correction was required for accurately modeling the experimental procedure.

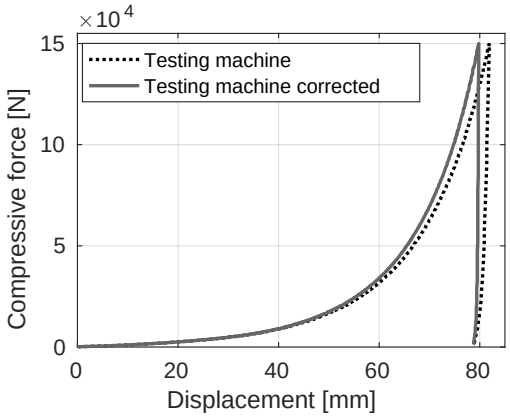

Figure 4.1 Load-displacement curve: raw data and with compliance correction

The results of normal stress in the upper and lower pistons show the effect of friction between the alumina powder and the die wall. The maximum absolute normal stress measured at the lower piston pressure sensor is about 20 % of the maximum absolute normal stress measured at the upper piston, as seen in the stress-displacement curve shown in Figure 4.2.

The second step of the experiment is isostatic pressing of the green compact extracted from the closed die at two different pressures (25 and 200 MPa) and the measurement of the profile of the compacted part for each pressure (Figure 4.3).

The top region of the compacted part (which was subjected to a higher pressure in the first step and, consequently, was denser) had lower plastic strain than the bottom side. At 25 MPa pressure, the top region of the compacted part had

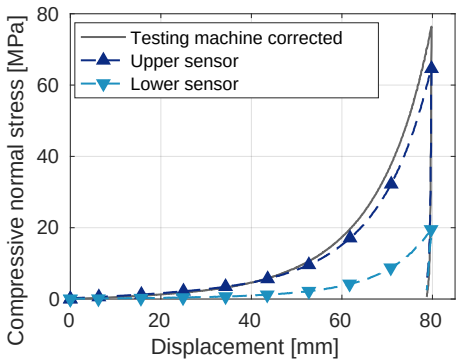

Figure 4.2 Normal stress on lower and upper pistons measured by pressure sensors, and normal stress computed from machine force and the cross-section area of the piston.

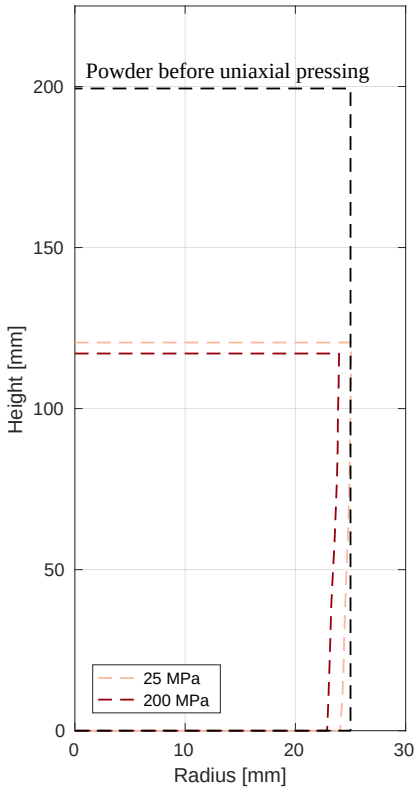

Figure 4.3 Profiles of the compacted part after isostatic pressing of 25 and 200 MPa

no measurable radial re-compaction. Unlike the bottom region of the compact, the top region did not seem to reach the cap yield surface (p_b) at this pressure level. Isostatic re-compaction of the green part from a closed-die pressing proved to be an indirect measure of the porosity left by the earlier steps.

4.1.2 Parameter calibration with pressure sensor data

The minimization of Equation (3.1), used to calibrate the DPC parameters, was accomplished by searching in the intervals defined in Table 3.2 using an in-house algorithm to automatize the finite element analysis. The best fit of DPC parameters and coefficient of friction are summarized in Table 4.1.

Table 4.1 Calibrated parameters

Coefficient of friction	Drucker-Prager/Cap			
μ	d [MPa]	β	R	α
0.3	3.25	55°	0.75	0

A comparison of experimental and FE normal stresses at regions close to the pressure sensors is provided in stress-displacement curves of Figure 4.4 for the best set of parameters. For this set of parameters, the calibration error, Equation (3.1), was computed as 7.3 % for normal stresses measured on the upper piston region and 1.2 % on the lower piston region. At the onset of the stress-displacement curve, the normal stress in the FE model is higher than the experimental one. A reason for this difference is the assumption that the elasto-plastic parameters of the DPC constitutive model (*e.g.,* Young's modulus, material cohesion, initial cap position, etc.) are constant throughout pressing and do not evolve as a function of relative density, as some authors suggest [78–82]. This model shortcoming is not observed in more sophisticated models [13]. The normal stress difference between the regions of lower and upper piston pressure sensors, caused by friction between the die walls and the powder, was well predicted by the FE model. The residual normal stress (after axial unloading) in the pressure sensors showed a difference between the experimental and numerical results (end of the unloading path, Figure 4.4), which may be related to the adopted friction model (Coulomb). An alternative to this friction model, discussed by Gethin et al. [83], is a model with a coefficient of friction dependent on the contact pressure.

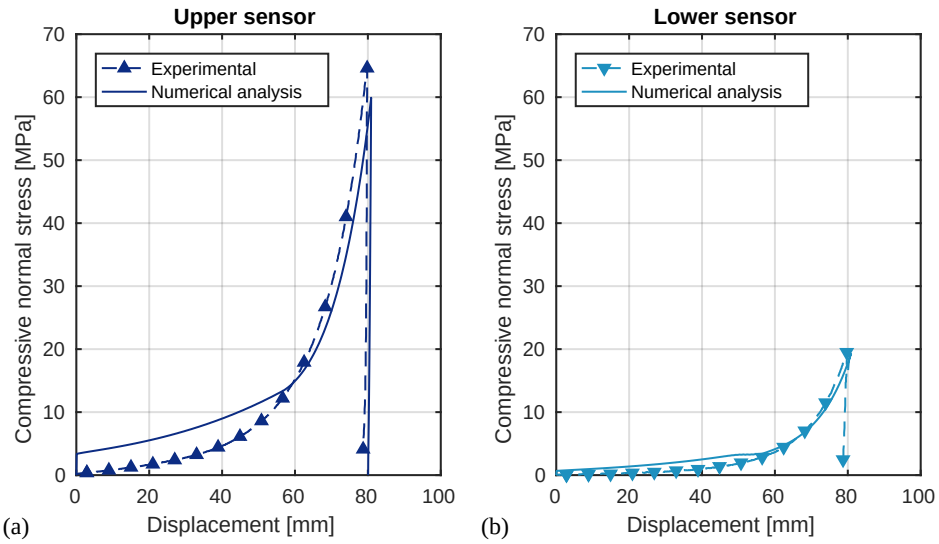

Figure 4.4 Comparison of normal stress measured by pressure sensors and predicted by the FE analysis for lower and upper pistons

4.1.3 Calibration of the cap hardening law

The hardening curve, measured as described in Section 3.3.1, was fitted with an exponential equation

$$p_b = 0.03312\, exp(-13.55\, \varepsilon^p_{vol}) + 2.250 \tag{4.1}$$

where p_b is the yield pressure and ε^p_{vol} the volumetric plastic strain. The R^2 coefficient was 0.9995 between the experimental data and the fitted curve. This hardening law is similar to some empirical expressions found in the literature [78, 84].

4.1.4 Comparison between experimental and numerical results

The shapes of the green compact measured experimentally and predicted by FE modeling after isostatic pressing are shown in Figure 4.5. The difference between experimental and predicted height of the compacted part isostatically pressed was 1.23 mm (1.0 % of the experimental height) and 2.99 mm (2.6 % of the experimental height) at 200 MPa. The maximum diameter measured and predicted in the compacted part had a difference of 0.05 mm (0.2 % of the experimental diameter) when pressed at 25 MPa and 0.40 mm (1.7 % of the experimental di-

ameter) at 200 MPa. The minimum experimental and numerical diameter in the compacted part had a difference of 0.41 mm (1.7 % of the experimental diameter) when pressed at 25 MPa and 0.28 mm (0.3 % of the experimental diameter) at 200 MPa. The measured and FE shape results for the green compact are therefore in very good agreement.

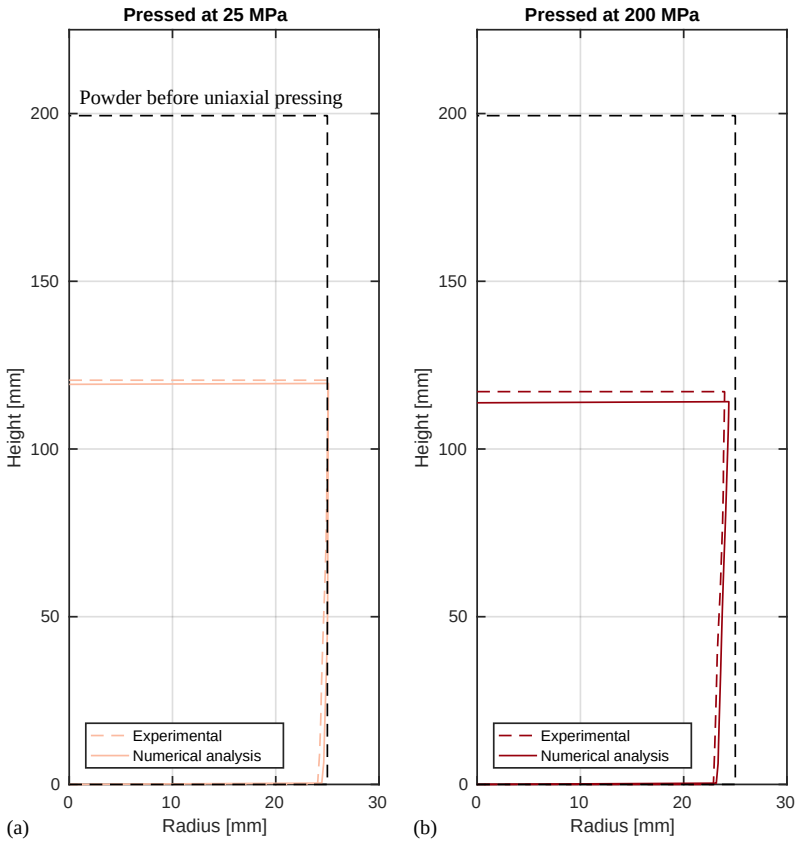

Figure 4.5 Experimental and numerical profiles of the compacted part after isostatic pressing

The density evolution during the numerical simulation of the experimental procedure is shown in Figure 4.6, which presents the density distribution in the green compact after closed-die pressing and ejection (Figure 4.6a), after isostatic pressing at 25 MPa (Figure 4.6b) and 200 MPa (Figure 4.6c). It is noticeable that the friction between alumina powder and die walls leads to a relevant density gradient in closed-die pressing. After first isostatic pressing at 25 MPa, the density field was partially homogenized in the inferior portion of the compact, once the applied

pressure was not enough to compact all regions of the specimen. The second isostatic pressing at 200 MPa was sufficient to result in a homogeneous green compact, in terms of density, but with a non-trivial shape, since less compacted regions exhibited larger inelastic volumetric deformation.

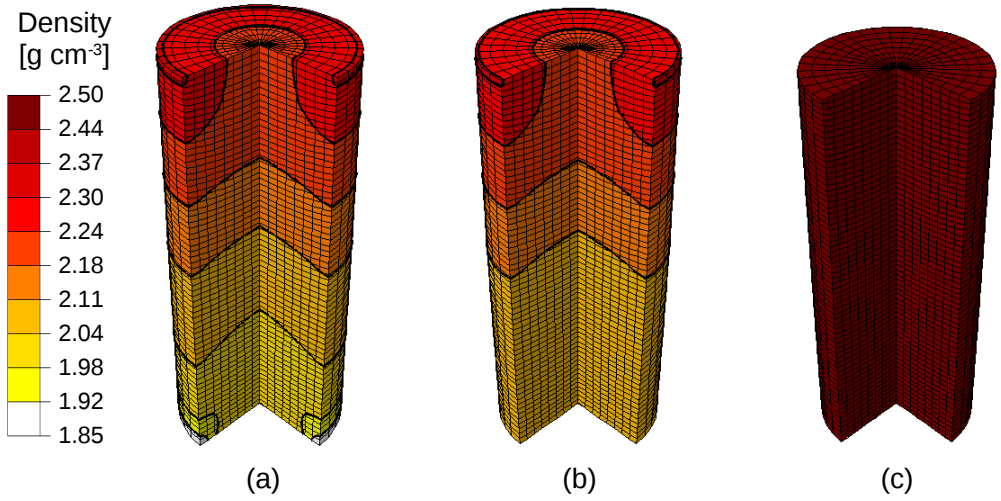

Figure 4.6 Density field after: (a) closed-die pressing and ejection, (b) isostatic pressing at 25 MPa and (c) 200 MPa

In addition, the density distribution presented in Figure 4.6(a) was compared to the reported results of Stupkiewicz et al. [13], who performed experimental and a numerical approach of a single action uniaxial pressing of alumina powder. Their numerical results indicate a range of density varying from 1.8 to 2.1 $\mathrm{g\,cm^{-3}}$ for a green compacted cylinder with 1.9 height-to-diameter ratio, pressed at 40 MPa. Their density values are compatible with the results of this study, varying from 1.85 to 2.4 $\mathrm{g\,cm^{-3}}$ for a green compacted cylinder with 2.4 height-to-diameter ratio, pressed at 76 MPa.

4.2 Uniaxial compression test with bending consideration

A uniaxial compression test was performed on a green-compacted specimen, made of the studied alumina powder (Section 3.1). Using DIC, displacement fields of two perpendicular surfaces of the specimen were measured showing unavoidable bending effect (Section 4.2.1). A constitutive model was calibrated through three Finite Element Model Updating approaches. First, an analysis was performed using average axial strains assessed via DIC and resultant forces to identify the constitutive model (Section 4.2.2). Then, a plane stress analysis was conducted out using the displacements of the boundaries of the regions of interest for each camera separately to obtain the sought parameters (Section 4.2.3). Last, a 3D analysis was carried out using the multi-point constraint method to link displacement fields of both surfaces (Section 4.2.4).

4.2.1 Digital image correlation and multi-point constraint

The images were processed using the Correli 3.0 framework [85] in which the additional steps described in Section 3.3.2 were added (More detailed information about the DIC analysis parameters may be found in Melo et al. [63]). The displacement fields for both surfaces of the specimen under a compressive axial force of 620 N (first peak force ①, see Figure 3.8 at time ≈ 50 s, image 8) are shown in Figure 4.7. The physical size of one pixel was 42.7 µm for face $y-z$ and 45.9 µm for face $x-y$. DIC is a full-field technique that also allows checking the "quality" of the test (*i.e.,* how close it is to a priori assumed boundary conditions). In uniaxial compression, for example, the vertical displacement contours should be horizontal to comply with the hypotheses that the strain and stress fields should be homogeneous before cracks initiate. Figure 4.7 shows that the vertical displacement fields are not satisfying this condition. The inclined contours evidence the presence of bending of the sample during the test. Bending may has some origins already described in Section 3.3.2. A nonuniform stress distribution is a consequence of bending, which may make the classical approach inaccurate to treat the results.

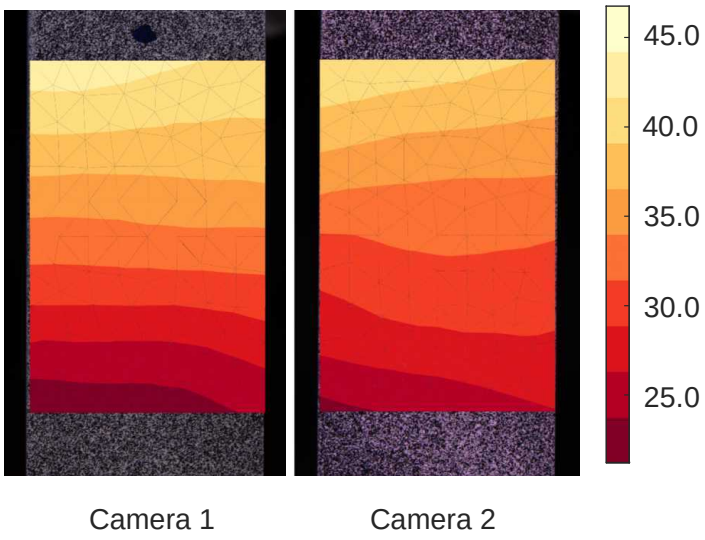

Figure 4.7 Vertical displacement fields (positive downward, expressed in µm) using independent DIC analyses for faces $y-z$ and $x-y$

In spite of the displacement fields measured from faces $y-z$ and $x-y$, (Figure 4.7) showing the same tendency, the displacement levels on the common edge of the sample (right edge $y-z$ and left edge $x-y$) are slightly different. By using the approach described in Section 3.3.2, the displacement field can be measured by prescribing the equality of the vertical displacements of both faces of the shared edge (MPC technique). Figure 4.8 shows the DIC results using this approach. A continuous vertical displacement field is observed for both faces, which means the technique successfully coupled the vertical degrees of freedom of the common edge in the two images. However, a numerical artifact emerges in this region, which is evidenced by the appearance of fluctuations in the form of "waves" in the displacement field. This artifact is a consequence of a vertical misplacement of the mesh boundaries, which were initially positioned by visual inspection.

To solve this problem, the optimization of the mesh boundary positions was performed by varying the vertical position of one mesh with respect to the other one. The result of the minimization of Equation (3.20) showed that the meshes had to be shifted by a relative vertical displacement of 1.48 mm (*i.e.,* $\approx$ 64 pixels). The visual positioning of mesh boundaries was estimated to be in the yellow box

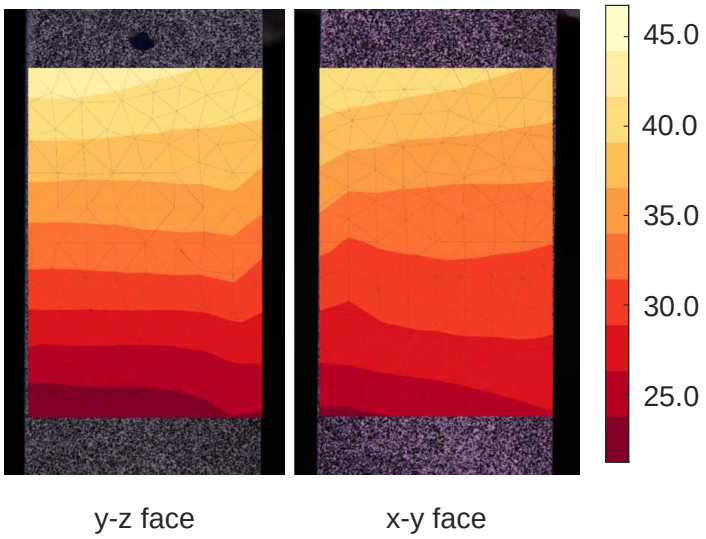

Figure 4.8 Vertical displacement fields of faces $y-z$ and $x-y$ (positive downward, expressed in µm) when the constraints of equal vertical displacements is prescribed on the common edge

of Figure 4.9a, and its optimization is depicted in white. Figure 4.9b shows the "shear" cost function (Equation 3.20) as a function of vertical mesh boundary translation about the optimal position. A smooth parabolic shape is observed and its minimum is close to unity, which means that the shear strain uncertainty γ_s is reached.

Figure 4.10 shows the displacement field with the corrected mesh position. The numerical artifact is less pronounced and the displacement field is smoother than in the previous case.

This methodology made possible an analysis of both images in a more consistent way, allowing the use of the displacement fields for FEMU optimization with considerations of three dimensions. The corrected mesh was used in all identification approaches. The correction is the most influential in the three-dimensional coupled analysis.

4.2.2 Classical FEMU-F analysis

By the use of a FEMU-F approach described in Section 3.3.2, the Young's modulus E, yield stress σ_y, hardening coefficient b, and compressive strength σ_∞ were

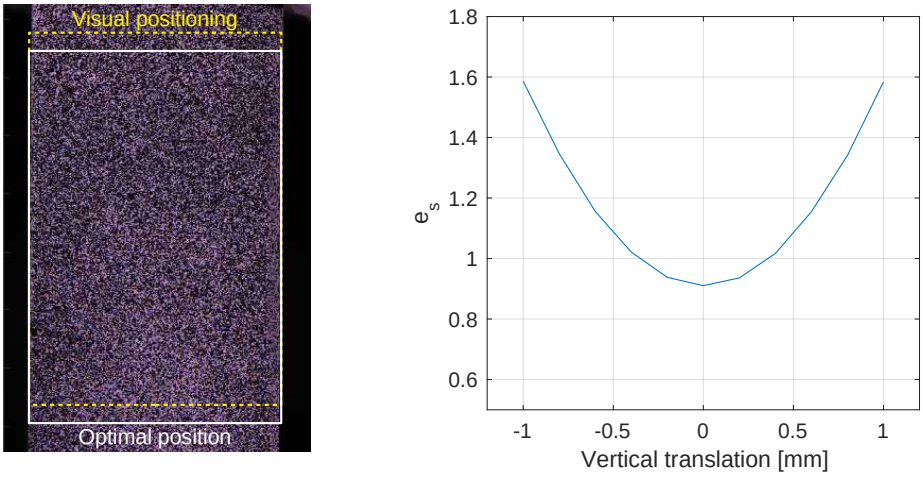

(a) (b)

Figure 4.9 (a) Initial visual positioning of mesh boundaries (yellow) and after optimization (white). (b) Cost function e_s vs. vertical translation of mesh on $x-y$ face

identified using the region of interest of DIC as a virtual gauge for the sequence of images of $y-z$ and $x-y$ faces independently. A sensitivity analysis was performed for all images of the test. The load sensitivities were computed by using Equation 4.2[1]. The derivative was estimated by the use of forward differences with a perturbation factor $\alpha = 10^{-2}$ of each parameter ($\Delta p_i = \alpha p_i$)

$$S_{Fi}(p_i,t) = \frac{\partial F_c}{\partial p_i}(p_i,t) \approx \frac{F_c(p_i+\Delta p_i,t) - F_c(p_i,t)}{\Delta p_i} \tag{4.2}$$

Figure 4.11 shows the computed load sensitivities $\mathbf{S}_F$ for the $y-z$ face (the values for the $x-y$ face are very similar), indicating the time dependence of each parameter and the influence of each variable on the different steps of the test. The elastic modulus increases its sensitivity as a function of the elastic energy at a higher rate in the elastic regions and a slower rate in the elastoplastic regime, following the loading curve shown in Figure 3.8. All the parameters related to the plasticity model show no sensitivity in elasticity (as expected). The yield stress σ_y has a fast increase in sensitivity in the transition from elastic to plastic regimes, and then a slow decrease until the peak stress. The hardening coefficient b and

[1]Note that the variables described in Equation (4.2) are the same as those used in Equation (3.21).

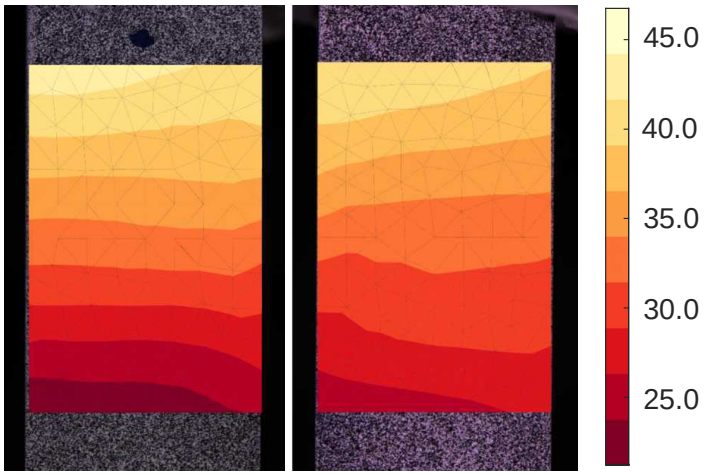

Figure 4.10 Vertical displacement fields for faces $y-z$ and $x-y$ (positive downward, expressed in µm) when the constraints of equal vertical displacements is prescribed on the common edge and the meshes were repositioned

compressive strength σ_∞ become more important at the end of the test, where their sensitivities are higher. For all parameters, the load sensitivities are very high (in comparison with the load uncertainty of 4.5 N or the corresponding stress uncertainty of 11 kPa) for a one percent variation of each parameter. This result indicates that the parameters are expected to be identifiable for the considered test and proposed identification route.

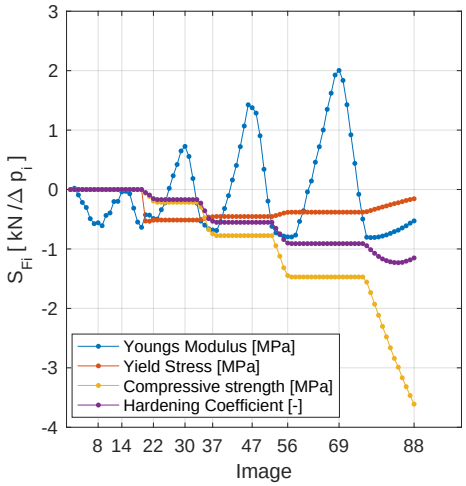

Figure 4.11 Computed load sensitivity for $x-y$ face

Figure 4.12a shows the Hessian matrix in decimal logarithm (see Equation 3.25).

The sensitivity of each parameter taken independently is related to the diagonal terms of the matrix. The off-diagonal terms represent the correlations between two parameters. The spectrum of eigen values (Figure 4.12b) is not very wide, which indicates that the overall conditioning of the Hessian is very good, namely, all parameters should be identifiable. The most sensitive parameters are the hardening and Young's moduli (*i.e.,* the third and fourth eigen vectors are mostly dependent on these two parameters), followed by the yield stress and then the ultimate strength.

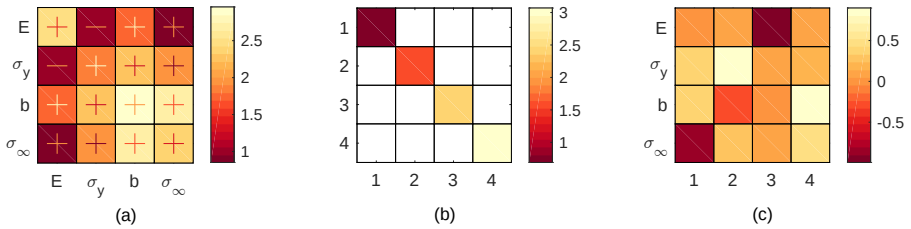

Figure 4.12 Hessian matrix in decimal logarithm for $x-y$ face, (b) Decimal logarithm of the eigenvalues of Hessian matrix, and (c) corresponding eigenvectors.

Figure 4.13 shows the stress-strain responses for axial strains obtained from independent DIC analyses. From the full-field measurements, the axial strains were evaluated averaging the engineering strain measure of DIC mesh elements (Figure 3.10). The numerical results were derived from a one-element FE model, where displacements were prescribed to represent the strain obtained from the DIC technique in the previous step. The difference between experimental curves of $y-z$ and $x-y$ faces (Figure 4.13) are due to bending of the specimen, which should be better captured using the three-dimensional model of Section 4.2.4.

The difference between computed and measured loads, namely load residuals, are reported in Figure 4.14. Their levels are similar for both faces, which is shown by the calculation of the root mean square (RMS) differences, namely 223 N (or 0.54 MPa) for the $x-y$ face, and 173 N (or 0.42 MPa) for the $y-z$ face. After the first two cycles, the residuals increase significantly, in other words, mostly in the plastic regime (Figure 4.14a and b). The nonlinear behavior of the compact

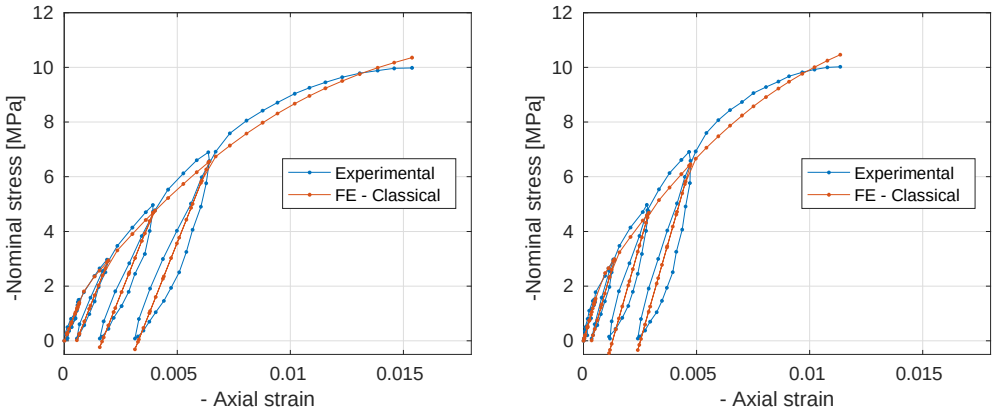

Figure 4.13 Classical (independent) analyses using DIC as a virtual strain gauge. Experimental and numerical stress-strain curves for (a) $y-z$ face, and (b) $x-y$ face

is due to its porous nature. The dilatancy of the medium increases the porosity, resulting in an even higher nonlinear behavior, as a consequence of the presence of microcracks and the effect of friction between crack surfaces [43]. One may note that the first two cycles of loading and unloading have a better agreement between computed and measured forces, thereby highlighting that the selected elastic model cannot fully capture the unloading and reloading sequences of the last three cycles. Damage may explain such differences. The equivalent error (in RMS sense) for both faces is equal to 200 N, much higher than the load uncertainty, which evidences that this error has its source in the numerical and material models chosen herein.

The values of the calibrated parameters are gathered in Table 4.2. The differences in levels for each face are mostly related to the assumption of homogeneous stress states in the specimen, which is not a good representation for this test.

4.2.3 Plane stress FEMU-F analysis

By using boundary conditions measured via DIC, a plane stress analysis was performed for both faces independently. In this analysis, a non-homogeneous stress state can be achieved and bending effects partly taken into account. The same

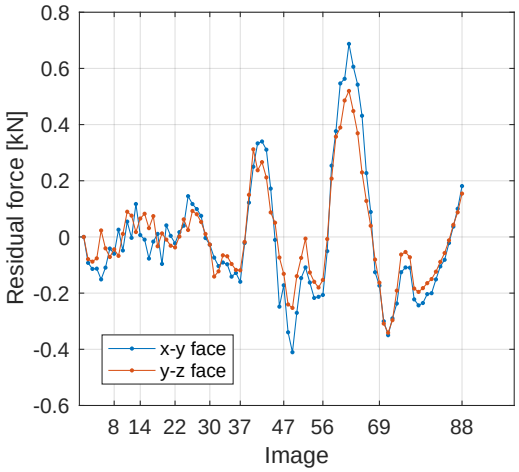

Figure 4.14 Load residuals for (a) $x-y$ and (b) $y-z$ faces

Table 4.2 Calibrated parameters for classical FEMU-F analysis

Parameters	$x-y$ face	$y-z$ face	Average
E [GPa]	2.9	2.1	2.5
σ_y [MPa]	2.3	2.0	2.1
σ_∞ [MPa]	12.4	11.6	12.0
b [-]	212	199	206

constitutive parameters as in the previous analysis were inspected. A sensitivity analysis was also performed for all images of the test and the results were similar as before. For the sake of brevity, the corresponding results for the plane stress analyses are not repeated herein. In Figure 4.15, experimental and numerical forces are compared for $y-z$ and $x-y$ faces. A good agreement is observed.

The difference between computed and measured forces are also very similar for both faces. The root mean square values for the residual forces were evaluated as 221 N for $x-y$ face and 175 N for $y-z$ face. An increasing difference between numerical and experimental results can be also seen in Figure 4.16. The linear elastic model was not a good description of the mechanical behavior of the green compact, mainly after the first two cycles in the plastic regime. In the present case, the equivalent RMS error is 199 N, a value very close to that obtained in the previous analysis, which means that there was no significant improvement in the representation of the problem by the numerical model.

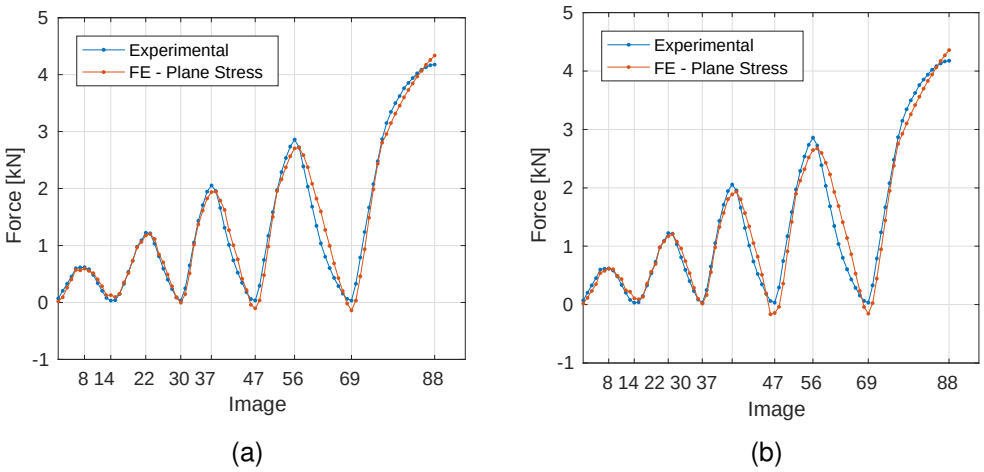

Figure 4.15 Plane stress analyses using measured boundary conditions. Experimental and computed forces for (a) $y-z$ and (b) $x-y$ faces

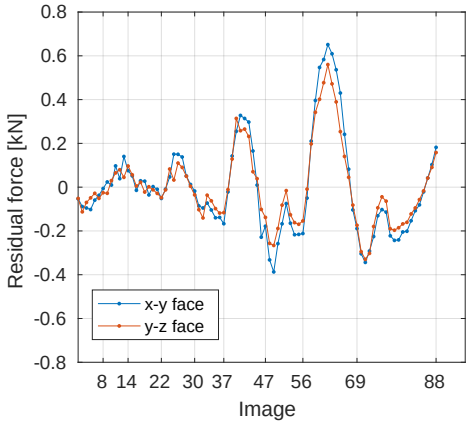

Figure 4.16 Force residuals for the plane stress analyses

Table 4.3 shows the two sets of parameters obtained for $y-z$ and $x-y$ faces. The gap between numerical and experimental data was minimized iteratively by the FEMU method (Figure 4.15). However, there is a lack of agreement between the calibrated parameters for the two analyses, showing that the plane stress assumption was not sufficient to treat this problem. In the present case, bending has a three-dimensional nature, making inaccurate the previous assumption. Most of calibrated parameters were slightly closer to each other in comparison with the classical approach (Table 4.2), which may be related to the consideration of the bending effect in each face separately thanks to the plane stress analysis.

Table 4.3 Calibrated parameters for plane stress FEMU-F analyses

Parameters	$x-y$ face	$y-z$ face	Average
E [GPa]	2.9	2.2	2.6
σ_y [MPa]	2.2	2.0	2.1
σ_∞ [MPa]	12.8	11.9	12.3
b [-]	209	197	203

4.2.4 3D Coupled FEMU-F analysis

The 3D FEMU-F analysis used the data obtained from DIC using a multi-point constraint approach to couple the vertical DOFs on the shared edge of the specimen. On the top and bottom boundaries, the DIC data were extrapolated to planes as described in Section 4.2.1. Sensitivities and the Hessian matrix are again very similar to those shown in Section 4.2.2, and for the sake of brevity, they are not shown hereafter. The experimental and computed forces are reported in Figure 4.17a, and the corresponding residual forces in Figure 4.17b. The residual forces are similar for 3D and plane stress analyses, the root mean square of the residual force for the present case is 191 N, which is lower than the values of the previous two analyses, thereby showing that the 3D consideration of the bending effect is an improvement in the numerical representation of the mechanical test.

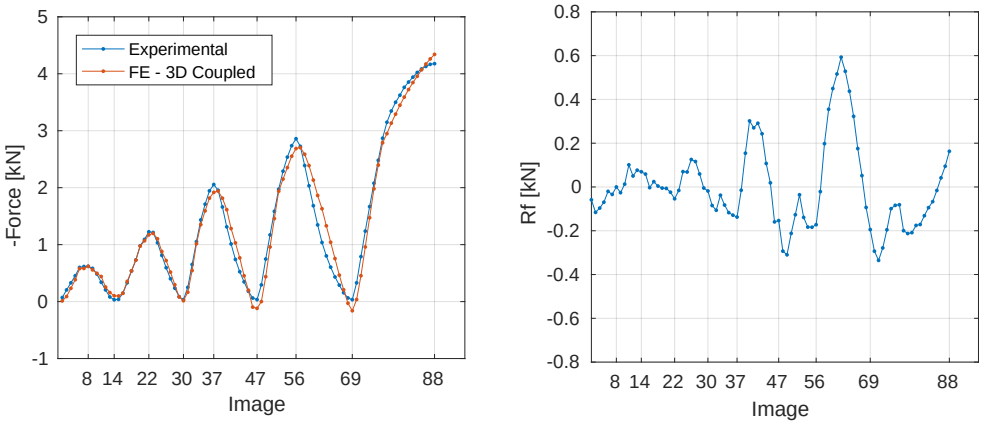

(a) (b)

Figure 4.17 (a) Experimental and computed forces, and (b) corresponding residuals for the 3D Coupled FEMU-F analysis

The minimization of the gap between computed and experimental data by the 3D Coupled FEMU-F algorithm resulted in yet another set of parameters in comparison with the previous analyses (Table 4.4). It is interesting to note that their levels lie between those previously found and close, but not identical, to their averages.

Table 4.4 Calibrated parameters for 3D FEMU-F analysis

Parameters	3D FEMU
E [GPa]	2.5
σ_y [MPa]	2.0
σ_∞ [MPa]	12.4
b [-]	207

From the load distribution obtained in the FE model, it was possible to calculate the load eccentricity *i.e.,* the point where the resultant moment vanishes) in directions x and z (Figure 4.18). Small eccentricities are observed in both directions. However, neglecting them may lead to erroneous calibration of material parameters. For example, considering the parameters in the classical FEMU-F approach for the $x-y$ face, the Young's modulus is 15.4% higher in comparison with that obtained in this last analysis. It is important to note that care was taken to minimize the bending effect during the test, by the use of epoxy resin in the end portion of the specimen and checking the parallelism in the platens of the testing machine (see Figure 3.7). Yet, even with such procedures, it was not possible to fully align the sample. Further, it is interesting to note that beyond the second cycle, the eccentricity does not evolve much. This phenomenon is related to the fact that the material is yielding and that this nonlinearity induces stress (and strain) redistributions that were not possible in the elastic regime.

Figure 4.19 shows the FE results of the axial strain distribution in the ROI of the specimen for the last image (*i.e.,* at maximum loading). Non-homogeneous strains are observed in the specimen. Moreover, the average value of axial strain is close to the diagonal of the cross-section that is related to the same magnitude of eccentricity shown in Figure 4.18.

The so-called percent bending [62] is a quantity defined as the difference be-

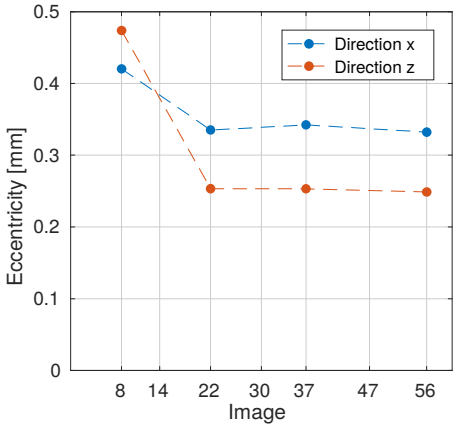

Figure 4.18 Eccentricity of the load distribution at loading peaks, expressed as distance from the center of the cross section

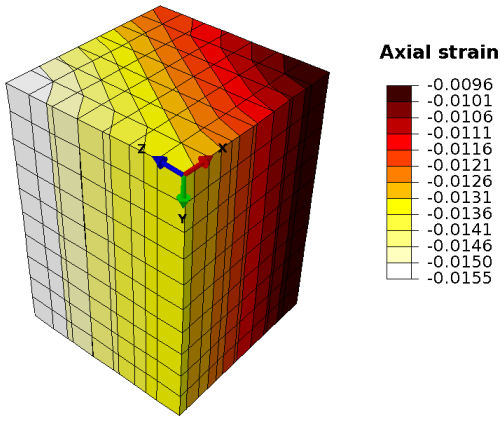

Figure 4.19 Axial strain distribution in the FE model for the last image (88)

tween the strain on the surface and the nominal axial strain divided by the nominal axial strain. It is a measure of the goodness of uniaxial compression tests. Figure 4.20 shows the average and standard deviation of the axial strains as functions of the image number. The two quantities are proportional to each other during the whole test. From such data, it is possible to calculate a maximum percent bending of 23, which is approximately 10 times higher than the recommended level (*i.e.,* 2.5 [62]).

4.3 Multi-test approach for identification of density-dependent parameters

The multi-test approach based on FEMU-DIC analyses, as described in Section 3.3.3, was applied to calibrate the Drucker-Prager parameters as a function

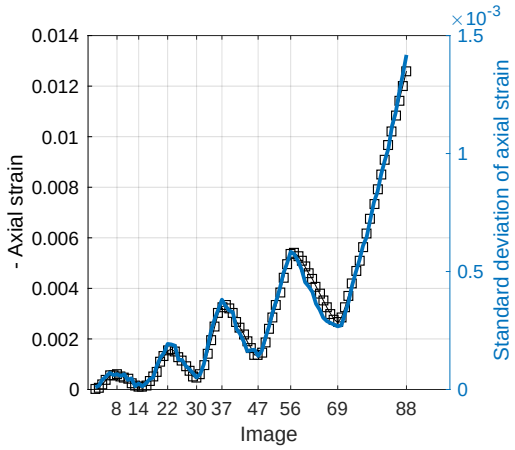

Figure 4.20 Average (square symbols) and standard deviation (solid blue line) of axial strain vs. image number

of density. Figure 4.21 shows the comparison of numerical and experimental force in the analyzed images for the nine performed tests. Note that same density specimens have different loading curves, even though, the numerical model is able to describe satisfactorily all responses, which means that their differences may be explained by bending artifacts (discussed in the previous section) and this feature is captured by the FEMU-DIC approach.

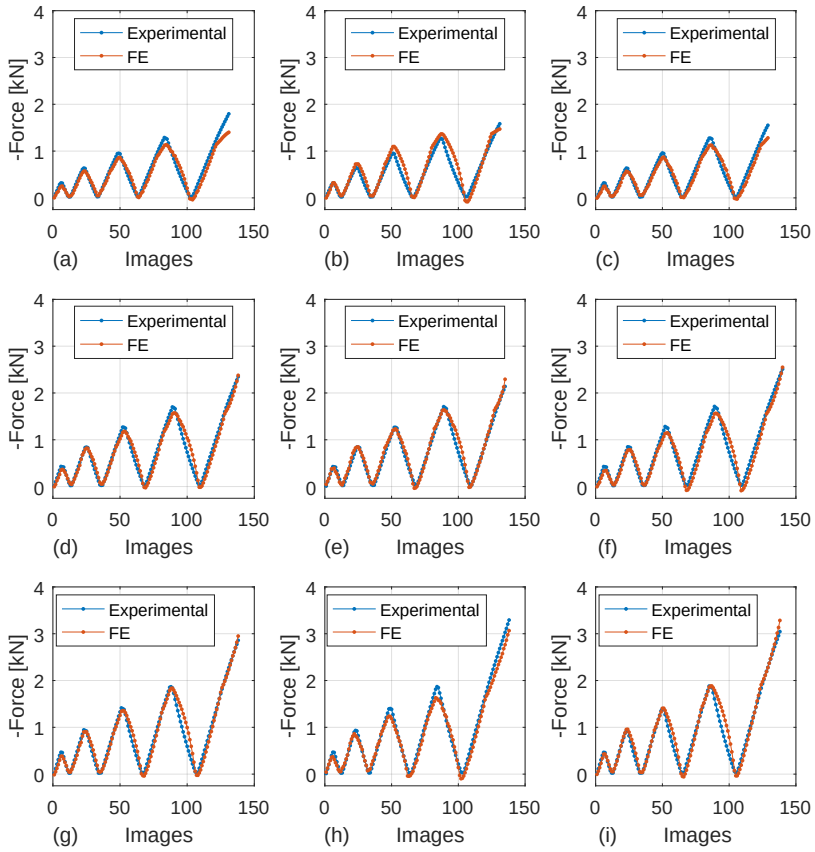

Figure 4.21 Curves of experimental and numerical forces from (a, b and c) uniaxial compression tests 1, 2 and 3 with specimens pressed at 50 MPa, (d , e and f) tests 4, 5 and 6 with specimens pressed at 100 MPa and (g , h and i) tests 7, 8 and 9 with specimens pressed at 200 MPa.

Sensitivities and Hessian matrices were similar to the case of uniaxial compression shown in Section 4.2.2. Figure 4.22(a) shows that the stiffness of the compacted powder is higher in denser specimens, which agrees with other powder studies [78, 81, 86–89]. The same behavior is observed for the yield stress and compressive strength, respectively shown in Figures 4.22(b) and (c). The hardening parameter decreases as a function of density, which is also expected as the specimen becomes more brittle at lower densities.

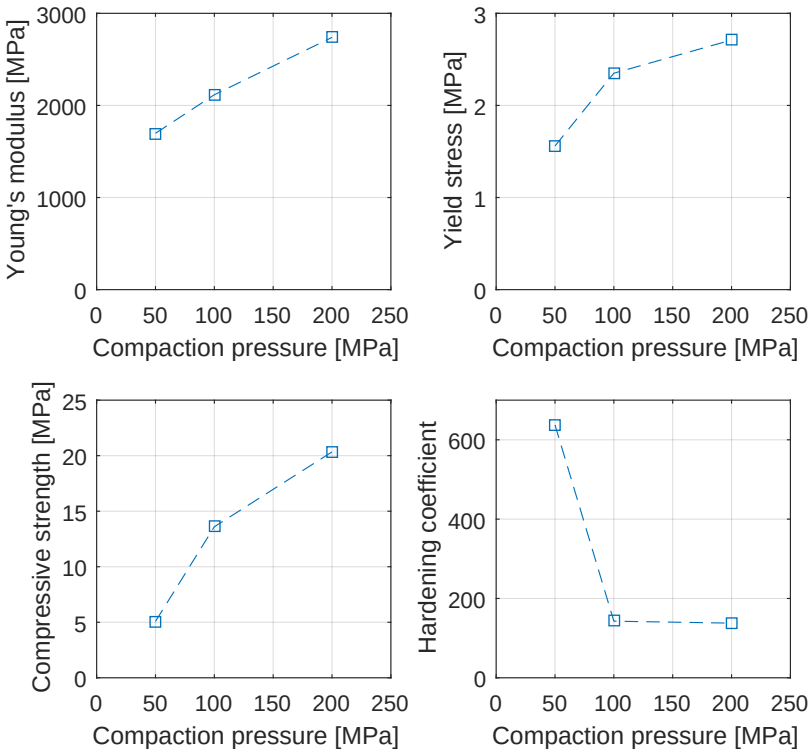

Figure 4.22 Parameters of Drucker-Prager surface evaluated from multi-test approach

The Young's modulus found in the multi-test approach for the specimens pressed at 100 MPa was 18 % lower than that found using a single specimen (Section 4.2). Montilha et al. [43] report a Young's modulus 1.4 % lower for the specimens pressed at 200 MPa. These differences may be related to artifacts of the experimental procedure or deviations in the specimen manufacturing, and highlights the importance of using more than one specimen in the analysis.

4.4 Angle of friction

The results of uniaxial and diametral compression were used to obtain the angle of friction, following the approach described by Montilha [43] to identify dilatancy. Specimens pressed at 100 MPa of diametral and uniaxial compression were used for this evaluation. Figure 4.23(a) and (b) shows the curves of axial and transverse strain vs. Mises stress q, respectively, for the Brazilian test 1. With the DIC results, the onset of dilatancy is observed as a change in the tendency of reduction in volumetric strain ε_{vol}. In other words, dilatancy onset is here defined as the minimum value of ε_{vol} (see Figure 4.23c). Before dilatancy onset, small permanent strains may be observed and are related to pore closure and the rearrangement of granules. These small plastic strains are neglected in this analysis. After the dilatancy point, the volume increase is related to the dilation mechanisms, for instance, the initiation of cracks and voids. Although failure criteria are used to calibrate many constitutive models of powder compaction, this result emphasizes that the dilatancy point occurs earlier than the ultimate load and, thus, should be considered in parameter identification. To estimate the dilatancy point, the volumetric strain estimated for the elements of the DIC mesh were averaged for each time step in opposite faces for Brazilian tests and in adjacent faces for the uniaxial compression tests. For Brazilian tests, only the elements within 20% of the diameter of disc (close to the center) were used to perform the calculation in a region of homogeneous strain.

The dilatancy point of three uniaxial compression tests and three diametral compression tests were identified. At these points, the equivalent Mises stresses and pressure were calculated using the equations described in Section 3.3.4. Figure 4.24 shows a linear regression for these values. The angular coefficient of the curve corresponds to the angle of friction β that describes the Drucker-Prager surface, and its value was found as 63.3°, which is 15% higher than the previously reported in the validation procedure described in Section 3.3.1.

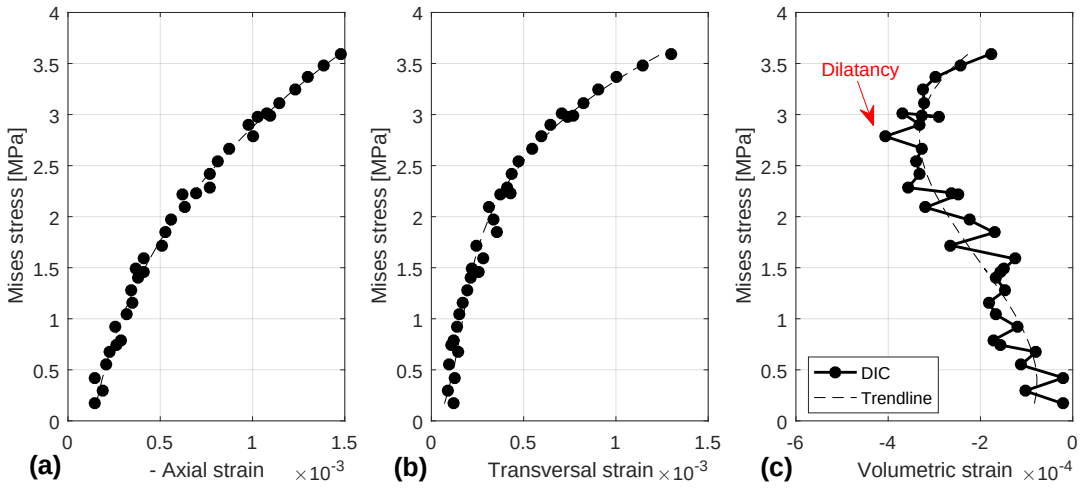

Figure 4.23 (a) Axial, (b) transversal and (c) volumetric strain for the Brazilian test 1.

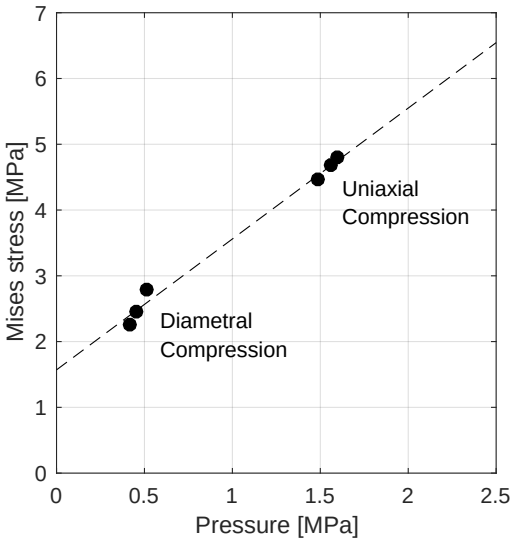

Figure 4.24 Linear regression of the pressure and equivalent Mises stress data identified by the dilatancy approach.

4.5 Density-dependent elastic modulus and material cohesion

The yield stresses found in the multi-test approach were used to evaluate the material cohesion, using Equation (2.10). The dilatancy method could also be used to evaluate the material cohesion. However, it neglects some small plastic strains that occur before the minimum strain point and may lead to less precise results [43]. Figure 4.25 shows the evolution of material cohesion as function of the compaction pressure calculated using the data from multi-test approach and

the angle of friction, Equation (2.10).

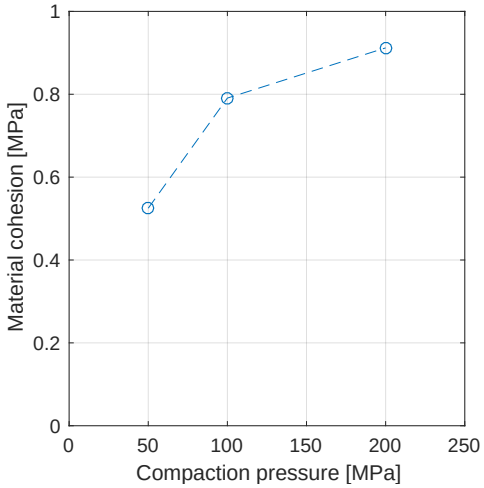

Figure 4.25 Material cohesion as a function of compaction pressure for the studied ceramic powder.

4.6 Constitutive model for RenCast 4644-1 rubber

Using experimental test data, the hyperelastic material curve fitting tool in Abaqus® permits the user to compare different hyperelastic models. The input data in Abaqus® are the nominal stress and nominal strain data pairs. Uniaxial and volumetric compression tests were performed in an Instron® (model 5500R) universal testing machine. Hyperelastic models of Arruda-Boyce, Ogden (order 3), and polynomial (order 2) were used to fit the results from these experiments as shown in Figure 4.26. In Figure 4.26(a and b), the experimental and numerical curves are presented for the tests of uniaxial and volumetric compression, respectively. Table 4.6 shows the RMS values of each curve fitting.

All the tested hyperelastic models were able to fit well the uniaxial compression data. However, the Ogden model was the most suitable choice for predicting the behavior of rubber in the volumetric test, which is proven by the good agreement in the curves of Figure 4.26(b).

Table 4.5 RMS values of the curve fitting

Model	Uniaxial compression [MPa]	Volumetric compression [MPa]
Arruda-Boyce	0.0213	21.5
Ogden	0.0149	1.0
Polynomial	0.0054	1.8

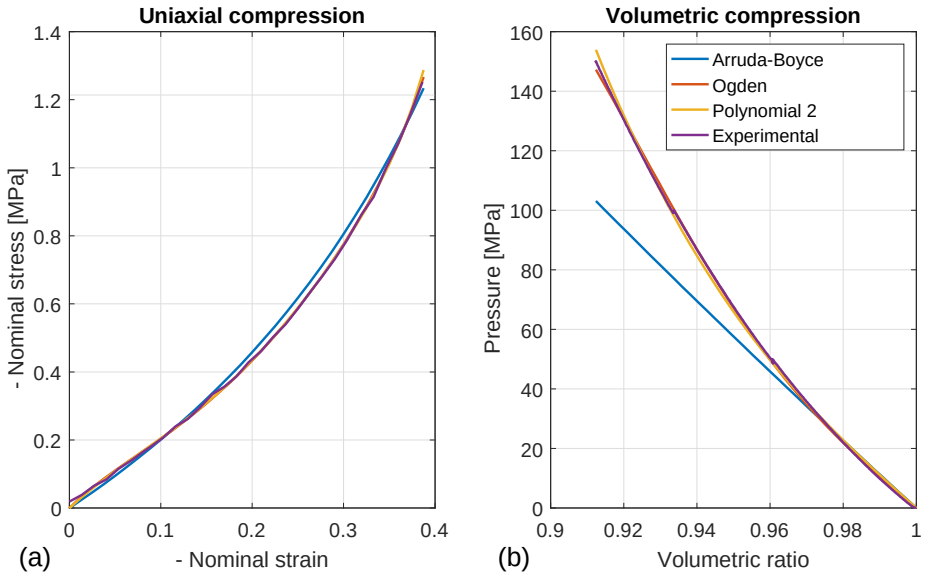

Figure 4.26 Calibration with the tests on the rubber material: (a) Nominal strain-stress curves for uniaxial compression tests and (b) nominal stress as a function of volumetric ratio for the volumetric compression tests.

Table 4.6 Calibrated parameters for the Ogden hyperelastic model (order 3)

i	μ_i [MPa]	α_i	D_i [MPa^{-1}]
1	0.473	-1.285	1.919×10^{-3}
2	0.899	25.000	2.873×10^{-5}
3	-0.457	-12.464	-8.211×10^{-7}

4.7 Design, numerical and experimental simulation of RMP

There are many advantages of RMP as high productivity and homogeneous products. However, the main shortcoming of the process is in the tool design. For example, it is difficult to predict the geometry of the rubber mold in its deformed configuration. The complexity of the deformed geometry is mainly a consequence of the nonlinear mechanical behavior of rubber and powder, as well as the friction conditions between the parts. To overcome this difficulty, firstly, an FE model was implemented using the preliminary parameters (Table 4.1, Page 62) found for the studied alumina powder. The sealing rings were represented by a linear elastic model for aluminum alloy (E = 70 GPa and ν=0.33). The friction coefficients estimated from the literature [9, 56] were 0.2 for a powder/rubber surfaces, 0.3 for powder/steel surfaces, 0.05 for a rubber/steel surfaces and 0.05 for the rubber/steel surfaces, the last surfaces were lubricated with graphite powder.

The geometry was represented in an axisymmetric model and was discretized in the mesh shown in Figure 3.14 (page 57). For rubber, C3AX4HR elements were used (continuous, axisymmetric, four-noded, hybrid formulation and reduced integration). C3AX4 elements (continuous, axisymmetric and four-noded) were attributed to the alumina powder, and C3AXR elements (continuous, axisymmetric, four-noded and reduced integration) were attributed to the rubber cap. The geometry of the rubber mold was altered in an iterative process, so that the final shape of the compact was satisfied. In less than 10 iterations, a suitable rubber mold was obtained for RMP, illustrated in Figure 4.27.

The profile obtained in the FE analyses and the target profile are shown in Figure 4.28. Using numerical simulations, it was possible to adapt the geometry and achieve the target profile for the green compact. It should be noted that the process carried out in numerical analyzes could also be conducted experimentally, by trial-and-error, and this process would probably last days or months. On the other hand, once the appropriate models are known, identified and validated for the simulations, the design of the rubber mold by numerical analyses may take a few hours of work by an engineer with master in these tools. The developed pro-

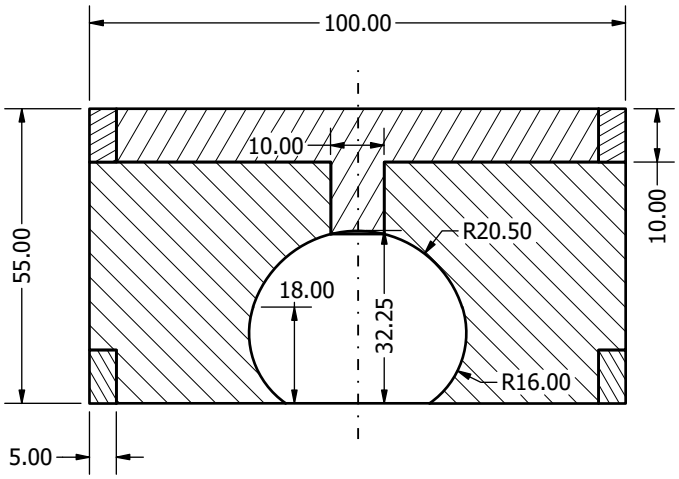

Figure 4.27 Optimized rubber mold geometry for RMP of a ceramic femoral head.

cedure is suitable to design other ceramic parts and an automated optimization algorithm, as the one described in Section 2.6, may be used to reduce the time spent on the iterations.

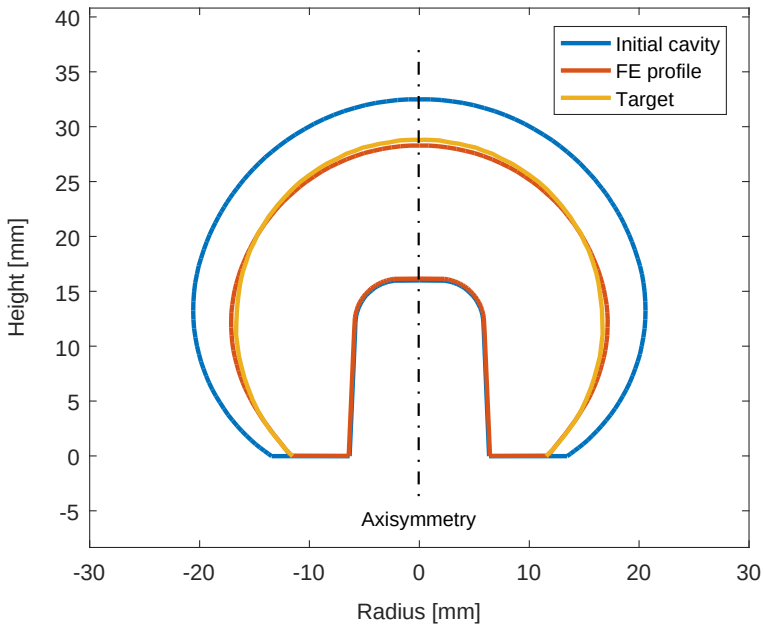

Figure 4.28 Profile of the undeformed cavity of the rubber mold and profiles of the desired compact (target) and the outcome of the finite elements analysis.

The profile achieved in the FE analysis was used to manufacture the rubber

mold with the help of 3D-printed parts, Figure 4.29(a). With the procedure described in Section 3.2, the rubber parts were produced. Figures 4.29(b-c) show different views of the rubber mold and cap, the aluminum sealing rings are also shown at the bottom of the rubber mold and rubber cap.

(a) (b) (c)

Figure 4.29 Rubber parts manufactured for RMP: (a) Auxiliary 3D-printed part, (b) bottom view of the rubber mold, and (c) top view of the rubber mold and cap.

RMP of the ceramic femoral head was performed in a manual uniaxial press, with the tools described in Section 3.5. The rubber mold and cap surface in contact with the steel parts were lubricated with graphite powder. The rubber mold cavity was filled with 34.2 g of alumina powder, resulting in a loose-powder density of 1.1 g.cm^{-3}. The lower loose-powder density in comparison with the previously reported value (Section 3.1) may be a consequence of the geometry of the cavity, which jeopardizes the filling process. Figure 4.30 shows the successfully pressed part, demonstrating that RMP is viable for ceramics.

Figure 4.30 Ceramic femoral head produced via RMP.

To perform a proper comparison of the numerical and experimental profiles, an algorithm was developed in Matlab®. Side and top-view images were taken

from the compacted part (Figure 4.31), using a Canon 5DS camera with 180-mm Canon macro and Canon Extender EF 2x III. The camera was placed at a distance of 3.6 m from the specimen and level measurements were performed to ensure perpendicularity between the camera axis and zenith-axis of the specimen. By the difference of contrast in the images, the algorithm detects the profiles, which are shown in Figures4.31(d-e). Two measurements were taken on the side view, rotating the part around its zenith-axis by 90°. It is worth noting that RMP led to a final part with good axial symmetry, Figure 4.31(d). To verify the profile obtained by the algorithm, a caliper measurement was performed in the larger diameter of the green part, resulting in a value of 16.32 mm (0.5% lower than the average value obtained by the optical profile measurements).

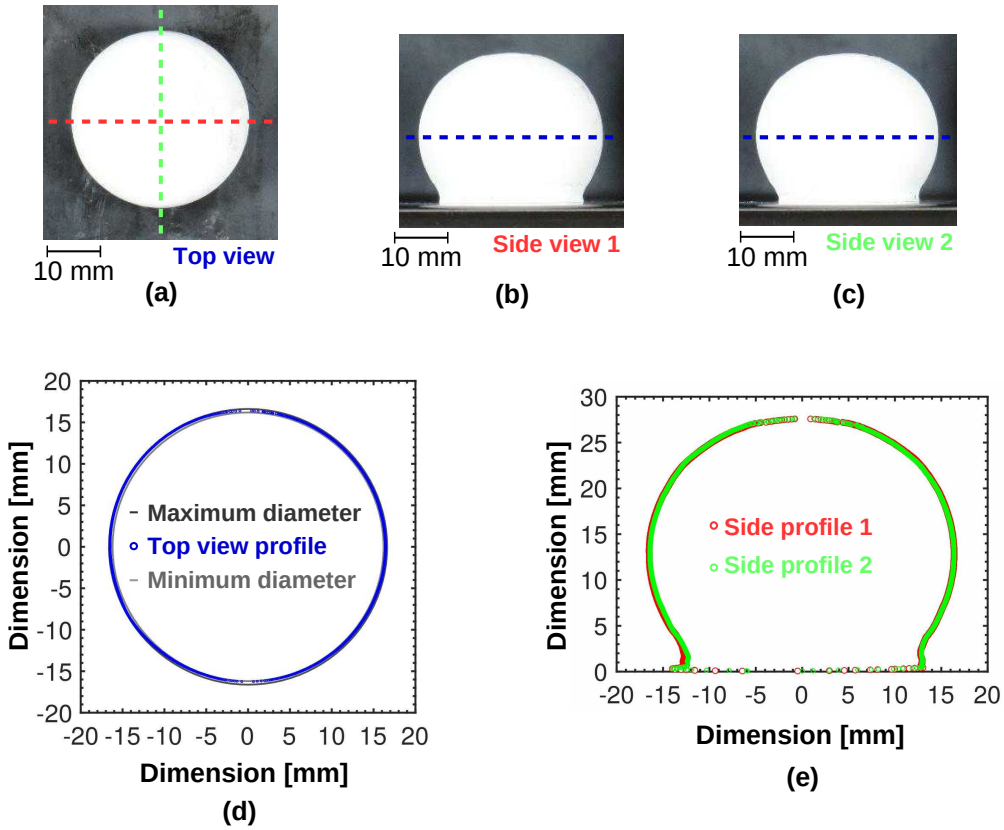

Figure 4.31 Measured profiles of the femoral head pressed by RMP: (a) Top view image, (b) Side view 1, (c) Side view 2, (d) Top view profile and (e) Side view profiles.

Figure 4.32 shows a comparison between numerical and experimental data. For the numerical results, the initial density was updated to the value obtained

in the RMP trial, leading to a smaller final compact in comparison with the target geometry. Normally, the target geometry is defined considering a material to be removed and a small variation in its dimensions may be tolerated. The region near the base of the compact displays a more pronounced discrepancy between the experimental and numerical results. This difference could be attributed to the use of a simple contact model in the numerical simulations [90].

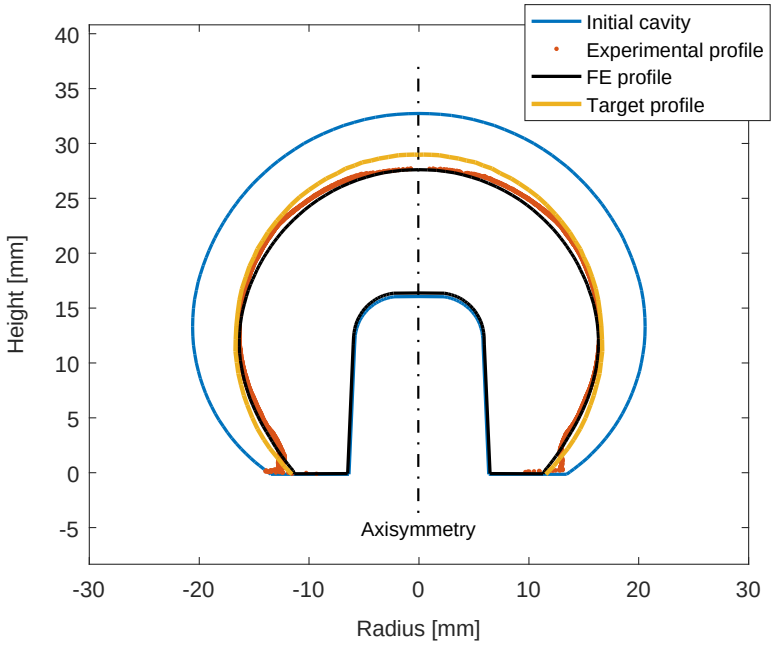

Figure 4.32 Comparison between experimental and numerical profiles.

For the studied application, the preliminary model and the density-dependent model lead to similar final geometries (Figure 4.33). However, the models result in different density fields. With the density-dependent model, one may identify two low-density spots, highlighting the importance of a more sophisticated material calibration, if the objective is to predict flaws in the final product, and in the present case, to diminish the failure probability of implants.

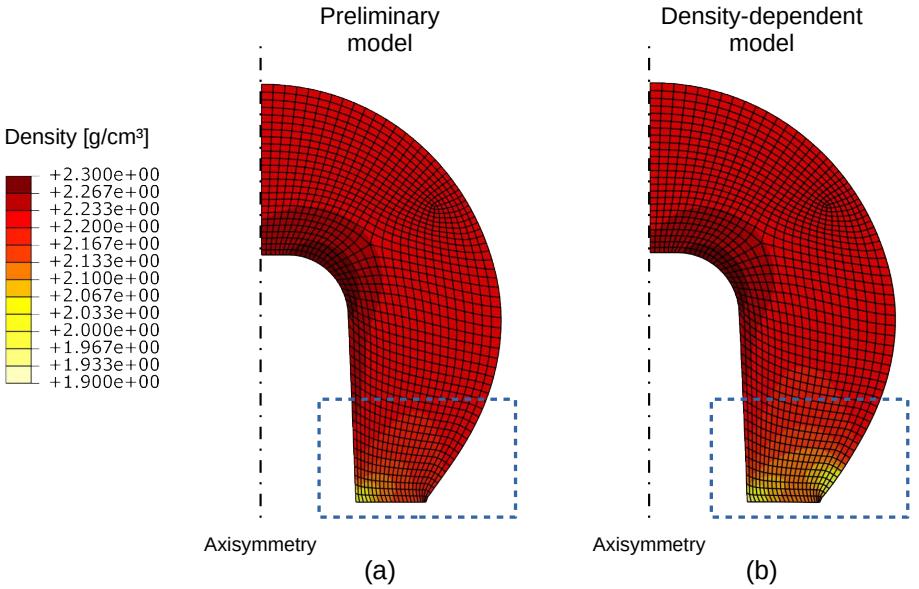

Figure 4.33 Comparison between the density fields obtained by the FE simulations with the (a) preliminary and (b) density-dependent constitutive models.

5 CONCLUSIONS

The main objective of this research project was to design Rubber Multiaxial Pressing through FE analyses for producing a ceramic femoral head. Reliable numerical analyses require precise characterization of the mechanical behavior of the materials.

To obtain a first preliminary identification/validation of the constitutive model for the studied alumina powder, a non-conventional procedure was developed. This experimental procedure proved to be an indirect evaluation of relative density distributions and simpler than most other procedures reported in the literature since the developed method does not rely on complex and expensive devices or techniques. Besides an isostatic press, which is a usual equipment, a uniaxial closed die, with cylindrical parts, was used. For the latter, a single requirement becomes necessary: a high ratio between its height and diameter, which may already be available or be simple to manufacture. In addition, two pressure sensors were used in the piston heads to measure the loss of pressure associated with friction between the powder and die walls, which led to an approach to calibrate a better set of numerical model parameters for the alumina powder used in this study, considering the large variation of their values found in the literature for similar systems. After uniaxial pressing and re-compaction by isostatic pressing, the final green compact shape and dimensions were used to validate the numerical model. The finite element analysis and experimental results have shown good agreement, demonstrating that the set of parameters obtained from the proposed procedure is valid. Some minor differences between numerical and experimental analyses could be observed because of the simplifications adopted in the constitutive models, such as the linear elastic behavior and the inelastic parameters considered as constant during powder compaction.

To further investigate the parameters of the compacted powder, uniaxial compression tests were performed. During this investigation, some experimental artifacts that led to spurious bending effects were revealed. These artifacts may

render inaccurate the usual assumption of uniform strain over the cross-section of the specimen. To overcome them, a FEMU-DIC procedure was developed, where DIC measurements were conducted by using two cameras that acquired images of two perpendicular free surfaces of the specimen, and the multi-point constraint technique was used to couple the degrees of freedoms of the shared boundary of the images captured from both faces in a DIC framework. A FEMU-F methodology was applied to calibrate a isotropic linear elastic and plastic (Drucker-Prager model) parameters for three distinct cases:

- Classical approach where DIC was used as a virtual strain gauge and the constitutive model was fitted with the load-strain curve independently for the results of both faces;
- Plane stress analysis where the displacements obtained independently from DIC analyses were prescribed as boundary conditions;
- 3D analysis where the multi-point constraint technique was used to couple the DIC results from image acquisitions of both faces, and extrapolation of the measured boundary conditions to two cross-sections.

The independent analyses for both faces (*i.e.,* classical approach and plane-stress analyses) resulted in different sets of parameters as a consequence of the violation of the uniform strain assumption. As plane stress analyses consider the bending effect in their plane, most of the calibrated parameters were closer to each other in comparison with the classical approach. The full consideration of the bending effect in the 3D analysis leads to a set of parameters that lies within the intervals of the parameters found from the previous two approaches. The average parameters of classical and plane stress analyses are also good approximations of the set of parameters obtained in the 3D analysis. However, the latter led to the lowest identification residuals and is thereby believed to provide the best set of parameters among the studied approaches. The developed procedure allowed us to check, measure and consider the bending effects in uniaxial compression tests and their analyses. Only two cameras were used and the boundary conditions had to be extrapolated even on some external surfaces.

The methodology previously discussed was enriched to handle a series of tests, removing the shortcoming of using a single test data for parameters identification. The multi-test approach based on FEMU-DIC analyses was used to calibrate the Drucker-Prager parameters as a function of density. The numerical model was able to describe satisfactorily all the experimental curves. Diametral compression tests were performed and their data, along with the results of uniaxial compression tests, were used to evaluate the angle of friction and material cohesion. The angle of friction found by this approach was 15% higher than that from the preliminary model.

To calibrate a hyperelastic model for rubber, uniaxial and volumetric compression tests were performed. Hyperelastic models of Arruda-Boyce, Ogden (order 3), and polynomial (order 2) were calibrated. The three tested hyperelastic models were able to satisfactorily describe the uniaxial compression data. However, the Ogden model was the most suitable choice for predicting the behavior of rubber in the volumetric test. As a good description of the volumetric behavior is a requirement for modeling RMP, the Ogden model was a natural choice.

An adequate rubber mold was designed for RMP of ceramic femoral heads, using FE simulations with the preliminary model. Using the designed rubber mold and other tools such as die and pistons, a ceramic femoral head was successfully pressed via RMP, demonstrating the feasibility of the process for ceramic parts. Although the initial density of loose powder was lower than the estimated level leading to a part slightly smaller than the target geometry, the FE and experimental profiles were in good agreement. The density field observed by the density-dependent model presents more low-density spots than the same field estimated by the preliminary model, highlighting the importance of a more detailed calibration for the identification of low-density regions in the final product. As part of future research, it may be possible to use tomography techniques for comparing the experimental and numerical density fields, which would provide a more comprehensive understanding of the material behavior and enable more accurate predictions.

6 REFERENCES

[1] Reddy, E.S., Rajasekharan, T.. Fabrication of textured (re= y, gd) composites by infiltration and growth of preforms by liquid phases. Superconductor Science and Technology 1998;11(5):523.

[2] Oberacker, R.. Powder compaction by dry pressing. Ceramics Science and Technology 2012;3:3–37.

[3] Sagawa, M., Nagata, H., Watanabe, T., Itatani, O.. Rubber isostatic pressing (RIP) of powders for magnets and other materials. Materials & Design 2000;21(4):243–249.

[4] Sagawa, M., Nagata, H.. Novel processing technology for permanent magnets. IEEE transactions on magnetics 1993;29(6):2747–2751.

[5] Aydin, I., Briscoe, B.J., Sanliturk, K.Y.. The internal form of compacted ceramic components: A comparison of a finite element modelling with experiment. Powder Technology 1996;89(3):239–254.

[6] Zipse, H.. Finite-element simulation of the die pressing and sintering of a ceramic component. Journal of the European Ceramic Society 1997;17(14):1707–1713.

[7] Kim, K., Kwon, Y., Kim, H.. Near-net-shape forming of alumina powder under hot pressing and hot isostatic pressing. International Journal of Mechanical Sciences 1997;39(9):1011–1022.

[8] Zeuch, D.H., Grazier, J.M., Argüello, J.G., Ewsuk, K.G.. Mechanical properties and shear failure surfaces for two alumina powders in triaxial compression. Journal of Materials Science 2001;36(12):2911–2924.

[9] Canto, R.B.. Projeto de fabricação de moldes para prensagem isostática utilizando tecnologia CAD/CAE e prototipagem rápida. Master's thesis; Universidade de São Paulo; 2002.

[10] Canto, R.B., Tita, V., Carvalho, J., Purquerio, B.M.. Finite element simulation of ceramic powder isostatic pressing process using material parameters for uniaxial compaction. Materials Science Forum 2003;561-566:416–418.

[11] Reiterer, M., Kraft, T., Janosovits, U., Riedel, H.. Finite element simulation of cold isostatic pressing and sintering of SiC components. Ceramics International 2004;30:177–183.

[12] Gruber, D., Harmuth, H.. Simulation of moulding of refractory bricks. Advances in Science and Technology 2010;70:167–172.

[13] Stupkiewicz, S., Piccolroaz, A., Bigoni, D.. Elastoplastic coupling to model cold ceramic powder compaction. Journal of the European Ceramic Society 2014;34(11):2839–2848.

[14] Shin, H., Kim, J.B.. A numerical investigation on determining the failure strength of a powder compact in unconfined compression testing by considering the compressible character of the specimen. Powder Technology 2015;277:156–162.

[15] Le Corre, V., Brusselle-Dupend, N., Moreaud, M.. Numerical modeling of the effective ductile damage of macroporous alumina. Mechanics of Materials 2017;114:161–171.

[16] Shima, S., Sakamoto, Y., Kotera, H.. Simulation of rubber isostatic pressing and shape optimization of rubber mold. International journal of mechanical sciences 2002;44(8):1603–1623.

[17] Yang, H.C., Kim, J.K., Kim, K.T.. Rubber isostatic pressing and cold isostatic pressing of metal powder. Materials Science and Engineering A 2004;382:41–49.

[18] Henderson, R.J., Chandler, H.W., Akisanya, A.R., Barber, H., Moriarty, B.. Finite element modelling of cold isostatic pressing. Journal of the European Ceramic Society 2000;20(8):1121–1128.

[19] Gruber, D., Harmuth, H., Michelitsch, A.. Simulation of moulding – Influencing factors and results for collector nozzels. 2012, p. 112–115.

[20] Carter, C.B., Norton, M.G.. Ceramic materials: science and engineering. Springer Science & Business Media; 2007.

[21] Garner, S., Strong, J., Zavaliangos, A.. Study of the die compaction of powders to high relative densities using the discrete element method. Powder Technology 2018;330:357–370.

[22] Güner, F., Sofuoglu, H., Cora, Ö.N.. An investigation of contact interactions in powder compaction process through variable friction models. Tribology International 2016;96:1–10.

[23] Sinka, I.C., Cocks, A.C.F.. Constitutive modelling of powder compaction - ii. evaluation of material data. Mechanics of Materials 2007;39:404–416.

[24] Güner, F., Cora, Ö.N., Sofuoğlu, H.. Numerical modeling of cold powder compaction using multi particle and continuum media approaches. Powder Technology 2015;271:238–247.

[25] Treloar, L.R.G.. The physics of rubber elasticity. Oxford University Press, USA; 1975.

[26] Shahzad, M., Kamran, A., Siddiqui, M.Z., Farhan, M.. Mechanical characterization and fe modelling of a hyperelastic material. Materials Research 2015;18(5):918–924.

[27] Hibbitt, H., Karlsson, B., Sorensen, P.. Abaqus theory manual. 2000.

[28] De Crevoisier, J., Besnard, G., Merckel, Y., Zhang, H., Vion-Loisel, F., Caillard, J., et al. Volume changes in a filled elastomer studied via digital image correlation. Polymer Testing 2012;31(5):663–670.

[29] Chandler, H.W., Sands, C.M., Song, J.H., Withers, P.J., McDonald, S.A.. A plasticity model for powder compaction processes incorporating particle deformation and rearrangement. International Journal of Solids and Structures 2008;45(7):2056–2076.

[30] Mooney, M.. A theory of large elastic deformation. Journal of applied physics 1940;11(9):582–592.

[31] Rivlin, R.. Large elastic deformations of isotropic materials. iv. further developments of the general theory. Philosophical Transactions of the Royal Society of London A: Mathematical, Physical and Engineering Sciences 1948;241(835):379–397.

[32] Ogden, R.W.. Large deformation isotropic elasticity – on the correlation of theory and experiment for incompressible rubberlike solids. Procedures of Royal Society of London A 1972;326(1567):565–584.

[33] Yeoh, O.H.. Some forms of the strain energy function for rubber. Rubber Chemistry and technology 1993;66(5):754–771.

[34] Boyce, M.C., Arruda, E.M.. Constitutive models of rubber elasticity: a review. Rubber chemistry and technology 2000;73(3):504–523.

[35] Basar, Y., Weichert, D.. Nonlinear continuum mechanics of solids: fundamental mathematical and physical concepts. Springer Science & Business Media; 2013.

[36] Bathe, K.J.. Finite element procedures. Prentice Hall; 1996.

[37] DiMaggio, F.L., Sandler, I.S.. Material model for granular soils. Journal of the Engineering Mechanics 1971;97(3):935–950.

[38] Chtourou, H., Guillot, M., Gakwaya, A.. Modeling of the metal powder compaction process using the cap model. part i. experimental material characterization and validation. International Journal of solids and Structures 2002;39(4):1059–1075.

[39] Brewin, P.R., Coube, O., Doremus, P., Tweed, J.H.. Modelling of powder die compaction. Springer Science & Business Media; 2007.

[40] Green, R.. A plasticity theory for porous solids. International Journal of Mechanical Sciences 1972;14(4):215–224.

[41] Shima, S., Oyane, M.. Plasticity theory for porous metals. International Journal of Mechanical Sciences 1976;18(6):285 – 291.

[42] Drucker, D.C.. A definition of stable inelastic material. Tech. Rep.; BROWN UNIV PROVIDENCE RI; 1957.

[43] Montilha, F.S., Rocco, F.O., Melo, C.C., Sciuti, V.F., Canto, R.B.. Identification of dilatancy in green compacted ceramic powder via digital image correlation. Powder Technology 2018;330:471–476.

[44] Roscoe, K., Burland, J.. On the generalized stress-strain behaviour of wet clay. Engineering Plasticity 1968;33:535–609.

[45] Diarra, H., Mazel, V., Busignies, V., Tchoreloff, P.. Comparative study between drucker-prager/cap and modified cam-clay models for the numerical simulation of die compaction of pharmaceutical powders. Powder Technology 2017;320:530–539.

[46] Drucker, D., Prager, W.. Soil mechanics and plastic analysis or limit design. Quarterly Journal of Applied Mathematics 1952;10(2):157–165.

[47] de Souza Neto, E.A., Peric, D., Owen, D.R.. Computational methods for plasticity: theory and applications. John Wiley & Sons; 2011.

[48] Aydin, I., Briscoe, B., Sanliturk, K.. Dimensional variation of die-pressed ceramic green compacts: comparison of a finite element modelling with experiment. Journal of the European Ceramic Society 1997;17(10):1201–1212.

[49] Lee, S.C., Kim, K.T.. Densification behavior of aluminum alloy powder under cold compaction. International Journal of Mechanical Sciences 2002;44:1295–1308.

[50] Learmonth, I.D., Young, C., Rorabeck, C.. The operation of the century: total hip replacement. The Lancet 2007;370(9597):1508–1519.

[51] Boutin, P.. Total hip arthroplasty using a ceramic prosthesis. pierre boutin (1924-1989). Clinical orthopaedics and related research 2000;(379):3.

[52] Lau, Y.J., Sarmah, S., Witt, J.D.. 3rd generation ceramic-on-ceramic cementless total hip arthroplasty: a minimum 10-year follow-up study. HIP International 2018;28(2):133–138.

[53] Capello, W.N., D'Antonio, J.A., Feinberg, J.R., Manley, M.T., Naughton, M.. Ceramic-on-ceramic total hip arthroplasty: update. The Journal of arthroplasty 2008;23(7):39–43.

[54] RenCast 4644-1 documentation. Huntsman International LLC; 2003.

[55] Briscoe, B., Rough, S.. The effects of wall friction on the ejection of pressed ceramic parts. Powder technology 1998;99(3):228–233.

[56] Melo, C.C., Moraes, A.L.I., Rocco, F.O., Montilha, F.S., Canto, R.B.. A validation procedure for numerical models of ceramic powder pressing. Journal of the European Ceramic Society 2018;38(8):2928–2936.

[57] Canto, R.B.. Theoretical and experimental study of the compaction and sintering processes of polytetrafluoroethylene (PTFE). Ph.D. thesis; Universidade de São Paulo - Brazil / École Normale Supérieure de Cachan - France (LMT-Cachan); 2007.

[58] Gustkiewicz, J.. Uniaxial compression testing of brittle rock specimens with special consideration given to bending moment effects. In: International Journal of Rock Mechanics and Mining Sciences & Geomechanics Abstracts; vol. 12. Elsevier; 1975, p. 13–25.

[59] Hawkes, I., Mellor, M.. Uniaxial testing in rock mechanics laboratories. Engineering Geology 1970;4(3):179–285.

[60] Peng, S.. Stresses within elastic circular cylinders loaded uniaxially and triaxially. In: International Journal of Rock Mechanics and Mining Sciences & Geomechanics Abstracts; vol. 8. Elsevier; 1971, p. 399–432.

[61] Sines, G., Adams, M.. Compression testing of ceramics. In: Flaws and Testing. Springer; 1978, p. 403–434.

[62] ASTM C1424-15. Standard test method for monotonic compressive strength of advanced ceramics at ambient temperature. Tech. Rep.; ASTM International; 2015.

[63] Melo, C., Furlan, M., Hild, F., Schmitt, N., Canto, R.. Uniaxial compression test on ceramic green compact with bending consideration using digital image correlation. Powder Technology 2020;376:136–148.

[64] Voce, E.. The relationship between stress and strain for homogeneous deformation. Journal of the Institute of Metals 1 948;74:537–562.

[65] Jendele, L., Červenka, J.. On the solution of multi-point constraints–application to FE analysis of reinforced concrete structures. Computers & Structures 2009;87(15-16):970–980.

[66] Felippa, C.A.. Introduction to finite element methods. Course Notes, Department of Aerospace Engineering Sciences, University of Colorado at Boulder, available at http://www.colorado.edu/engineering/Aerospace/CAS/courses.d/IFEM.d; 2004.

[67] Cook, R.D., et al. Concepts and applications of finite element analysis. John Wiley & Sons; 2007.

[68] Hild, F., Misra, A., Dell'Isola, F.. Multiscale dic applied to pantographic structures. Experimental Mechanics 2021;61(2):431–443.

[69] Ienny, P., Caro-Bretelle, A.S., Pagnacco, E.. Identification from measurements of mechanical fields by finite element model updating strategies: a review. European Journal of Computational Mechanics/Revue Européenne de Mécanique Numérique 2009;18(3-4):353–376.

[70] Pagnacco, E., Lemosse, D., Hild, F., Amiot, F.. Inverse strategy from displacement field measurement and distributed forces using fea. In: 2005 SEM annual conference and exposition on experimental and applied mechanics. 2005,.

[71] Grédiac, M., Hild, F., editors. Full-Field Measurements and Identification in Solid Mechanics. London (UK): ISTE / Wiley; 2012.

[72] Tarantola, A.. Inverse Problems Theory. Methods for Data Fitting and Model Parameter Estimation. Southampton (UK): Elsevier Applied Science; 1987.

[73] Hibbitt, D., Karlsson, B., Sorensen, P.. Abaqus 6.14 Documentation. Dassault Systèmes Simulia Corp.; Providence, RI, USA.; 2014.

[74] Neggers, J., Mathieu, F., Hild, F., Roux, S.. Simultaneous full-field multi-experiment identification. Mechanics of Materials 2019;133:71–84.

[75] Levenberg, K.. A method for the solution of certain non-linear problems in least squares. Quarterly of applied mathematics 1944;2(2):164–168.

[76] Marquardt, D.W.. An algorithm for least-squares estimation of nonlinear parameters. Journal of the society for Industrial and Applied Mathematics 1963;11(2):431–441.

[77] Twizell, E.H., Ogden, R.. Non-linear optimization of the material constants in ogden's stress-deformation function for incompressinle isotropic elastic materials. The ANZIAM Journal 1983;24(4):424–434.

[78] Coube, O., Riedel, H.. Numerical simulation of metal powder die compaction with special consideration of cracking. Powder Metallurgy 2000;43(2):123–131.

[79] Kim, H., Gillia, O., Dorémus, P., Bouvard, D.. Near net shape processing of a sintered alumina component: adjustment of pressing parameters through finite element simulation. International Journal of Mechanical Sciences 2002;44(12):2523–2539.

[80] Abdullah, O.G., Rasin, F.A., Al-Dhahir, T.A.. Finite element simulation of alumina ceramic powder compaction. International Journal of Pure and Applied Physics 2009;5(1):15–31.

[81] Frédy, C.. Modeling of the mechanical behavior of polytetrafluoroethylene (PTFE) compounds during their compaction at room temperature. Ph.D. thesis; Université Pierre et Marie Curie - Paris VI; 2015.

[82] Salvadori, A., Lee, S., Gillman, A., Matouš, K., Shuck, C., Mukasyan, A., et al. Numerical and experimental analysis of the Young's modulus of cold compacted powder materials. Mechanics of Materials 2017;112(Supplement C):56 – 70.

[83] Gethin, D.T., Solimanjad, N., Doremus, P., Korachkin, D.. Friction and its measurement in powder-compaction processes. In: Brewin, P.R., Coube, O., Doremus, P., Tweed, J.H., editors. Modelling of Powder Die Compaction. London: Springer London; 2008, p. 105–129.

[84] Fossum, A., Fredrich, J.. Cap plasticity models and compactive and dilatant pre-failure deformation. In: 4th North American Rock Mechanics Symposium. American Rock Mechanics Association; 2000,.

[85] Leclerc, H., Neggers, J., Mathieu, F., Roux, S., Hild, F.. Correli 3.0. 2015. IDDN.FR.001.520008.000.S.P.2015.000.31500.

[86] Cunningham, J.C., Sinka, I.C., Zavaliangos, A.. Analysis of tablet compaction. i. characterization of mechanical behavior of powder and powder/tooling friction. Journal of Pharmaceutical Sciences 2004;93(8):2022–2039. doi:{10.1002/jps.20110}.

[87] Han, L., Elliott, J., Bentham, A., Mills, A., Amidon, G., Hancock, B.. A modified drucker-prager cap model for die compaction simulation of pharmaceutical powders. International Journal of Solids and Structures 2008;45(10):3088–3106.

[88] Shang, C., Sinka, I.C., Pan, J.. Constitutive model calibration for powder compaction using instrumented die testing. Experimental mechanics 2011;52(7):903–916.

[89] Kim, Y.B., Lee, J.S., Lee, S.M., Park, H.J., Lee, G.A.. Calibration of a density-dependent modified drucker-prager cap model for azo powder. In: Advanced Materials Research; vol. 482. Trans Tech Publ; 2012, p. 1249–1256.

[90] Canto, R.B.. Estudo teórico e experimental dos processos de compactação e sinterização do politetrafluoretileno (PTFE). Ph.D. thesis; Universidade de São Paulo - Brasil/École Normale Supérieure de Cachan - França; 2007.